

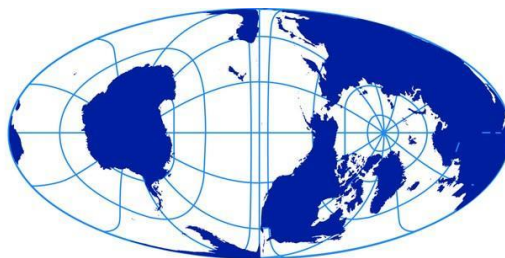
June 2018

The development and application of IceLake, an accurate and computationally  
efficient model of supraglacial lake evolution in the ablation zone of the  
Greenland Ice Sheet.

Author: Robert Law

Supervisor: Neil Arnold

University of Cambridge Geography Department



**Scott Polar Research Institute**

University of Cambridge



**UNIVERSITY OF  
CAMBRIDGE**

## Declaration

I declare that this thesis is my own unaided work, except where noted. It is no more than 20,000 words in length, excluding acknowledgements, declaration, bibliography, and captions.

## Acknowledgements

As night turns to day and the birds begin to sing, I must deeply thank Judith, Refna, and Hilton Law for making this year possible. I am very grateful for the guidance and support of Neil Arnold who has been willing to discuss ideas throughout and has provided invaluable pointers and suggestions. Without the support, encouragement, and proofing of Andrew Williamson I may have lacked the confidence and resolve to make it through to the end FAST enough and without Cecilia Hobbs I may have fallen asleep before getting here. Thanks also to Cameron MacKay, my favourite Raspberry, and the rest of the MPhil gang for being wonderful people, and thanks to the friendly tips from Samuel Cook and Tom Chudley. The atmosphere at SPRI has really made these months exceptional and I am grateful to every person within its walls. Additional thanks go to Corinne Benedek for her ideas and model source code, Sammie Buzzard for helpful modelling advice, and Brice Noel for providing RACMO data.

## Abstract

The supraglacial hydrological system of the Greenland Ice Sheet (GrIS) delivers ~60% of total mass loss from the ice sheet to the ocean (van den Broeke et al., 2016), making a thorough understanding crucial for sea level rise predictions. Supraglacial lakes play a crucial role in the evolution of this system and have been implicated in initiating rapid ice-sheet acceleration (Das et al., 2008), the formation of inland surface-bed meltwater pathways (Christoffersen et al., 2018; Hoffman et al., 2018) and cryo-hydrologic warming (Phillips et al., 2010, 2013). No model currently exists to reproduce the full evolution of these lakes in the ablation zone, including the effect of snow cover. Here, the IceLake model is presented which effectively replicates recorded supraglacial lake depth data to within 0.7 m after a 165-day, over-winter, run. IceLake is computationally efficient, taking <30 seconds for a one-year run using a 3.2 GHz processor. The parameter space of IceLake is comprehensively tested and the model output is found to be relatively insensitive to the variation of most parameters, with the exception of changes to the  $I_0$  term, which controls the amount of incoming shortwave radiation that can enter a lake's water column. IceLake is applied to a 100–2200 m a.s.l. elevation transect of Upernavik Isstrøm Glacier (72.8°N) in West Greenland to investigate the dependence of lake evolution on elevation. When only basal ice melt is accounted for and no water input is included, it is found that lake depth decreases at  $\sim 0.004 \text{ m m}^{-1}$ , that the time the lake has a frozen cover increases at  $\sim 0.06 \text{ days m}^{-1}$ , and that maximum lid thickness exhibits little variation, with a range of 1.15–1.95 m, although a clear increase and thicker average lids are seen if snow is excluded. The latter result has the important implication that even shallow (1.9 m) lakes at high elevation can effectively retard the cooling of the underlying ice overwinter and provide latent heat stores for the following spring, expediting the melt season evolution of supraglacial hydrology. Lake bottom freeze-up rate was found to be low ( $0.15 \text{ m year}^{-1}$ ) and controlled primarily by ice temperature at depth.

## Contents

<b>Introduction and rationale</b> .....	5
<b>Background</b> .....	7
Supraglacial lake bathymetry, distribution, and melt season evolution .....	9
Supraglacial lakes and surface energy balance .....	13
Buried lakes .....	13
Supraglacial lakes: their importance for surface-bed linkages and subglacial drainage systems .....	16
Existing lake and snow models .....	22
<b>Methods</b> .....	26
Surface energy flux .....	29
Shortwave radiation propagation through water and ice .....	31
Phase tracking .....	33
Lake convection .....	34
Lake albedo .....	34
Indexing and turbulence .....	35
Snow .....	35
Initial temperature profile .....	38
Grid setup and lake and snow inserts .....	38
Heat diffusion .....	40
Hydrograph input .....	42
Sensitivity testing .....	42
Model validation: comparison to Tedesco et al. (2012) .....	44
Model inter-comparison with Buzzard et al. (2018) .....	45
Endless winter .....	46
Application: lapse rate and RACMO elevation profile .....	46
<b>Results</b> .....	48
Sensitivity testing .....	48
Model validation: comparison to Tedesco et al. (2012) .....	52

Model inter-comparison with Buzzard et al. (2018).....	53
Validation results .....	54
Endless winter.....	56
Application: elevation-lake evolution relationship .....	58
RACMO-UPE-U comparison .....	58
Elevation-lake evolution relationship results .....	59
Model performance.....	64
<b>Discussion</b> .....	64
Broad model behaviour.....	64
Sensitivity testing.....	68
Model validation: comparison to Tedesco et al. (2012).....	76
Model inter-comparison with Buzzard et al. (2018) .....	77
The $I_0$ term: further discussion.....	77
Application: elevation relationships.....	79
RACMO-UPE-U comparison .....	79
Elevation-lake evolution relationship .....	79
<b>Possible model improvements</b> .....	81
Lake surface area .....	81
Further validation.....	82
2-Dimensional extension.....	82
Albedo.....	82
<b>Conclusion</b> .....	83
<b>References</b> .....	84
<b>Appendices</b> .....	99

## **Introduction and rationale**

Mass loss from the Greenland Ice Sheet (GrIS) has significantly accelerated over the last several decades to become a major contributor to global sea-level rise (Rignot et al., 2011),

responsible for 0.7-1.1 mm yr<sup>-1</sup> of the 2.8-3.6 mm yr<sup>-1</sup> total (IPCC, 2013). This acceleration eludes model predictions (Cowton et al., 2016; Goelzer et al., 2018) and is exacerbated by an Arctic that is warming at twice the global average (Hall et al., 2013; AMAP, 2017), northward incursion of warm water currents (Rignot et al., 2010), and a decrease in ice-sheet albedo (Van Angelen et al., 2014). Since 1991, ~60% of Greenland mass loss has been attributed to losses due to direct surface meltwater runoff (van den Broeke et al., 2016), a figure set to increase as firn aquifer capacity decreases (de la Pena et al., 2015; Noël et al., 2017; Steger et al., 2017), with the majority of the remaining ~40% loss coming from the direct discharge of ice over the grounding line at large, marine terminating glaciers (Nick et al., 2013). These alarming figures place the GrIS in a position of great societal importance for the 145 million coastal inhabitants living within 1 m of current sea level (Anthoff et al., 2006). Here, a modelling approach is used to gain a detailed understanding of the evolution of Greenlandic supraglacial lakes (hereafter 'supraglacial lakes', 'meltwater lakes', or 'lakes'), an important aspect of the overall supraglacial hydrological system, which remains poorly quantified by field observations and modelling (Rennermalm et al., 2013; Vernon et al., 2013). Comprehensive modelling of these lakes provides insight into buried lake formation (Koenig et al., 2015); basal ice temperature; water temperature and volume, which can be used to track the transfer of atmospheric heat englacially (Phillips et al., 2010) or subglacially (Tedesco et al., 2013); and enhanced surface melting (Tedesco et al., 2012). This understanding can then inform a more holistic view of GrIS melt processes and can enable better quantification of runoff pathways and meltwater storage.

The overall objective of this work was to build an efficient and realistic model of meltwater lake evolution on the GrIS that could be used to give a clearer understanding of the research shortfalls identified above, as well as understanding the physical processes involved. This was achieved through five distinct sections: development, sensitivity testing, validation, intercomparison, and application. The model created, IceLake, is designed with capabilities beyond those of existing models (see review of current models), to be robust under a range of forcing, and to have a rapid run time. The rationale for reducing run time is that it facilitates the implementation of improvements, alterations, and customisation with rapid feedback on their efficacy; that the model can be applied to a large area of the ice sheet using varying forcing data, without a prohibitive computational cost; and that the model could be coupled

with broader hydrological models if required, without hindering their overall performance. Additionally, extensive sensitivity testing can be carried out, adding credibility and transparency to model results (Saloranta and Andersen, 2007). This modelling approach will neatly complement observational studies as it is not limited by the spatial and temporal resolution of available remotely sensed imagery, or by gaps in coverage due to clouds. It could also be used for more robust forecasting, building on studies such as that by Leeson et al. (2015).

### **Background**

The hydrological system of Greenland is one of the least understood hydrological systems on earth (Smith et al., 2015; Yang and Smith, 2016), but perhaps one of the most active areas of current hydrological research. Research has moved at a rapid pace over the last decade, but details such as how supraglacial hydrology will respond to future warming and the spatial and temporal patterns of surface-to-bed linkages, remain poorly constrained with much left to uncover (Chu, 2013; Koziol et al., 2017; Nienow et al., 2017). The supraglacial hydrological system of Greenland comprises three meltwater routing pathways: over-ice flow, flow through streams and rivers, and groundwater flow through firn aquifers. Ultimately, this water enters moulines that drain to the interior or base of the ice sheet (Catania et al., 2008; Catania and Neumann, 2010), flows over the periphery of the ice sheet, or refreezes in firn aquifers (figures 1 and 2, Harper et al., 2012). The relevance of supraglacial hydrology to the timing and quantity of meltwater leaving the ice sheet is obvious, but it may also play a significant role in altering ice dynamics through meltwater delivery to the base and disturbance of basal hydrology.





Figure 1: images of aspects of the Greenland supraglacial hydrology. Top left: a canyon carved by the outflow of a supraglacial lake, people centre right for scale. Top right: a moulin routing a meltwater stream to the ice-sheet interior. Bottom, a supraglacial lake ~1 km in diameter. Incised channel inflow can be seen in the top right of the image. Images from Joughin/AAS via The Guardian (2012)

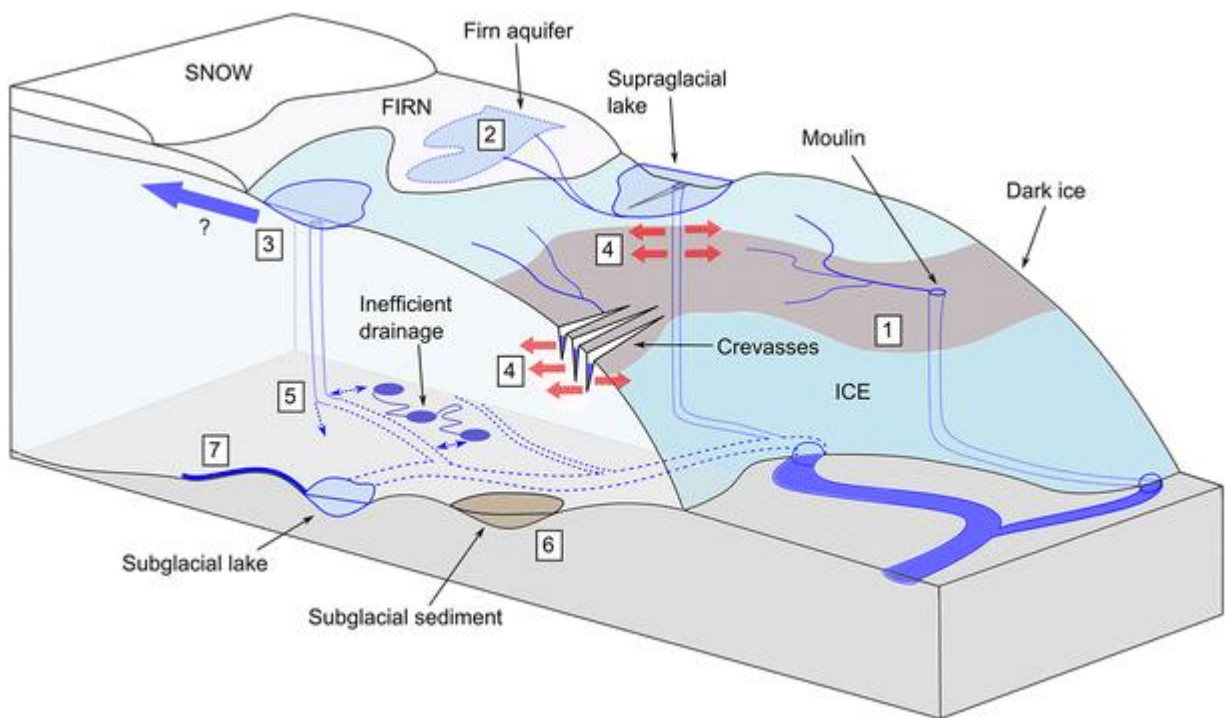


Figure 2, schematic overview of GrIS hydrology. (1) darkening of the ice sheet, (2) surface firn densification processes, (3) surface to bed connections at higher elevations, (4) cryo-hydrologic warming, (5) rates of channelisation at the ice bed interface, (6) subglacial sediments and till deformation, and (7) basal melt rates.

Figure and description from Nienow et al. (2017).

### Supraglacial lake bathymetry, distribution, and melt season evolution

The presence of a lake requires two criteria be fulfilled: sufficient melt, both *in situ* and in the surrounding catchment, and a suitable depression for the lake to occupy. Echelmeyer et al. (1991) first observed that supraglacial lakes fill depressions which do not appear to be advected, suggesting they are a surface expression of bedrock topography and are dynamically supported. This was expanded upon by Lampkin and Vanderberg (2011) who looked at transfer of basal topography to the surface, finding that basal structures with a wavelength closest to 8 times the total ice thickness are most readily transferred to the surface. This means that as ice thickness increases, larger basal features are required to bring about surface depressions, which will in turn be larger. As the surface gradient of the GrIS decreases with increasing elevation and ice thickness (Howat et al., 2014), the area that can support supraglacial lakes increases with a move inland on the GrIS as larger, more numerous depressions are present (Lüthje et al., 2006; Fitzpatrick et al., 2014). The typical bathymetry of a supraglacial lake is shallow, circular, and approximately sigmoidal (figure 3, Box and Ski, 2007; Fitzpatrick et al., 2014), with a maximum depth-diameter ratio of roughly 1:1000. So called 'slush swamps' comprising a mixture of ice, water, and saturated firn are observed above the equilibrium-line altitude (Lüthje et al. 2006; Sneed and Hamilton, 2007; Poinar et al. 2015) and are characterized by diffuse boundaries across broad topographic lows (figure 4).

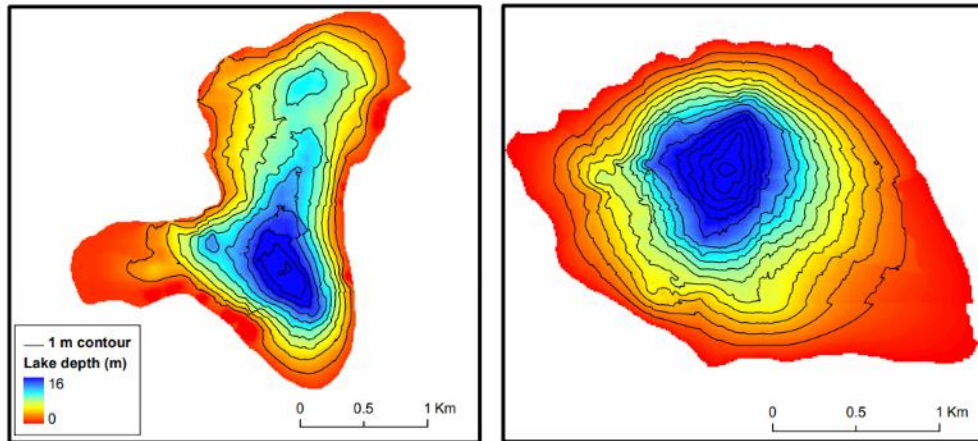


Figure 3: bathymetry maps for two lakes from the study of Fitzpatrick et al. (2014)

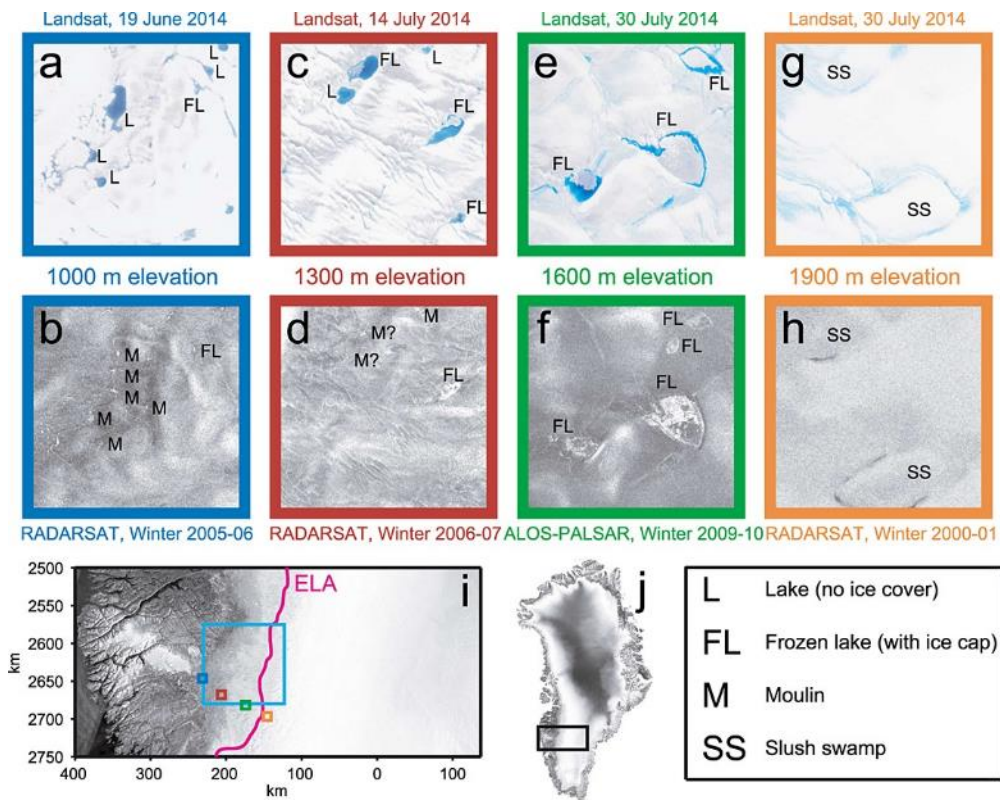


Figure 4: frozen lakes, drained lakes, moulins, and slush swamps seen from remotely sensed data at different elevations. From Poinar et al. (2015).

Remote sensing of supraglacial lakes in south west Greenland from Box and Ski (2007) using MODIS imagery shows a maximum depth of 12.2m, an average depth of 2-5 m, a maximum area of 8.9 km<sup>2</sup>, and a maximum volume of 0.05 km<sup>3</sup>. Another study using Landsat 7 data finds that the maximum average lake depth occurs on the 1st August for the western margin of Greenland at 3.9±1.1 m (McMillan et al., 2007). Liang et al. (2012) found lake distribution with

elevation at 69°N on the western margin to be fairly uniform from 800-1,500 m (figure 5), though Leeson et al. (2015) observe lakes up to 1,700 m at a nearby location, with a lesser proportion of lakes at low elevation due to more extensive crevassing (Chu, 2013). For the entire ice sheet, Selmes et al. (2011) mapped the evolution of 2,600 lakes and found that 61% occurred in the south west region, which forms the focus for the majority of supraglacial lake studies, whereas only 1% occurred in the south east, where mass loss from dynamic thinning is greatest (Velicogna and Wahr, 2006). The lakes are observed to transiently occupy up to 2.7% of the entire ablation zone (Lüthje, 2005; Box and Ski, 2007). Johansson and Brown (2013) found lake initiation typically occurs in May after  $40 \pm 18.5$  positive degree days, with lid formation in September and the exact date dependent on temperature lapse rate, atmospheric variability across Greenland, and annual weather trends. Most lakes do not remain present for this duration however, with Johansson and Brown (2013) observing ~80% of lakes in south west Greenland to drain before winter, whilst Selmes et al. (2013) record a value of ~50% for the entire ice-sheet.

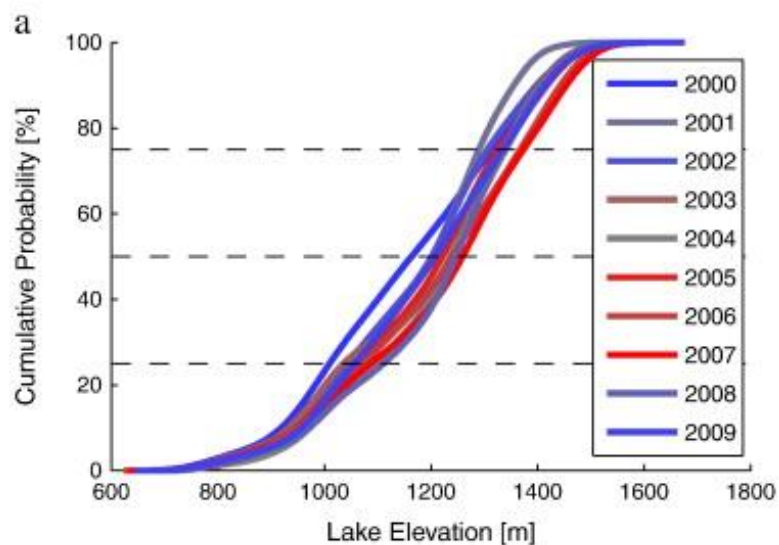


Figure 5: Cumulative probability of supraglacial lake occurrence with elevation from 2000 to 2009 in central western Greenland. From Liang et al. (2012)

As a lake approaches the boundaries of its depression it may overtop its banks or incise a channel, the fate of an estimated third of supraglacial lakes (Selmes et al., 2013). Tedesco et al. (2013) observed the latter for Lake Half Moon, central western Greenland, where drainage was initially rapid (22 hours), with removal of snow blocking the previous winter's channel by

slush flows, before drainage slowed exponentially over the next week due to a decreasing hydraulic head. This would be defined as 'stable' supraglacial drainage under the classification of Raymond and Nolan (2004) as the rate of incision from frictional heat dissipation is outpaced by a drop in depth, meaning the lake stabilises with its level equal to that of the incised channel. Alternatively, 'unstable' supraglacial drainage, as observed by Selmes et al. (2013) and modelled by Kingslake and Sole (2015) may occur where the bottom of the incised channel outpaces a reduction in water level. Koziol et al. (2017) also model overtopping and incision of supraglacial lakes, extending from Kingslake and Sole (2015), by including a snowpack layer, as part of a wider-scale model of supraglacial-hydrology evolution over a melt season in Paakitsoq, west Greenland. Alternatively rapid (< 2 day) drainage through a lake-bottom moulin occurs for 10-13% of lakes (Selmes et al., 2013) as discussed in greater depth later.

Placing supraglacial lakes within the broader supraglacial hydrology system, Koziol et al. (2017) use modelling to suggest that in Paakitsoq, West Greenland, crevasses drain 47% of meltwater, lake hydrofracture is responsible for 3%, with the opened moulins later capturing an additional 21%, and that moulins not associated with supraglacial lakes route a further 15%. At elevations above 850m however, they find that the predominant mode of meltwater routing is lake hydrofracture and subsequent flow through the newly opened moulin (figure 6). It should be noted however, that Koziol et al. (2017) use a volume threshold for predicting lake-drainage events following Krawczynski et al. (2009), which has since been shown to be an unreliable predictor of the precise timing and magnitude of lake-drainage events, even though it can reproduce the broad statistical patterns of lake drainage across the whole region (Williamson et al., 2018). Meltwater is delivered to supraglacial lakes through supraglacial streams, which are fed in turn by saturated slush, channel erosion, precipitation, and surface melt (Marston, 1983). Lake watersheds fluctuate throughout the melt season as lakes overtop their boundaries or incise channels, thereby contributing to their current catchment, or drain to the ice-sheet interior, cutting off their meltwater supply. As some lakes are seen to experience more than one drainage in a season (Fitzpatrick et al., 2014; Williamson et al., 2017) it is also evident that these moulins can temporarily, or permanently close, meaning their catchment is once again passed on downstream. This means that there is no one standard hydrograph input and that the hydrograph for a particular lake can easily

exhibit wide variation from one year to the next. On average however, cumulative hydrographs from Arnold et al. (2014), who model seasonal evolution of meltwater storage in the western GrIS, generally exhibit a sigmoidal shape with maximum input during the height of the melt season.

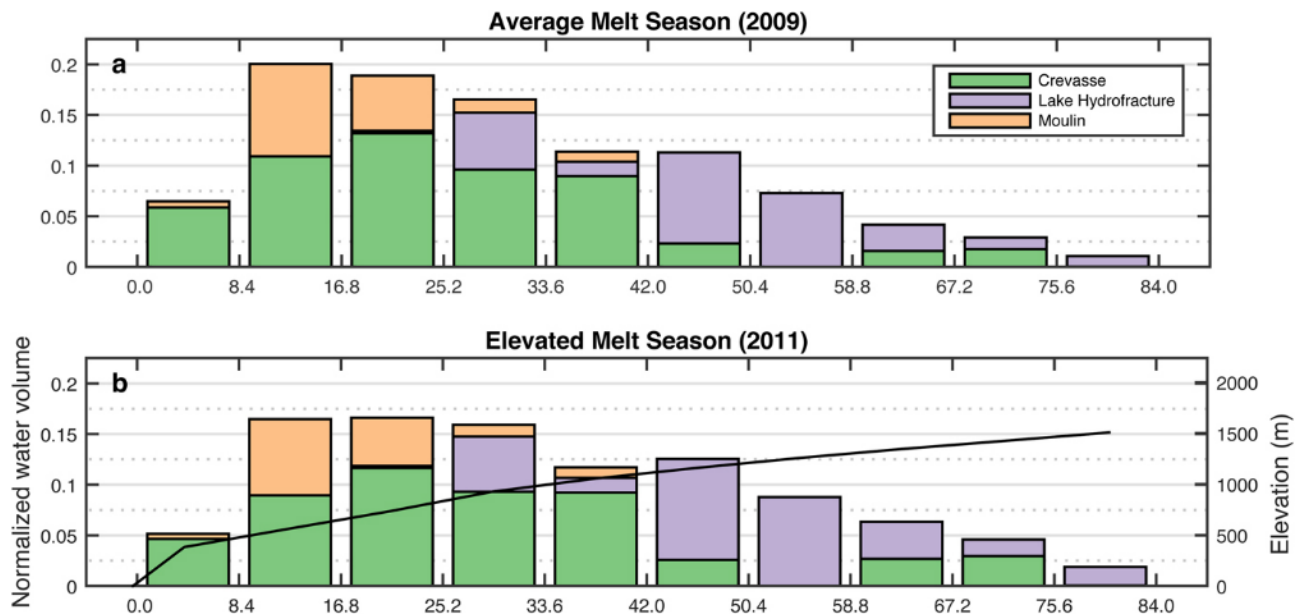


Figure 6: Partitioning of water into different pathways at different distances from the study margin of Koziol et al. (2017). The black line in middle plot is the width-averaged elevation profile of the study area. From Koziol et al. (2017). Note increasing importance of lake hydrofracture at increasing elevation.

### Supraglacial lakes and surface energy balance

Previous lake models for Greenland have focussed on lake's impact on melt rates and overall surface mass balance as they are darker than surrounding ice and have a lower albedo (Lüthje et al., 2006). Field data suggest lakes increase melt by 110-135% compared to bare ice (Tedesco et al., 2012). However, due to their small proportional coverage and that their maximum depth (and therefore minimum albedo) is obtained towards the end of the melt season when incoming shortwave radiation flux is waning, the enhanced ablation resulting from a 50% increase (by 2100) in their area is predicted to be only 0.7-0.8% of the total change (Leeson et al., 2015).

### Buried lakes

Little attention was given to the fate of lakes after the end of the melt season until Koenig et al. (2015). Lüthje et al. (2006), Johansson and Brown (2013), Selmes et al. (2013), and Arnold et al. (2014), for example, all assume that the lakes freeze-through entirely over winter. Koenig et al. (2015) use airborne radar from project IceBridge to observe 57-127 buried lakes from 2009 to 2012 across the entire periphery of the GrIS, with Miles et al. (2017) suggesting this may be an underestimate by a factor of three. They find that buried lakes occur in the same location as an observed summer lake detected using MODIS data (figure 7c). The majority of the lakes they detected lie between 1000 and 2000 m above sea level (a.s.l.) on the western periphery of the ice sheet (figure 7b), with fewer detected in the south east despite a high density of flight lines (in accordance with a lower observed number of supraglacial lakes, Selmes et al., 2011). Many lakes were observed on two consecutive years and one on three consecutive years, with the exact number obscured by shifting IceBridge flight lines. Some of the lakes remain buried for the entirety of the subsequent melt season. The vast majority of these lakes exhibit no visible surface signal whatsoever, but radar shows the average snow-depth above them to be 0.65 m and the average ice-layer thickness to be 1.4 m (figure 7a). An important aspect of these buried lakes is that the presence of a pre-existing body of water progressing into the melt season means that there is a store of latent heat which can immediately begin acting on its surroundings, for example causing earlier onset of channel formation. However, Koenig et al. (2015) do not hold this retained latent heat to be of importance to the overall energy balance of the GrIS, comparing the first order estimate of 1.5 Gt of water stored in such lakes to the 140 Gt believed to be stored in firn aquifers (Forster et al., 2014; Koenig et al., 2014) and the 100 - 300 Gt melt lost through GrIS runoff annually (Vernon et al., 2013).

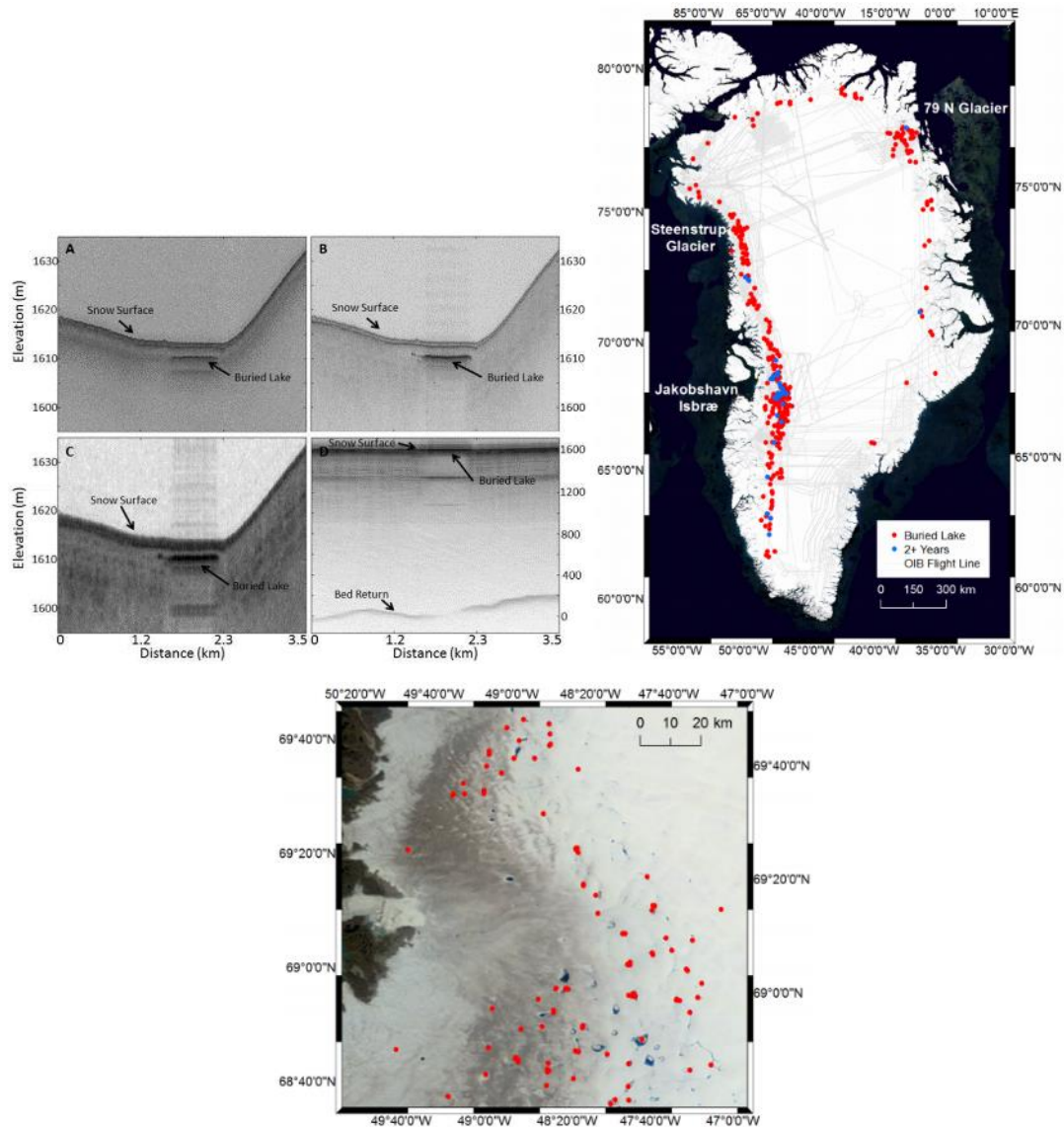


Figure 7a, top left: radar echograms for different frequencies for the same buried lake, ~90 km inland from the terminus of Jakobshavn Isbrae. 7b, top right: buried lakes observed by Koenig et al. (2015). Note IceBridge flow lines in light grey which offer less coverage on the eastern coast. 7c, bottom: buried lake locations overlain on MODIS data showing occurrence of lakes in August. All from Koenig et al. (2015).

If a buried lake is uncovered in spring, Koenig et al. (2015) observe the formation of a characteristic crescent or toroid shape, with a lid disconnected from the lake shores which persists into the early melt season and melts from the outside inwards. The overall evolution of these lakes mirrors that of shallow, laterally-extensive lakes seen in Arctic tundra, which persist until complete refreezing occurs, or remain with a liquid core for the entirety of winter (Surdu et al., 2014). In the Arctic tundra, modelling predictions suggest that warming climate will lead to shallower ice lids which are present for a decreasing amount of time (Duguay et

al., 2006). Koenig et al. (2015) suggest that the degree of connectivity of the lake to the exterior and the meltwater volume stored in the lake at the end of the melt season are primary controls on whether a buried lake will form, but they speculate on which is more important, sowing the seed for further investigation.

Separately, Miles et al. (2017) use Sentinel-1 synthetic aperture radar to define lake freeze-through as when backscatter values are equal to the lake surroundings (i.e. lid formation), and subsurface lakes as below surface water storage. For 2015, Miles et al. (2017) observe mean subsurface lake formation on the 9<sup>th</sup> August and mean disappearance on the 8<sup>th</sup> October. In contrast to Koenig et al. (2015), Miles et al. (2017) suggest that full freeze-through does occur before spring, citing lesser C-band radar penetration depths and an increased data time span as a possible explanation. Additional work on buried lakes is also currently being carried out at the Scott Polar Research Institute (SPRI), Cambridge, to explore the winter drainage of supraglacial lakes, observed through the wintertime development of surface depressions where lakes were previously located. The work presented here provides important quantification of buried lake phenomenon from a modelling angle.

#### Supraglacial lakes: their importance for surface-bed linkages and subglacial drainage systems

The earliest suggestion that supraglacial lakes in Greenland may drain subglacially came when Russell (1993) aerially photographed 'circular depressions' following reports by residents of Kangerlussuaq that releases of meltwater in the nearby rivers during February 1990 had occurred, when no melt was expected. It was suggested that the circular depression was the site of a lake that had drained through > 1 km thick ice to the subglacial system, resulting in the outburst, but no explanation was proposed and the matter received limited further investigation. Separate to ice sheets, the transfer of surface melt to the base for temperate and polythermal alpine glaciers had been acknowledged for decades (Bindschadler et al., 1977; Vornberger and Bindschadler, 1992; Hubbard and Nienow, 1997; Hodson and Ferguson, 1999). This focus on valley glaciers reversed, and the GrIS garnered widespread attention from the glaciological community, when Zwally et al. (2002) observed that meltwater availability was correlated with velocity in the equilibrium zone of the west-central GrIS, strongly suggesting a connection from surface to base (figure 8). This study acted as a catalyst

for further work as it presented a mechanism by which a warming atmosphere could near instantaneously influence the lowermost ice layers and basal sediment of an ice sheet, where the majority of deformation occurs through ice plastic deformation, basal sediment shear, and basal sliding (Benn and Evans, 2010). Prior to this, it was assumed that the impact of climate on ice-dynamic processes would take hundreds of years to millennia due to the slow rate of heat diffusion through the ice from the atmosphere, and the relatively small impact that surface mass balance would have on driving stresses (Alley and Whillans, 1991). The major source of incoming melt water suggested by Zwally et al. (2002) was flow through supraglacial streams into moulin, which peppered the lower ablation zones at relatively high density ( $0.2 \text{ km}^{-2}$ ), with the exact mechanism that created these pathways left open to speculation.

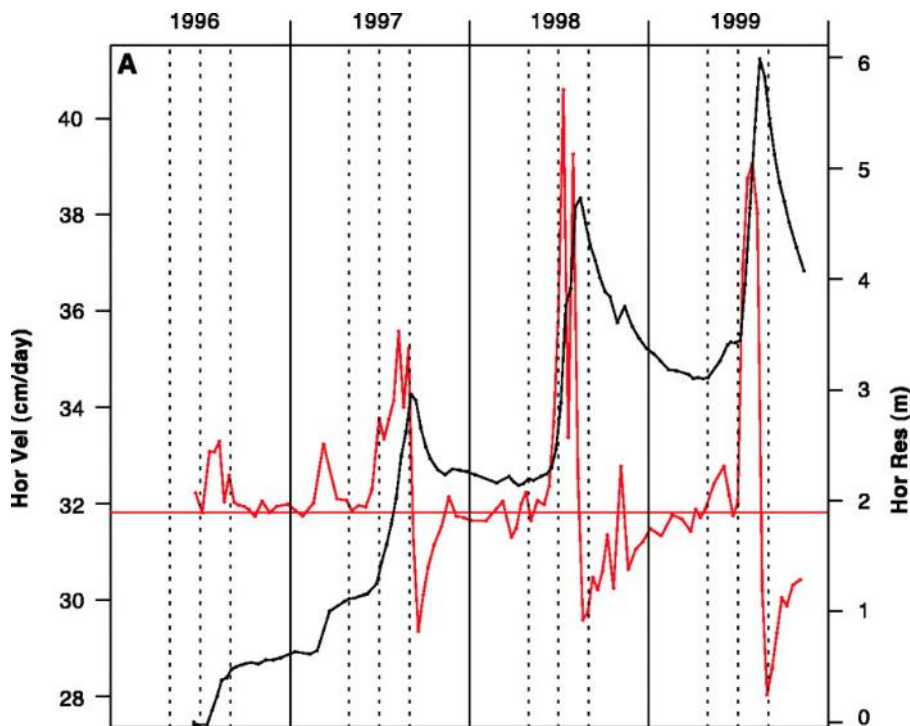


Figure 8: horizontal ice velocity (red curve) along a smoothed line of motion showing ice accelerations during the summer melt seasons and the abrupt transitions to deceleration around the times of melt cessation. The cumulative additional motion (horizontal residual, black) relative to a wintertime-average velocity of 31.33 cm/day is 6.0 m by the time of the maximum velocity in 1999. From Zwally et al. (2002)

In the wake of Zwally et al. (2002), efforts were redoubled to properly grasp the genesis and morphology of surface-to-bed connections. Boon and Sharp (2003) observed fracture propagation through 150 m thick ice in Ellesmere Island, Canada, in a stilted manner

suggesting repeated fracture progression. Das et al. (2008) then observed and monitored the rapid, sub-two hour drainage of a ~2 km diameter lake, and the formation of a surface to bed conduit. They showed that this rapid drainage could have a large but fleeting impact on the surrounding ice, raising basal pressure to near overburden and triggering a 20% velocity increase for 24 hours, although half of the resulting displacement was countered by a subsequent deceleration. Das et al. (2008) hypothesised that the integrated effect of many such lake drainages could be held responsible for the summer speed up observed by Zwally et al. (2002). This conclusion built upon a body of theoretical work from van der Veen (2007) and van der Veen (1998), who showed that a crevasse modelled under linear elastic fracture criteria, which exceeded a threshold depth, would propagate indefinitely through hydrofracture given a constant meltwater supply and would do so at a rate primarily governed by the flux of that supply. This threshold depth was determined to be on the order of tens of metres by Alley et al. (2005), giving crevasse patterns and the stress regime across the GrIS a new importance, as it was considered improbable that a surface to bed connection would form without this perturbation. An important finding of the van der Veen (2007) study is that a large volume of water (~35,000m<sup>3</sup> for ~1km of ice) is necessary in order to allow full connectivity to the base, although being larger than this threshold gives no statistically significant indication that a lake will drain by hydrofracture (Williamson et al., 2018).

The idea of surface to bed connections generated substantial interest in the glaciological community, and debate has since been ongoing regarding the importance of supraglacial meltwater drainage on GrIS dynamics, and whether lakes are able to drain to the bed at greater elevations inland (Nienow et al., 2017). Whilst early studies (Zwally et al., 2002; Das et al., 2008; Joughin et al., 2008) make it clear that surface to bed routing can cause a marked increase in ice velocity (~25%) at small time scales by perturbing a steady-state system, Sundal et al. (2011) and Sole et al. (2013) point to a net slow down on annual time scales, and decadal observations from Tedstone et al. (2015) show that a land-terminating sector of the western GrIS was seen to decrease in velocity by 10-12% despite a 50% increase in the supply of meltwater from 1985-2014. This dichotomy in ice-sheet response dependent on the time scale considered has been a central concern of studies published on the matter in the last decade, with the net outcome for GrIS mass loss pivoting on the impact of a spatially and

temporally heterogeneous supply of meltwater to the subglacial hydrological system (Flowers, 2015).

During summer in the ablation zone, supraglacial meltwater delivery to the bed outweighs input from basal geothermal and frictional melting by 1-2 orders of magnitude (Fahenstock et al., 2001; Bøggild et al. 2010; Banwell et al., 2016) making it a crucial input when understanding the subglacial hydrological system in this region. In response to this influx, the subglacial hydrological system exhibits a continuum of behaviour between two endpoints: an inefficient, distributed system incapable of quickly evacuating large quantities of water leading to a loss of basal traction, and an efficient, channelised system that easily routes large supplies of meltwater and maintains basal friction (Kamb, 1987; Howat et al., 2008; Benn and Evans, 2010; Schoof, 2010). The predominant drainage mode depends, among other considerations, on the gradient of surface ice (which has a strong control on subglacial hydraulic potential gradients), temperature and ice thickness (dictating the closure rate of ice-incised channels), and the nature and permeability of the bed materials (Flowers, 2015; Nienow et al., 2017). Importantly for its relation to the supraglacial hydrology, subglacial hydrological mode is strongly influenced by the delivery rate of meltwater, with higher flow rates leading to channel expansion through viscous heat transfer, and therefore greater efficiency (Schoof, 2010; Mankoff and Tulaczyk, 2017). In this manner, a large inflow of meltwater will raise basal pressure facilitating greater flow rates, but will also act to widen the channels through which it flows, eventually allowing quicker evacuation of subglacial meltwater. Given suitable conditions, this can mean that an initial speedup in glacier flow can give way to an eventual slow down as the subglacial hydrology system switches from an inefficient to efficient regime over the course of a melt season (Nienow et al., 1998; Flowers, 2015; Cowton et al., 2016; Nienow et al., 2017).

The view that the spatial and temporal distribution of supraglacial meltwater supply controls seasonal velocity patterns and subglacial hydrology mode is supported by dye-tracing measurements from Chandler et al. (2013) and Cowton et al. (2013), who observe a decrease in drainage response time resulting from melt season evolution from an inefficient to efficient system. GPS measurements are also in agreement with Sole et al. (2013) finding no significant correlation between surface melt and annual ice flow for a land-terminating, 115 km transect,

in the west of the GrIS. This view is corroborated by Tedstone et al. (2013) who measured slower ice-marginal flow during the record melt year of 2012 than during the average melt year of 2009. Doyle et al. (2014) however observed a 2.2% flow increase, 140 km inland of the western margin of the GrIS, persistent over a three-year period and related to increasing surface melt (figure 9). This inland difference is a suggested response to inland regions being predisposed to inefficient drainage due to thick ice and lower meltwater input, impeding the development of efficient channels and generating greater basal water pressure (Bamber et al., 2007; Chandler et al., 2013; Howat et al., 2013; Meierbachtol et al., 2013; Doyle et al., 2014; Poinar et al., 2015). Results from the modelling study of Koziol and Arnold (2018) however, question the importance of an inland response, with a 400% increase in melt responsible for only a 25% increase in annual velocity, although this study was static and did not include ice-dynamic response to changes in ice-sheet configuration.

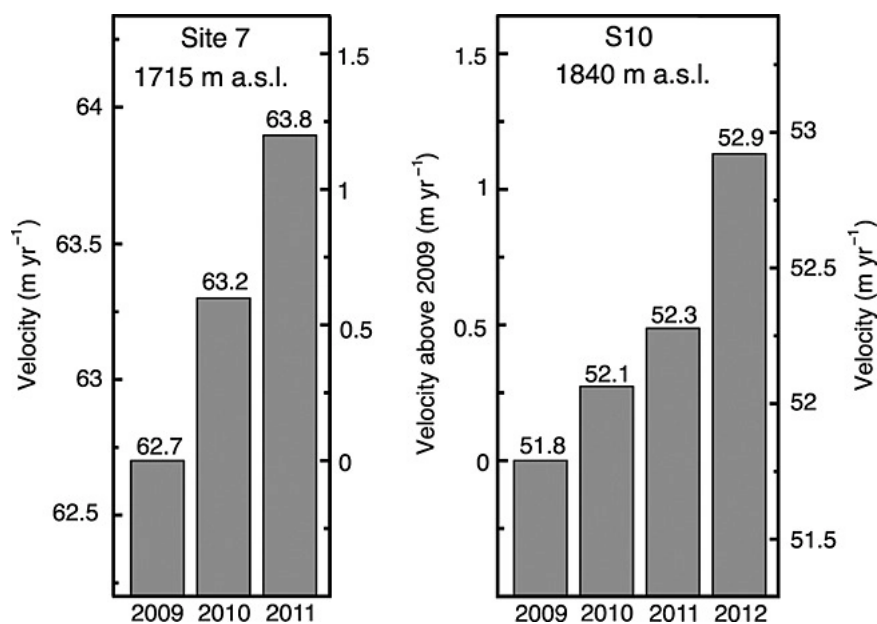


Figure 9: Annual velocity at sites used by Doyle et al. (2014). The center axes show the speed above the respective 2009 velocity. From Doyle et al. (2014).

The above studies all focus on land-terminating sectors of the western GrIS; the picture for marine terminating sectors, where dynamic mass loss is concentrated (van den Broeke et al., 2009), is less clear with fewer studies and a need for greater understanding. The effect of supraglacial meltwater on marine-terminating glaciers is potentially large due to its interaction with fjord waters, affecting the stress distribution at the calving front, and

generating buoyant meltwater plumes that can erode the underside of floating glacier tongues (Jenkins et al., 2011; Xu et al., 2012; Moon et al., 2015). Supraglacial meltwater may also effect offshore ecosystems by delivering ferrous sediments important for productivity (Hawkings et al., 2018). Moon et al. (2014) present five-year records for 55 marine-terminating glaciers and show that high sensitivity to terminus retreat in some glaciers sustains fast summer velocities beyond the end of the melt season, whilst other outlet glaciers do not seem to transition from an inefficient to an efficient system. Furthermore, the velocity patterns of the glaciers are not consistent year-on-year. In light of the findings of Moon et al. (2014), and the possibility of increasing velocity inland (Doyle et al., 2014), the importance of a shifting inland boundary of supraglacial lakes becomes apparent. This is as lakes appear to be the main operator in the formation of surface-bed connections, as seen from WorldView data used by Hoffman et al. (2018) and the modelling of Koziol et al. (2017) for greater elevations.

Howat et al. (2013) showed a decadal-scale advance inland for a selection of study sites across the entire GrIS (figure 10), advanced upon by Gledhill and Williamson (2018) who manually delimited over 8,000 lakes in a north-western sector from 1985–2016 to observe a 299 m increase in average lake elevation and 418 m increase in maximum observed elevation. Future predictions from Leeson et al. (2015) and Ignéczi et al. (2016) suggest the accelerating lake advance inland will continue, with a 50% and 100% increase by 2030 and 2070 respectively under a moderate (RCP 4.5) climate-change scenario. Poinar et al. (2015) use winter velocity data to place an upper limit on these lakes draining of 1600 m, based on a threshold for fracturing and crevasse formation below a principal surface strain rate of  $+0.005 \text{ yr}^{-1}$ . This assertion is challenged by remote sensing from Cooley and Christoffersen (2017) showing lakes detectable in MODIS imagery above 1,600 m are equally as likely to drain as those at lower elevations. Additionally, Christoffersen et al. (2018) model the propagation of tensile stress perturbations to demonstrate that lakes as far apart as 80 km can form expansive networks that drain in a cascading fashion in areas where fractures are ordinarily absent. This reveals the importance of understanding the inter-annual evolution of lakes at increasing elevations and their impact on surrounding ice temperature and morphology, as they hold the key to enabling the transfer of large amounts of water to the base in potentially sensitive inland regions and less-understood marine-terminating sectors.

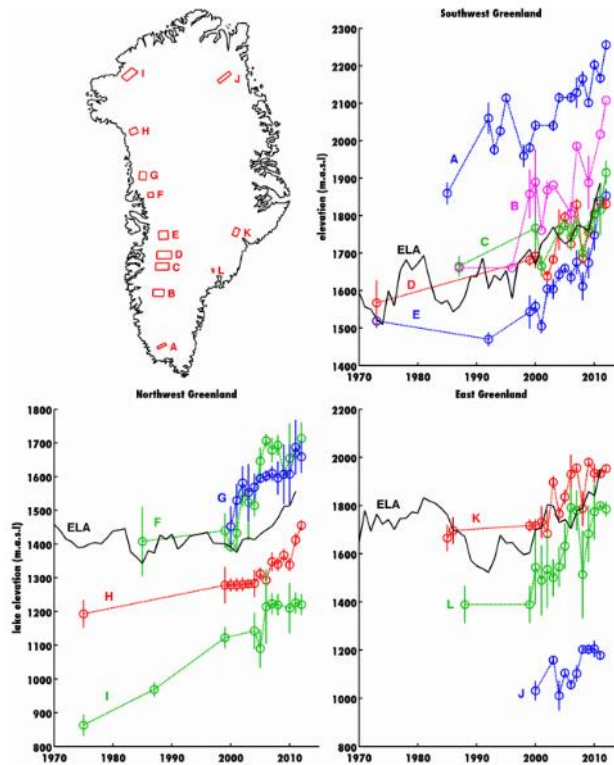


Figure 10: inland increase in upper  $0.1 \text{ km}^2$  of lake area within each of the study areas seen in the upper left panel. Black curves show the average equilibrium line altitude for each region. From Howat et al. (2013)

### Existing lake and snow models

In response to the uncertainty surrounding the importance of meltwater and the formation of surface-bed linkages highlighted above, a modelling approach is adopted here to better understand the processes at play. Tens of lake and snow models precede this one and range in how comprehensive their treatment of physics is, dependent on their intended end use and the computing capabilities available. This section discusses a selection of previous lake and snow models, their advantages, limitations, and the ways in which this model seeks to adapt and improve upon them. Models are discussed here if they relate to processes focused on by IceLake or are important for background information. Depression filling models such as Leeson et al. (2012) are not included as they are not suitable for inter-annual evolution of lake impact on underlying ice. Examples of other lake models include: Heron and Woo, 1994; Liston and Hall, 1995; Vavrus et al., 1996; Fang and Stefan, 1997; Sergienko and MacAyeal, 2005; Banwell et al., 2012; Koziol et al., 2017

Numerical modelling of cold environment lakes first focussed on meltwater lake formation atop sea ice, with Ebert and Curry (1993) incorporating the physics from Maykut and Untersteiner (1971). Ebert and Curry (1993) placed emphasis on the lakes as they can reduce the sea-ice albedo from 0.85 to 0.1, thereby exerting a large influence on the energy balance and expediting summer melt and break-up. As these lakes can cover up to 50% of the total sea ice area towards the end of the melt season (Scott and Feltham, 2010), they are also of considerable importance to atmospheric general circulation models. The energy balance approach of Ebert and Curry (1993) was improved upon over the decades (Morassutti and LeDrew, 1996; Fetterer and Untersteiner, 1998; Taylor and Feltham, 2004; Skillingstad et al., 2009) culminating in the study by Scott and Feltham (2010). They produced a fully 3-dimensional model for first-year and multi-year sea ice, incorporating meltwater transfer rates from hydraulic gradients based on topography and snow and ice permeability, alongside a 1-dimensional thermodynamic approach (figure 11) which again follows the principles outlined in Maykut and Untersteiner (1971). Flocco et al. (2015) also explicitly model lake freezing atop sea ice as the buried lakes presence reduces basal sea ice accretion to a minimal level, and find that the heightened salinity of the half frozen lake markedly reduces its propensity to freeze further.

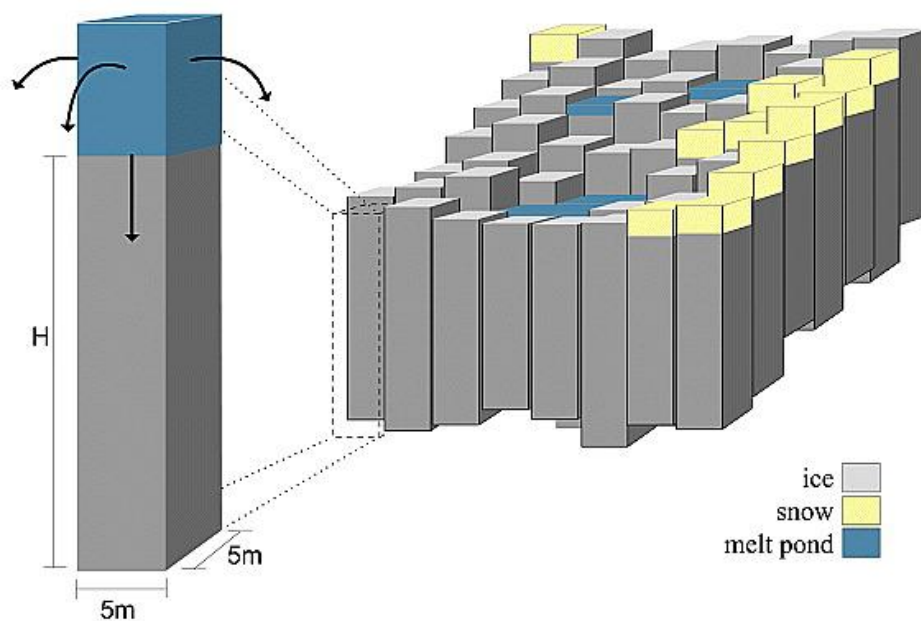


Figure 11: schematic diagram of the cellular structure of the sea ice model of Scott and Feltham (2010).

Modeling of terrestrial, non-ice substrate lakes has also been an active area of research and differs significantly from sea ice lakes due to the absence of brine, static topography, and a variable basal temperature. They are covered here as several include an ice cover module, which is an important component of IceLake. The MyLake model of Lydersen et al. (2003), updated to version 1.2 by Saloranta and Andersen (2007) and originally designed for phosphorus-phytoplankton dynamics, is very well suited to efficiently modelling temperature profiles and the broad behaviour of ice lid formation and break-up, with a 1 year run taking 22 seconds using a 1.6GHz processor. Its temperature profiling module, based on UNESCO (1981) is adapted for IceLake. It runs using a time step of one day, meaning diurnal variation is lost, and treats ice cover as a single layer with an additional layer for snow, and information recorded for refrozen snow, water and snow density. Whilst the temperature of the base of the lake can be set to 0°C, it does not fully replicate ice as it cannot melt or refreeze, thereby influencing the overall energy balance. MyLake has been successfully used in applications such as modelling high-latitude lake thermodynamics (Saloranta et al., 2009) and modelling ice cover in Germany (Livingstone and Adrianb, 2009). Duguay et al. (2002) specifically model lake freeze-up and break-up in the Canadian Arctic, again building on Maykut and Untersteiner (1971), and obtain a mean absolute error for these dates of just 2 days when compared to remotely sensed data. The model they construct is used by Surdu et al. (2014) to model freeze-up rates for permafrost lakes in Alaska, comparable due to the sub-freezing substrate temperature and shallow (~3m) depths. The difference in mean maximum ice thickness difference between their simulations and in situ measurements is just 12cm (6.5%), highlighting the effectiveness of the Maykut and Untersteiner (1971) equations.

Looking at glaciers and ice-sheets, supraglacial lakes are simpler than sea-ice lakes with regard to brine, bathymetry and advancement of model development, but are complicated by a varying, non-freezing basal-boundary condition. Lüthje et al. (2006) presented the first model, deriving their approach from the Ebert and Curry (1993) work outlined above, and using the explicit heat equation discretisation from Alexiades and Solomon (1993). Lüthje et al. (2006) examined the abundance of supraglacial lakes in satellite imagery and combined this with the use of a model to examine the impact of a meltwater column on energy transfer, finding that the basal ablation of lakes is 110–170% that of the immediate surrounding bare ice. MATLAB code from the study by Lüthje et al. (2006) formed the basis for Benedek's (2014) study, which

aimed to better constrain the enhanced melting due to supraglacial lakes on the GrIS through two main improvements: (i) allowing the addition of meltwater from the surrounding catchment, and (ii) extending the length of the shortwave radiation path from the lake surface to the bed, based on refraction at the lake surface using the zenith angle of the sun. Benedek (2014) found that the two implemented changes caused relatively little change to the overall evolution of the melt ponds, with parameter uncertainty (such as surface absorption of shortwave radiation) having a greater impact. The models of Lüthje et al. (2006), Tedesco et al. (2012), and Benedek (2014) were not run for longer than 30 days and there was no incorporation of lid formation, lid collapse, or allowance for a transition from bare ice to water. The explicit discretisation of these models means the time step was held below 6 minutes to avoid numerical instability, resulting in a larger time expenditure than with an implicit scheme.

Buzzard (2017) and Buzzard et al. (2018) examined the development of lakes on the ice shelves of Antarctica and include meltwater addition from the surrounding firn catchment. Buzzard et al. (2018) improved upon the models considered above primarily through the addition of ice lens formation in the firn beneath the lake, which necessitates tracking the density and meltwater content of each cell. These ice lenses are seen in the field on Larsen C ice shelf both through ice pits and ground-penetrating radar (Hubbard et al., 2016) and are also observed in the accumulation zone of Greenland (Forster et al., 2014). These features are of greater importance in Antarctica where lakes almost exclusively form on firn due to the far cooler temperatures than the periphery of the GrIS. Omission of this phenomenon in Antarctica would lead to water immediately pooling on the surface, the lake arising too early, and the depth being too great throughout the season. By obtaining the depth of the lens formation, the maximum depth to which water can percolate could be calculated, and the latent heat release of refreezing meltwater could be fully incorporated. In Greenland, it is acceptable to ignore these firn processes as the vast majority of lakes form below wet snow and firn facies (figure 4). Buzzard et al. (2018) do not account for lid break-up, full lid freezing, or stratification of the lake temperature profile as the profile is reset following 10 days of freezing, a valid approach for Antarctica, but not Greenland.

Of the models discussed above concerning the GrIS, none incorporate snow. Of the remaining models used elsewhere, Buzzard et al. (2018) incorporate it both as an input to the surface of the firn and to the ice lid but not as an input to the lake itself, as the Larsen C ice shelf where the model is tested only has exposed lakes for a matter of weeks. The addition of snow incrementally increases the size of each cell, necessitating a computationally expensive resizing of the entire 1-dimensional array. MyLake is fully suited for snow input, but its 1-day time step and thermodynamic setup makes it ill-suited for adaptation to IceLake. Duguay et al. (2002) do not give clear details of their implementation of a snow layer but do specify that a constant density of  $350 \text{ kg m}^3$  is used and that the presence of snow has an important implication for break-up dates. As IceLake departs from the snow-firn-ice continuum of Buzzard et al. (2018) by treating snow and ice separately, and from MyLake by using a shorter time step and discrete cell-based approach, it was important to find a separate snowpack model that could be coupled to a pure-ice substrate.

Snowmelt models generally take a degree-day approach (or a time step greater than one day) and comprise three stages: first, the temperature of the snowpack becomes isothermal at the melting point; second, melt occurs, and the snow becomes fully saturated; third, extra melt generated leaves the snowpack and the snow ultimately vanishes (e.g. Braithwaite 1995; Boone and Etchevers, 2001; Liston and Elder, 2006; Valery 2010; Troin et al., 2015). If the snow is falling on a frozen surface in a lake hollow depression before melt, or the planar surface of an ice lid, however, the third stage would not apply and evacuation of water would be either impossible or stymied. It would also be possible for this meltwater to be refrozen due either to diurnal temperature variations or diffusion of heat downwards into the ice column. For these reasons, an existing snowpack model compatible with the time step and discretisation of the ice column needed to be adapted. The Factorial Snowpack Model (FSM) of Essery (2015), a multi-layer energy-flux model written in Fortran, was ultimately chosen as a base due to the clear documentation of the equations used therein and the associated robust testing of its performance. Further details of this model, its implementation and its adaptation are provided in the methods section.

## **Methods**

The model was written in MATLAB using equations derived here and source code adapted from Benedek (2014), Buzzard et al. (2018), Saloranta and Andersen (2007) and Essery (2015). To improve efficiency, for-loops were removed wherever possible and interpolants were avoided. The model is divided into five stages (figures 12 and 13 and table 1). Movement between the stages and simplified modules at each stage are detailed in figure y. In addition, stage 3.5 was created to mimic bare ice melt excluding water, following Benedek (2014). The model was developed using weather data from the Programme for Monitoring of the Greenland Ice Sheet (PROMICE, van As et al., 2011). The AWS UPE-U, at an elevation of 980 m a.s.l., was used since the record for this station was the most comprehensive of any PROMICE station in the ablation zone of the GrIS (figure 14).

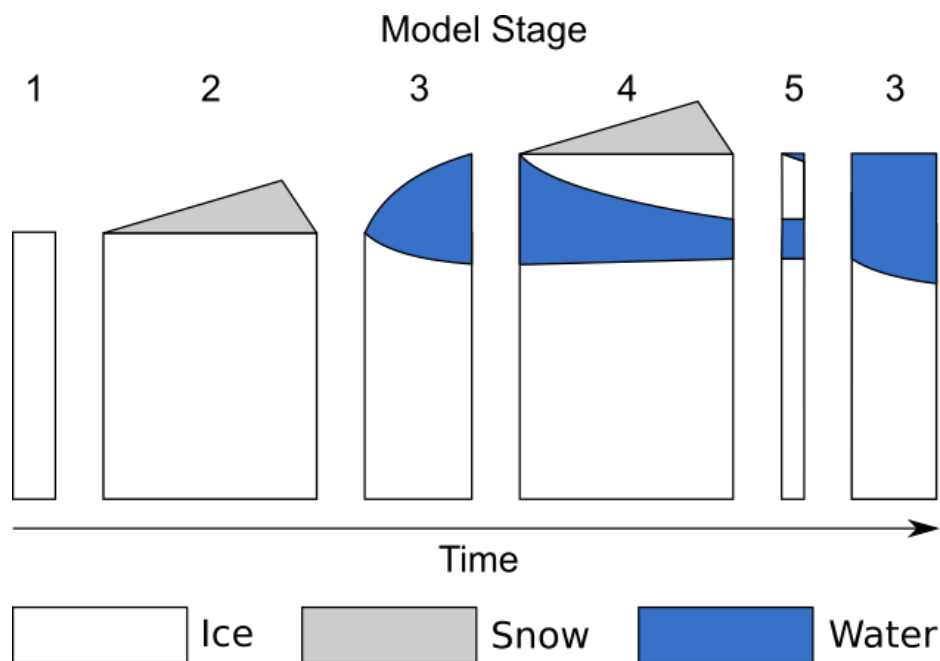


Figure 12: schematic illustration of model stages. Table y provides details of each stage. The model does not necessarily need to progress through the stages in numerically chronological order, as detailed in figure 13. Stage 3 is included twice to show year-on-year continuity of IceLake.

Stage	Description
1	Bare ice, no surface snow cover.
2	Snow layer present on top of ice.
3	Lake present above ice.

4	Snow lid overlying lake with snow present above.
5	Lid break-up after snowmelt.

Table 1, description of model stages.

<p><b>(start)</b></p> <p>Import AWS, precipitation, and hydrograph data based on user-specified run time and time step</p> <p>Initialise arrays, set trackers so that correct modules are used, model stage set as 1</p> <p><b>Main loop</b></p> <p><b>If model stage = 1</b></p> <p>Calculate surface energy flux   Phase tracking   Heat diffusion</p> <p>If sufficient snow has fallen to commence snow layer, move to stage 2</p> <p>If top cell is entirely water, move to stage 3</p> <p><b>If model stage = 2</b></p> <p>Incorporate incoming precipitation   Calculate snow melt if required based on phase tracking from previous time step   Update snow layer density, heat capacity, conductivity and albedo   Calculate surface energy flux   Phase tracking   Heat diffusion</p> <p>If snow has melted, move to stage 3</p> <p><b>If model stage = 3</b></p> <p>Incorporate incoming precipitation and hydrograph into lake insert   Calculate surface energy flux and shortwave propagation   Phase tracking   Lake indexing   Temperature profile   Turbulence   Heat diffusion</p> <p>If surface cell has become ice and sufficient snow has fallen to commence snow layer, move to stage 4</p> <p><b>If model stage = 4</b></p> <p>Incorporate incoming precipitation   Calculate snow melt if required based on phase tracking from previous time step   Update snow-layer density, heat capacity, conductivity and albedo   Calculate surface energy flux   Phase tracking   Lake indexing   Temperature profile   Turbulence   Heat diffusion</p> <p>If lake has frozen, move to stage 2</p> <p>If lid is unstable trigger break-up and move to stage 3</p> <p>If snow has melted, move to stage 5</p> <p><b>If model stage = 5</b></p> <p>Calculate surface energy flux   Phase tracking   Lake indexing (two lakes)   Temperature profiles   Turbulence   Heat diffusion</p> <p>If lid is unstable trigger break-up and move to stage 3</p> <p>Plot figures</p>
--

Figure 13: simplified code structure. Description of modules calculated at each model stage in the order upon which they are called (orange), conditions for moving to another stage (green), and processes conducted outside the main loop (black).

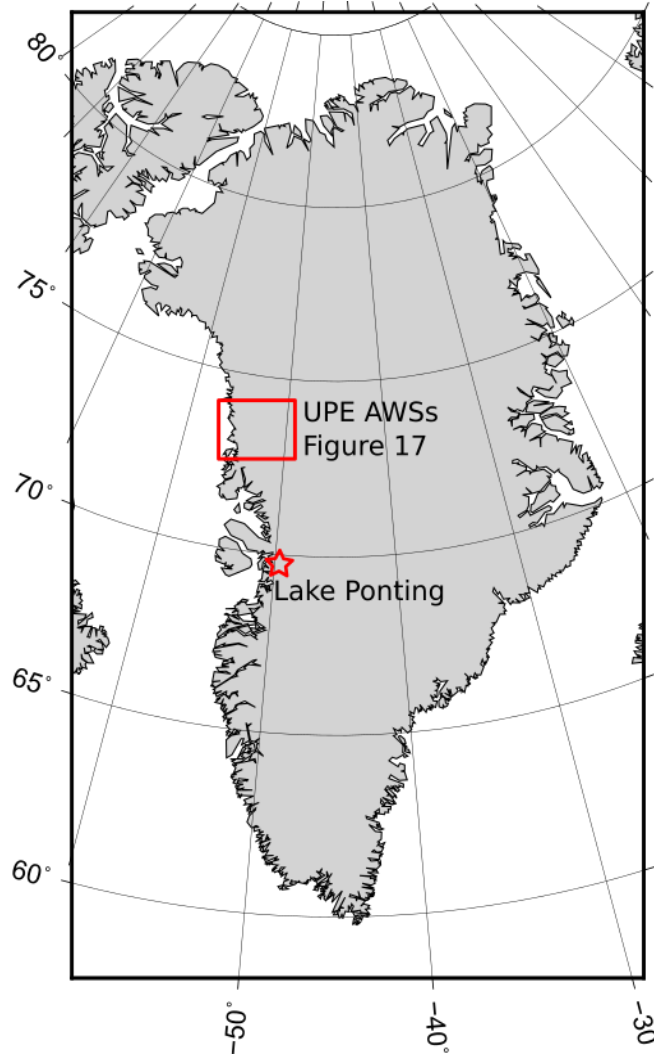


Figure 14: Location of PROMICE AWSs, figure 17 and Lake Ponting.

### Surface energy flux

Surface energy flux in  $\text{W m}^{-2}$  is calculated after Buzzard (2017), who follows Ebert and Curry (1993), as

$$F_{total} = \varepsilon F_{LW_{in}} + (1 - \alpha) F_{SW} - \varepsilon \sigma T^4 + F_{sens} + F_{lat} \quad (1)$$

where:

$\epsilon$	= emissivity
$F_{LWin}$	= incoming longwave radiation ( $W m^{-2}$ )
$\alpha$	= albedo
$F_{SW}$	= incoming shortwave radiation ( $W m^{-2}$ )
$\sigma$	= Stefan-Boltzmann constant ( $W m^{-2} K^{-4}$ )
$T$	= temperature (K)
$F_{sen}$	= sensible heat flux ( $W m^{-2}$ )
$F_{lat}$	= latent heat flux ( $W m^{-2}$ )

All calculations assume a cross-sectional area of  $1 m^2$ , as a scaling factor would cancel out under the assumption of uniform cross-sectional area throughout the profile. This follows Ebert and Curry (1993) and models based upon their methods, but diverges from Saloranta and Andersen (2003)). Sensible and latent heat fluxes are calculated as

$$F_{sens} = \rho_a c_p^{air} C_T v (T_a - T_0) \quad (2)$$

$$F_{lat} = \rho_a L_v C_T v (q_a - q_0) \quad (3)$$

where:

$\rho_{air}$	= density of dry air ( $kg m^{-3}$ )
$c_p^{air}$	= specific heat capacity of dry air ( $kJ kg^{-1} K^{-1}$ )
$v$	= wind speed ( $m s^{-1}$ )
$T_a$	= air temperature
$T_0$	= surface temperature
$L_v$	= latent heat of vaporisation ( $J kg^{-1}$ )

using a  $C_T$  (function of atmospheric stability) calculated using equations 2.12-2.14 of Buzzard (2017). Humidity measurements are provided as relative humidity (%) by the PROMICE weather stations and the data of Benedek (2014). This is converted to specific humidity by

first obtaining the saturation vapour pressure,  $e_s(T)$  at temperature  $T$  (in degrees), following Tetens (1930).

$$e_s(T) = 610.78e^{\frac{17.2694T}{T+238.3}} \quad (4)$$

Vapour pressure is obtained using the definition of relative humidity

$$e = RHe_s \quad (5)$$

where:

RH = relative humidity (0-1)

The mixing ratio of water vapour,  $w$ , is calculated from AMS (2012) as

$$w = \frac{eR_d}{R_v(p - e)} \quad (6)$$

where:

$p$  = pressure (Pa)

$R_d$  = specific gas constant for dry air ( $\text{Jkg}^{-1}\text{K}^{-1}$ )

$R_v$  = specific gas constant for water vapor ( $\text{Jkg}^{-1}\text{K}^{-1}$ )

Lastly the specific humidity,  $q$ , is obtained using AMS (2012), as

$$q = \frac{w}{w + 1} \quad (7)$$

#### Shortwave radiation propagation through water and ice

Transfer of shortwave radiation through water and ice was accounted for using the Beer-Lambert law following Benedek (2014) as

$$F_i = F_b e^{-\tau z_i} - F_b e^{-\tau z_{i+1}} \quad (8)$$

where:

- $F_i$  = flux at cell  $i$  ( $\text{W m}^{-2}$ )
- $T$  = shortwave extinction coefficient ( $\text{m}^{-1}$ )
- $z_i$  = depth of cell  $i$  (or  $i + 1$ )

$F_b$  was calculated for the water surface as

$$F_b = I_0(1 - \alpha)F_{sw} \quad (9)$$

where:

- $I_0$  = proportion of shortwave radiation absorbed at the surface

The path length for incoming shortwave radiation through the water, calculated from the angle of incidence of incoming shortwave and the refractive index of water, was not included as it was not found to be important by Benedek (2014) (figure 15). All remaining shortwave was absorbed in the topmost ice layer following Lüthje et al. (2006).

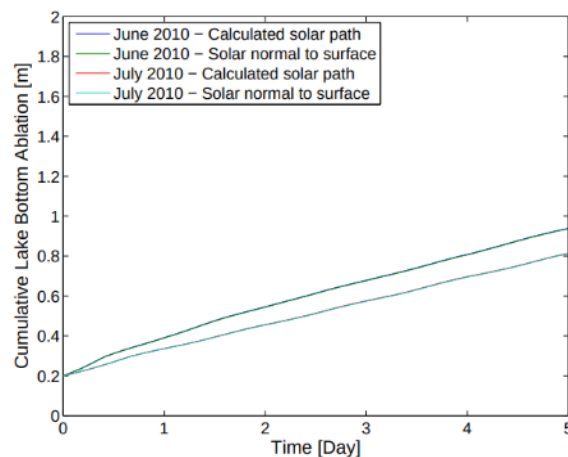


Figure 15: effect of calculating solar path on lake bottom ablation. The two clearly distinct lines are both actually two lines, showing the very minor impact of changing the path length. From Benedek (2014).

### Phase tracking

A phase-tracking approach was used to derive enthalpy from temperature and vice versa following Benedek (2014) and Lüthje et al. (2006). The enthalpy of an ice cell at melting point with heat capacity  $C_i$  and depth  $z_i$  is

$$E_{ice_i} = \rho_{water} C_i z_i T_{melt} \quad (10)$$

where:

$\rho_{water}$  = density of water ( $\text{kg m}^3$ )

$T_{melt}$  = freezing point of water (K)

And the enthalpy of a water cell at freezing point is

$$E_{water_i} = \rho_{water} z_i (C_i T_{melt} + L_f) \quad (11)$$

where:

$L_f$  = latent heat of fusion of ice ( $\text{J kg}^{-1}$ )

The density of water is used for ice, slush and water following Lüthje (2005), Benedek (2014), and Buzzard (2017) to avoid a change in cell depth with phase. As the difference is small (11%), the impact is assumed to be insignificant. Temperature is then calculated based on the cell's enthalpy as below, or in reverse if necessary

$$\begin{cases} T_i = \frac{E_i}{\rho_{water} C_{ice} z_i} & \text{if } E_i < E_{ice_i} \\ T_i = T_{melt} & \text{if } E_{ice_i} < E_i < E_{water_i} \\ T_i = \frac{E_i}{\rho_{water} C_{ice} z_i} - \frac{1}{C_{water}} (C_{ice} T_{melt} + L_f - C_{water} T_{melt}) & \text{if } E_i > E_{water_i} \end{cases} \quad (12)$$

The proportion of each cell that is water  $\lambda_i$ , is calculated as

$$\begin{cases} \lambda_i = 0 & \text{if } E_i < E_{ice_i} \\ \lambda_i = \frac{E_i - \rho_{water} C_{ice} z_i T_{melt}}{L_f \rho_{water} z_i} & \text{if } E_{ice_i} < E_i < E_{water_i} \\ \lambda_i = 1 & \text{if } E_i > E_{water_i} \end{cases} \quad (13)$$

### Lake convection

Following Taylor and Feltham (2004), the lake is modelled as turbulently convective at 0.1m depth: the smallest depth that can be modelled under the default grid depth. Two schemes are accounted for in this approach: a homogenous lake temperature following Benedek (2004) and Buzzard (2017), and a stratified temperature profile following Saloranta and Andersen (2007). The homogenous temperature profile takes the average lake enthalpy and applies it to all lake cells. However, as cooler water has lower density below 4 °C and is therefore at the top of the profile under the cold conditions considered here, a homogenous temperature profile may not accurately represent the downward encroachment of an ice lid. The stratified approach of Saloranta and Andersen (2007) utilises the International Equation of State of Seawater (IES-80, UNESCO, 1981), which calculates the density of water based on its temperature, depth and, if necessary, salinity. The stratified temperature profile is used for lake depths above 0.7 m.

### Lake albedo

Lake albedo follows the scheme of Lüthje et al. (2006) and is calculated as

$$\alpha = \frac{9702 + 1000e^{3.6z_l}}{-539 + 20000e^{3.6z_l}} \quad (14)$$

where:

$z_l$  = lake depth

giving an exponentially decreasing lake albedo with increasing depth.

### Indexing and turbulence

Turbulent mixing is expected in lakes with even slightly heterogeneous temperature profiles and acts to enhance heat exchange between water-ice and water-air boundaries (Taylor and Feltham, 2004). In order to apply turbulent convection to the correct section of the profile, it was important to index lake location correctly, especially as water can form atop the lid prior to collapse. This was implemented by progressing upwards from the base of the domain and recording the first and last instances of water between ice sections. This prevented two lakes being separated due to the transient appearance of one slush cell in the middle of the lake and encourages slush and ice encroachment from the upper and lower bounds of the lake. An allowance was made for a lid comprised entirely of slush cells at the start of the melt season by setting a minimum number of slush cells above a set value of  $\lambda$  as a threshold for a lid.

Turbulent heat flux,  $F_{turb}$  ( $\text{W m}^{-2}$ ), at a boundary of temperature  $T^*$  (K), is calculated following Buzzard (2017) as

$$F_{turb}(T^*) = \text{sign}(\bar{T} - T^*) \rho_{water} c_{water} J \left| \bar{T} - T^* \right|^{\frac{4}{3}} \quad (15)$$

where:

$$\bar{T} = \text{average lake temperature (K)}$$

and applied to the first slush or ice cell immediately surrounding the lake or incorporated into the overall surface energy transfer. Applying the turbulent flux to the first ice cell resulted in unrealistic lake growth with an unstable slush buffer zone.

### Snow

Snow-layer modelling broadly follows the approach of Essery (2015); however, notable changes were made in the process of adapting the source code from Fortran to MATLAB.

Importantly, one layer is used here, although the code is structured to allow easy implementation of an additional two layers. Additionally, The snow layer here is designed to be coupled to ice rather than soil as implemented by Essery (2015). Calculations for snow are conducted at the beginning of each time step, to allow them to be used subsequently in the conduction subfunction. When the snow-layer is first added, the conductivity of the snow,  $K_s$ , is initialised as

$$K_s = \frac{\rho_{s_{new}}}{\rho_{water}} K_{ice} + \left(1 - \frac{\rho_{s_{new}}}{\rho_{water}}\right) K_{air} \quad (16)$$

where:

- $\rho_{s_{new}}$  = density of fresh snow
- $K_{air}$  = thermal conductivity of air

The albedo is set at the new snow value. The snow temperature is set as 0 °C if the air temperature is above freezing, and as the air temperature if the air temperature is below freezing. Following initialisations,  $K_s$  is calculated following Essery (2015) as

$$K_s = K_{ice} \left(\frac{\rho_s}{\rho_{ice}}\right)^b \quad (17)$$

where:

- $\rho_s$  = current density of snow layer
- $b$  = use specified exponent originally set as 2 (Essery, 2015)

$\rho_{ice}$  is used here even though  $\rho_{water}$  is used in most other situations as its use here does not complicate depth calculations. The snow depth,  $x_{snow}$ , is calculated initially, and subsequently for all following time steps as

$$x_{snow} = S_{mwe} \mu_s + S_{mwe} (1 - \mu_s) (1 - \lambda_s) \left(\frac{\rho_{water}}{\rho_s}\right) \quad (18)$$

where:

- $S_{mwe}$  = snow layer metres water equivalent
- $\mu_s$  = proportion of snow layer which is snow-ice
- $\lambda_s$  = proportion of snow layer which is water

This assumes that the first term, snow-ice, which is defined as refrozen meltwater in the snow layer, displaces snow that is placed above it to simplify calculations. The heat capacity of the snow  $C_s$  is calculated initially and subsequently as

$$C_s = \mu_s C_{ice} + (1 - (\mu_s + \lambda_s)) C_{ice} + \lambda_s C_{water} \quad (19)$$

where:

- $\mu_s$  = proportion of snow layer which is snow-ice
- $\lambda_s$  = proportion of snow layer which is water
- $C_{ice}$  = heat capacity of ice
- $C_{water}$  = heat capacity of water

$\lambda_s$  is initially set as 0 (no water), then updated to include incoming snow at the start of the time step and recalculated at the end of the time step using the same enthalpy approach as equation x.  $\mu_s$  is initially set as 0 (no snow-ice) and is calculated subsequently if  $\lambda_s$  is seen to decrease as the difference between the new and old  $\lambda_s$

$$\mu_s^{n+1} = \mu_s^n + \lambda_s^n - \lambda_s^{n+1} \quad (20)$$

The density of snow at the start of each time step, after initialisation where it is set as  $\rho_{snew}$ , is calculated as

$$\rho_s^n = \frac{\rho_{snew}^n S_{in}^n + \rho_s^{n-1} S_{mwe}^{n-1}}{S_{mwe}^n} \quad (21)$$

where  $S_{mwe}^n$  already incorporates the water-equivalent depth of the incoming snow.  $\rho_s$  is updated to account for snow compaction at each time step as

$$\rho_s^n = \rho_{max} + (\rho_s^{n-1} - \rho_{max})e^{\frac{-\Delta t}{T_\rho}} \quad (22)$$

where:

- $\rho_{max}$  = maximum density of melting snow if air temperature is above freezing and maximum density of cold snow if air temperature is below freezing ( $\text{kg m}^{-3}$ )
- $\Delta t$  = time step (s)
- $T_\rho$  = snow compaction timescale (s)

integrated from equation 19 of Essery (2015). Albedo is available from the PROMICE AWSs and this can be used if the 'AWS\_albedo' switch is triggered. If not, it is calculated as an exponential-decay function with a rate dependent on snow state (i.e. melting or not melting) and held between a maximum and minimum value (Essery 2015, equation 10). The snow layer is terminated when  $\mu_s + \lambda_s \geq 1$ , and temperature and depth information is passed on for lake initialisation.

#### Initial temperature profile

By default, the model is initialised as an ice column with temperature linearly interpolated between a surface and basal temperature specified by the model user. Alternatively, if the 'import\_core' switch is triggered, data for core 4 or core 5 (at surface elevations of 849 m or 1090 m, respectively) from Harrington et al. (2015) for Isunnguata Sermia Glacier (68.4°N) on the west coast is imported. However, the resolution of the upper 20 m of these cores is low and the sign of the gradient varies between the cores.

#### Grid setup and lake and snow inserts

In order to allow for a varying domain depth as a result of incoming water and snow, inserts were constructed for additional lake depth and snow cover (figure 16). The flexible depth cell of Benedek (2014) was not used as it later obscured lid depth and formation rate. These were concatenated before heat diffusion and separated afterwards at each time step in order to avoid computationally expensive resizing. Once the maximum (user-specified) lake depth is reached, or hydrograph input ceases for the season, the lake insert is combined with the main profile to simplify code later in the model run. The snow layer is kept apart throughout due to a fundamentally different approach, but ice and water are added from it to the main column after snow melt. To avoid complication, surface energy flux is applied to the top cell of the original column if the lake insert is used, but is applied to the snow cell directly when in use.

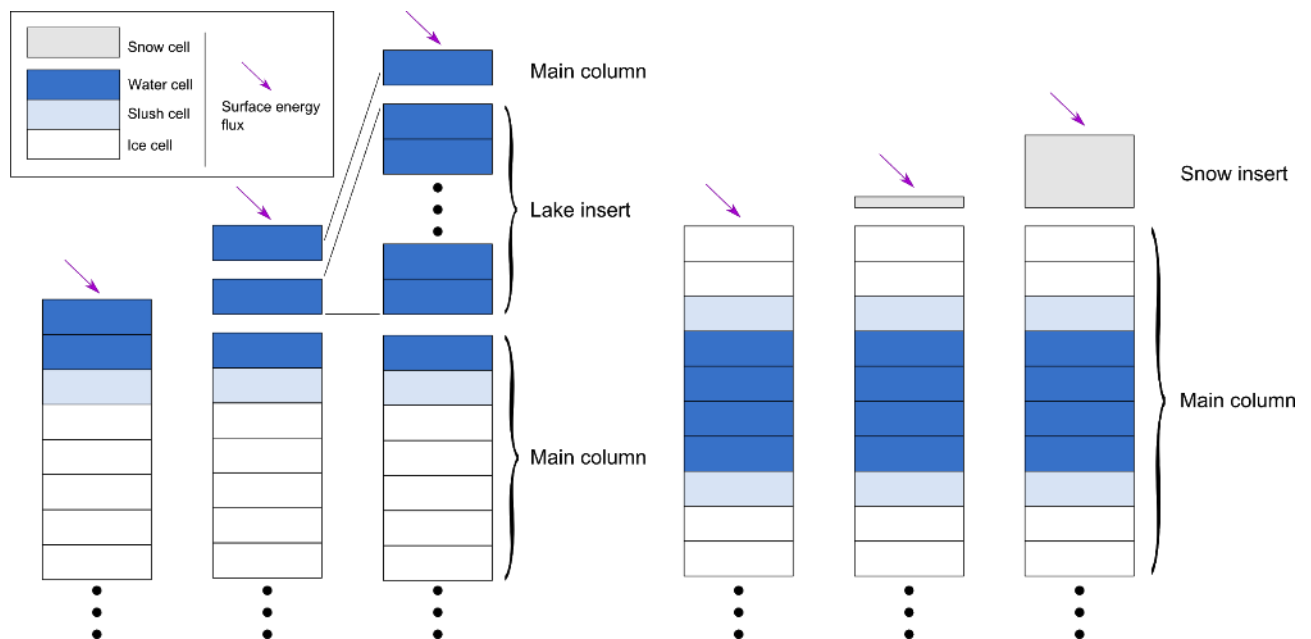


Figure 16: construction of lake and snow inserts. Lake insert size is increased discretely whereas snow insert size is increased continuously.

To reduce the impact of the basal Dirichlet boundary on the energy balance of the lake, while maintaining good computational efficiency, the default size of the lowest 10 cells was enlarged from 10 cm to 1 m to increase the overall domain depth. These values can be easily modified by the model user if required.

## Heat diffusion

Heat diffusion within the model is carried out using a backward-time, centered-space approach, with enthalpy change calculated from the difference in temperature for each cell at each time step. This approach was selected as it allows much longer (>20 times) time steps whilst maintaining numerical stability when compared with calculating the energy flux for each time step using Fourier's Law, as for Benedek (2014) following Alexiades and Solomon (1993). It is also markedly faster than using the in-built MATLAB pdepe function as used in Buzzard (2017). The heat diffusion equation

$$\frac{\partial T}{\partial t} = K \frac{\partial^2 T}{\partial x^2} \quad (23)$$

where:

- T = temperature (K)
- t = time (s)
- K = thermal conductivity (Wm<sup>-1</sup>K<sup>-1</sup>)
- x = depth (m)

is discretised in 1-dimension to allow for non-uniform layer spacing as a result of lake hydrograph input, snowfall, and larger deep cells as follows

$$\frac{T_i^{n+1} - T_i^n}{\Delta t} = K_{i+\frac{1}{2}}^{n+1} \frac{T_{i+1}^{n+1} - T_i^n}{(\Delta x_{i+\frac{1}{2}}^{n+1})^2} - K_{i-\frac{1}{2}}^{n+1} \frac{T_i^{n+1} - T_{i-1}^n}{(\Delta x_{i-\frac{1}{2}}^{n+1})^2} \quad (24)$$

where:

- n = time step
- i = cell index
- Δx = distance between the midpoints of two adjacent cells (m)
- Δt = time step (s)

This is simplified by creating the  $S_i^{n+1}$  term and relaying it into equation x to give equation y

$$S_i^{n+1} = k_i^{n+1} \frac{\Delta t}{(\Delta x_i^{n+1})^2} \quad (25)$$

$$T_i^{n+1} = T_i^n - S_{i+\frac{1}{2}}^{n+1}(T_{i+1}^{n+1} - T_i^{n+1}) - S_{i-\frac{1}{2}}^{n+1}(T_i^{n+1} - T_{i-1}^{n+1}) \quad (26)$$

Making  $T_i^n$  the subject gives

$$T_i^n = -S_{i+\frac{1}{2}}^{n+1}U_{i+1}^{n+1} + (1 + S_{i+\frac{1}{2}}^{n+1} + S_{i-\frac{1}{2}}^{n+1})T_i^{n+1} - S_{i-\frac{1}{2}}^{n+1}T_{i-1}^{n+1} \quad (27)$$

which can then be entered into a system of simultaneous equations using a tridiagonal matrix generalised to a given number of model layers and solved as a matrix equation. Dirichlet boundary conditions are applied at top and bottom and atmospheric heat flux is prescribed earlier in the time step (equation x). This is contrary to the Neumann basal boundary condition used by Buzzard (2017), but is deemed suitable due to the uncertainty in basal boundary condition that would remain even with a Neumann condition. Meierbachtol et al. (2015) also suggest a fairly constant ( $\pm 1$  °C) ice temperature at depths below 12 m from the ice surface.

$$\begin{bmatrix} 1 & 0 & 0 & \cdot & \cdot & \cdot & \cdot & \cdot \\ -S_{1-\frac{1}{2}}^{n+1} & (1 + S_{1-\frac{1}{2}}^{n+1} + S_{1+\frac{1}{2}}^{n+1}) & -S_{1+\frac{1}{2}}^{n+1} & \cdot & \cdot & \cdot & \cdot & \cdot \\ 0 & -S_{2-\frac{1}{2}}^{n+1} & (1 + S_{2-\frac{1}{2}}^{n+1} + S_{2+\frac{1}{2}}^{n+1}) & \cdot & \cdot & \cdot & \cdot & \cdot \\ \cdot & \cdot \\ \cdot & \cdot & \cdot & (1 + S_{j-2\frac{1}{2}}^{n+1} + S_{j-1\frac{1}{2}}^{n+1}) & -S_{j-1\frac{1}{2}}^{n+1} & 0 & \cdot & \cdot \\ \cdot & \cdot & \cdot & -S_{j-1\frac{1}{2}}^{n+1} & (1 + S_{j-1\frac{1}{2}}^{n+1} + S_{j-\frac{1}{2}}^{n+1}) & -S_{j-\frac{1}{2}}^{n+1} & \cdot & \cdot \\ \cdot & \cdot & \cdot & 0 & 0 & 1 & \cdot & \cdot \end{bmatrix} \cdot \begin{bmatrix} T_1^{n+1} \\ T_2^{n+1} \\ T_3^{n+1} \\ \cdot \\ T_{j-2}^{n+1} \\ T_{j-1}^{n+1} \\ T_j^{n+1} \end{bmatrix} = \begin{bmatrix} T_1^n \\ T_2^n \\ T_3^n \\ \cdot \\ T_{j-2}^n \\ T_{j-1}^n \\ T_j^n \end{bmatrix} \quad (28)$$

Lastly, the change in enthalpy is obtained from the difference in heat and added to the existing enthalpy profile. Change in enthalpy,  $\Delta E$ , at each grid step is calculated as

$$\Delta E = (T_i^{n+1} - T_i^n)C_i^n x_i^n \rho_{water} \quad (29)$$

where:

$$x_i^n = \text{height of cell}$$

The thermal conductivity and heat capacity for each cell are calculated using equations x and x, respectively, and the intermediate values between cells are obtained as the depth weighted average.

$$K_i = \lambda_i K_{water} + (1 - \lambda_i) K_{ice} \quad (30)$$

$$C_i = \lambda_i C_{water} + (1 - \lambda_i) C_{ice} \quad (31)$$

### Hydrograph input

Hydrograph data from Arnold et al. (2014) or Tedesco et al. (2012) are used to input water into the lake. The data is provided in  $\text{m}^3 \text{h}^{-1}$  and scaled to the surface area of the lake, as specified by the user, to replicate a lake of variable size. Precipitation and hydrograph input are stored in a holding bucket until their sum is sufficient to fill an entire new grid cell. While the buckets are filling, their enthalpy is averaged based on incoming water temperature if water or precipitation is added. The weighted average of both buckets when combined is then used as the initial enthalpy when a new cell is added to the lake insert. It would be possible to incrementally increase the depth of each cell of the lake, but this would interfere with temperature-profile calculations, increase run time, and would be unlikely to create a notably more accurate model as the sum hydrograph input is later shown to be the more important for lake freeze-up. The incoming water temperature of the hydrograph input can be set by the user and has a default value of  $0.001 \text{ }^\circ\text{C}$ , discussed in further detail in the discussion. For precipitation input, if the air temperature is above freezing, incoming precipitation is added at the air temperature; if the air temperature is below freezing then it is added at  $0^\circ\text{C}$ . When the lake is present, all precipitation is treated as rain; this is a reasonable assumption given as incoming water temperature is shown to have little impact on model output.

### Sensitivity testing

A short model run time means a large parameter space can be explored without a large time expenditure. For the model sensitivity testing, 20 values, extending slightly beyond the expected range of the parameters, were tested for 12 different parameters and used to

obtain a normalised sensitivity coefficient and to construct graphs of output variability. Nine output variables, described in table 2 and chosen to capture as wide a range of model behaviour as possible, were chosen to quantify the sensitivity of model output to parameter variation. The time for recording lake depth before and after lid formation was calculated based on a temperature proxy to avoid slush behaviour associated with lid formation and break-up. If the temperature passed a 0.05 °C threshold for at least 100 time steps, it was assumed that the model had transitioned from no lid to lid, or vice versa. Visual inspection of results showed that this assumption held true for all tests conducted.

The parameters tested fall into two classes: (i) the parameter value is uncertain because it is a result of uncertain knowledge or modelling of the surrounding environment (for example, incoming water temperature and the  $I_0$  term); (ii) there may be uncertainty or error in the instruments used to record the data (for example, albedo measured at the AWS). Under this classification temperature, shortwave and longwave radiation would fall under instrumental uncertainty but they are excluded as they form the focus of the elevation-evolution study.

Variable	Explanation
Lake depth before lid formation (m)	The depth of the lake at the end of the first melt season, before freeze-up. This was used in place of lake bottom ablation rate to avoid the assumption that lake bottom ablation is linear.
Time of lid formation (days)	The day at which lake depth before lid formation was obtained.
Lake depth after snow melt, before lid break-up (m)	The depth of the lake when all snow atop the lid has melted. This generally occurs a few days to a week before lid break-up and is chosen to avoid interference with the lid break-up process. The difference between this value and the lake depth before lid formation gives the degree of freeze-up.
Time of snowmelt (days)	The corresponding day on which full snowmelt occurs.
Lake depth after lid break-up (m)	The depth of the lake at the start of the second melt season, after the lid has fully broken up.
Time of lid break-up (days)	The corresponding day on which the lid has fully broken up.
Maximum average temperature of lake before lid formation (°C)	The maximum average temperature of the entire water column from the time of first melt occurrence to lid formation for the first melt season.

Maximum average temperature of lake after lid break-up (°C)	As above but from lid break-up until lid formation for the second melt season.
Time of first lake formation (days)	When model stage 3 is first reached.

Table 2: explanations of variables collected after each run.

The sensitivity coefficient was calculated following Loucks et al. (2005) and normalised with the  $\frac{P_0}{Q(P_0)}$  term to allow direct comparison. The initial value of the parameter was based on either previous studies or taken as a reasonable estimate if no studies were available. All initial parameters and are available in appendix 3.

$$\frac{|Q(P_0 + \Delta P) - Q(P_0 - \Delta P)|}{2\Delta P} \times \frac{P_0}{Q(P_0)} \quad (32)$$

where:

- $Q(P_0 + \Delta P)$  = output value Q when forced with a parameter value of  $P_0 + \Delta P$
- $P_0$  = initial parameter value
- $\Delta P$  = assumed reasonable positive or negative variation from  $P_0$

#### Model validation: comparison to Tedesco et al. (2012)

To validate the model, it was compared to field data collected by Tedesco et al. (2012) in 2011 for Lake Ponting (69.589°N, 49.783°W, figure 14), using July 2010 – July 2011 AWS weather data from Benedek (2014). No incoming longwave data is available in Benedek (2014), so it was calculated following Lüthje et al. (2006) and Benedek (2014) as

$$F_{LW_{in}} = [\varepsilon_{cs}(1 - n^p) + \varepsilon_{oc}n^p] \sigma T_{air}^4 \quad (33)$$

where:

- $\varepsilon_{cs}$  = clear-sky emissivity
- $n$  = cloudiness, assumed to be 0.6 by Lüthje et al. (2006)

- $p = 4$  (constant)  
 $\epsilon_{oc}$  = overcast-sky emissivity, assumed to be 0.952 by Lüthje et al. (2006)

with  $\epsilon_{cs}$  calculated as

$$\epsilon_{cs} = 0.23 + b \left( \frac{e_{air}}{T_{air}} \right)^{\frac{1}{m}} \quad (34)$$

where:

- $b = 0.484$  (constant)  
 $m = 8$  (constant)

The impact of using incoming longwave radiation as calculated above was determined by running IceLake with UPE-U AWS data including and then excluding derived incoming longwave radiation. The model was run for one year, commencing on 26<sup>th</sup> July 2010, although Lake Ponting drained on 19<sup>th</sup> June 2011. The hydrograph input recorded by Tedesco et al. (2012) was used so that the lake depth would be directly comparable. Basal melt was calculated by subtracting hydrograph input from overall lake depth. The  $I_0$  value, the most poorly constrained parameter, and most sensitive parameter (see discussion) was tweaked to obtain the closest match between observations and modelling. The model was also run in the absence of any overlying meltwater to determine the difference in lake-bottom melt rates between a lake overlying ice and a bare ice surface. Here, the water was allowed to remain above the ice but was excluded in all calculations, following Benedek (2014).

#### Model inter-comparison with Buzzard et al. (2018)

The model of Buzzard et al. (2018) was also run using forcing data for Lake Ponting from July 2010 – July 2011 to compare model output, using a 1-year spin-up with repeating AWS data to reduce spin-up errors. A spin-up period was not used for IceLake as it functioned well without this requirement, and since the full lake developed in the previous melt season would persist over winter, whereas Buzzard et al. (2018) reset the profile after 10 days of

consecutive freezing following lid formation. Buzzard et al.'s (2018) model was run using the incoming longwave data calculated through IceLake with the AWS data from Benedek (2014).

### Endless winter

In order to observe lake freeze-up behaviour for deep (> 5 m) lakes, the lid was allowed to form normally using UPE-U PROMICE AWS data, but was then forced using data from 02:00, 1<sup>st</sup> February on repeat from the 5<sup>th</sup> of April 2010 onwards.

### Application: lapse rate and RACMO elevation profile

In order to test the impact of elevation on the evolution of supraglacial lakes, and so to generate the first set of glaciological findings from applying the model, forcing data for an elevational transect were needed. Such data could be acquired either by applying lapse-rate transfers to each input using available AWS data, or by using a regional climate model such as MAR (Modèle Atmosphérique Régional, Fettweis et al., 2012) or RACMO2.3p2 (Regional Atmospheric Climate Model, Noël et al., 2018), which are in turn forced by atmospheric reanalysis data such as ERA-Interim (Dee et al., 2011) or CRU TS (Harris et al., 2014). The benefit of the latter is that once configured, the model can be run over large areas, that the data have already been rigorously tested and published, and that errors and inconsistencies are generally well documented. The large-scale approach does mean, however, that climate model and reanalysis data tend to be consistently less accurate than AWS data. These errors range from reasonably consistent 1–2 °C temperature differences throughout the year (ERA-Interim) to seasonal errors exceeding 4 °C (MAR, Eyre and Zeng, 2017), shortcomings in cloud prediction that strongly influence radiation readings (Bennartz et al., 2013), errors in longwave radiation (Cox et al., 2014), and significant (34%) inter-model variability in surface mass balance predictions (Vernon et al., 2013). RACMO2.3p2 data were ultimately chosen for the purposes of this study due to high resolution (~11 km), necessary for deriving a fine set of samples across the elevational transect, and as the RACMO data products generally compare well with *in situ* data (Ettema et al., 2010; Noël et al., 2018). Lapse-rate transfers were not used as data uncertainty would be difficult to constrain and the model would be

limited to one location. In addition, lapse rates vary seasonally, diurnally and spatially as a function of wind speed and moisture content (Minder et al., 2010; Kattel et al., 2013).

A 154 km transect at Upernavik Isstrøm Glacier (72.8°N) in western Greenland was used, comprising 14 RACMO data cells from 130 to 2,208 m a.s.l.. This transect was selected as it runs through the PROMICE UPE-U AWS (figure 17) allowing results from the two data sources to be compared over the same time period to provide an indicator of output uncertainty. This was done with one year from 1<sup>st</sup> January 2009, under the assumption that the UPE-U data is more accurate as it is collected *in situ*. Data for lake formation day, lake depth at the end of the first melt season, lid formation day, lid break-up day, and maximum ice-lid thickness was recorded.

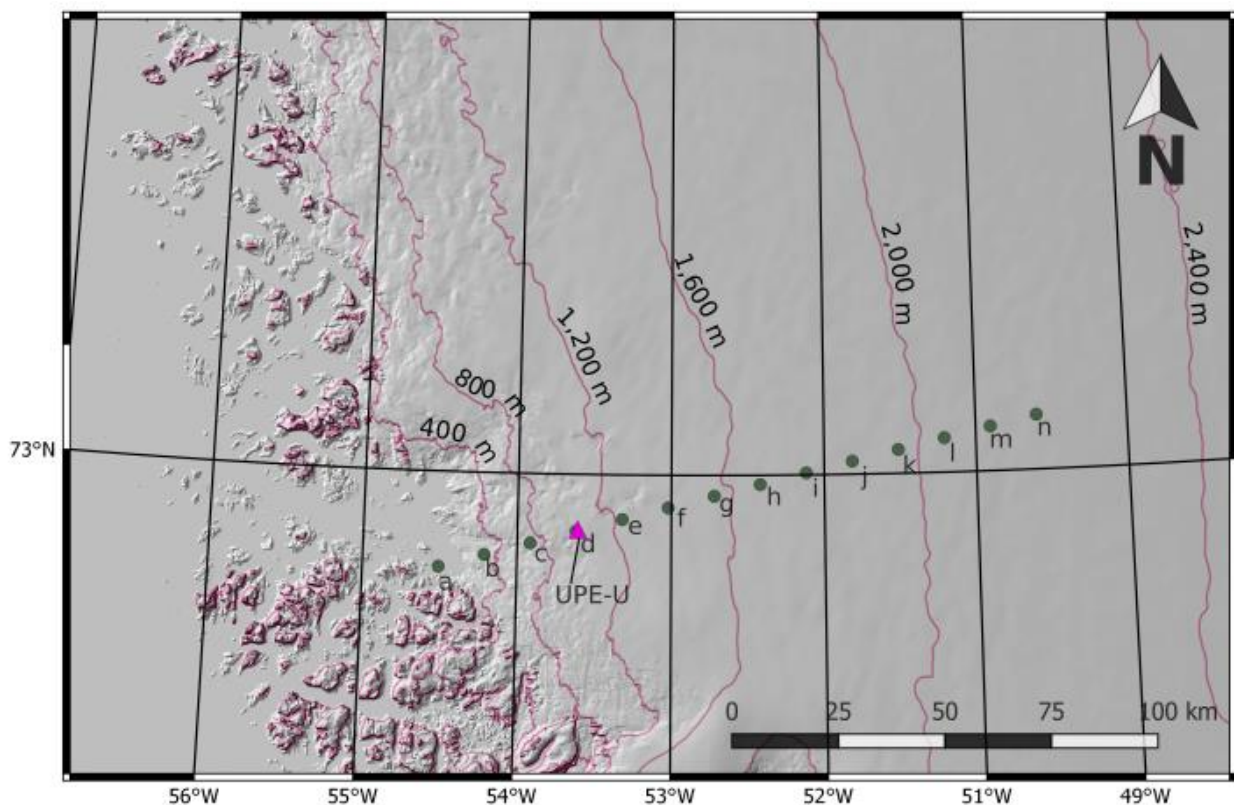


Figure 17: DEM of Upernavik Isstrøm Glacier with hill-shaded terrain using GIMP data (Howat et al., 2014), which was also used to determine the elevation of each RACMO grid cell. Green circles a-n are RACMO grid cells used for elevation-lake evolution testing and are labelled to allow easy reference in the results and discussion.

Pink triangle is the location of UPE-U weather station. See figure 14 for location within Greenland.

## Results

### Sensitivity testing

Figure 18 shows the model output when default parameters are used (appendix 3), to allow comparison with the model outputs during parameter testing. Labels of model output features are included to show the significance of each output value. Appendix 1 shows graphs of output sensitivity to input parameter variation. Figures 19, 20, and 21 are included below to highlight interesting features of model output with no hydrograph input, no precipitation input, and a large time step, respectively. Figure 22 shows an overall comparison between the sensitivity coefficients. Some sensitivity graphs show signs of instability or unrealistic behaviour as a result of the model being pushed into a scenario that was unaccounted for. If this behaviour proves problematic and is relevant to the main results, it is reviewed in the discussion. Overall, however, the model proves to be robust under a wide range of forcing. No graphs for changing break-up threshold parameters are included as no change was observed.

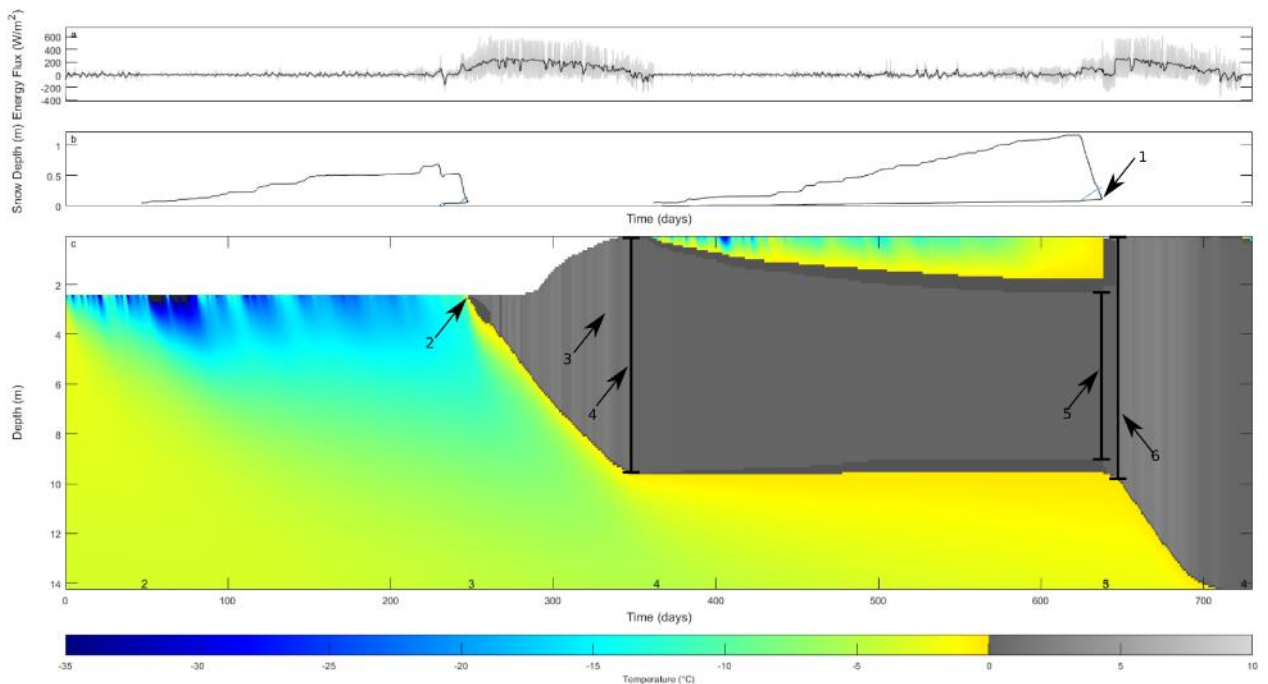


Figure 18: model output using default parameters with labels for output collection variables. 1: time of snow melt atop lid. 2: time of initial lake formation. 3: maximum average water column temperature during first melt season. 4: depth at end of first melt season. 5: depth under lid when snow melts, equates to shallowest

depth. 6: depth at start of second melt season after lid break-up. Top panel: total energy flux per time step (grey) and averaged over 24 hours (black). Middle panel: snow depth (uppermost blackline) accounting for density, water depth (blue) and depth of refrozen water (lowermost black line). Bottom panel: temperature profile for each time step down to the depth where grid cells of 1 m are used. Temperature scale beneath, coloured for ice and greyscale for water. White area in the top left is empty before the addition of water.

### Excluding a hydrograph input

Figure 19 shows the model output when incoming water from the surrounding catchment is excluded. As seen, the main influence is on lake depth before lid formation, with little effect on other model details.

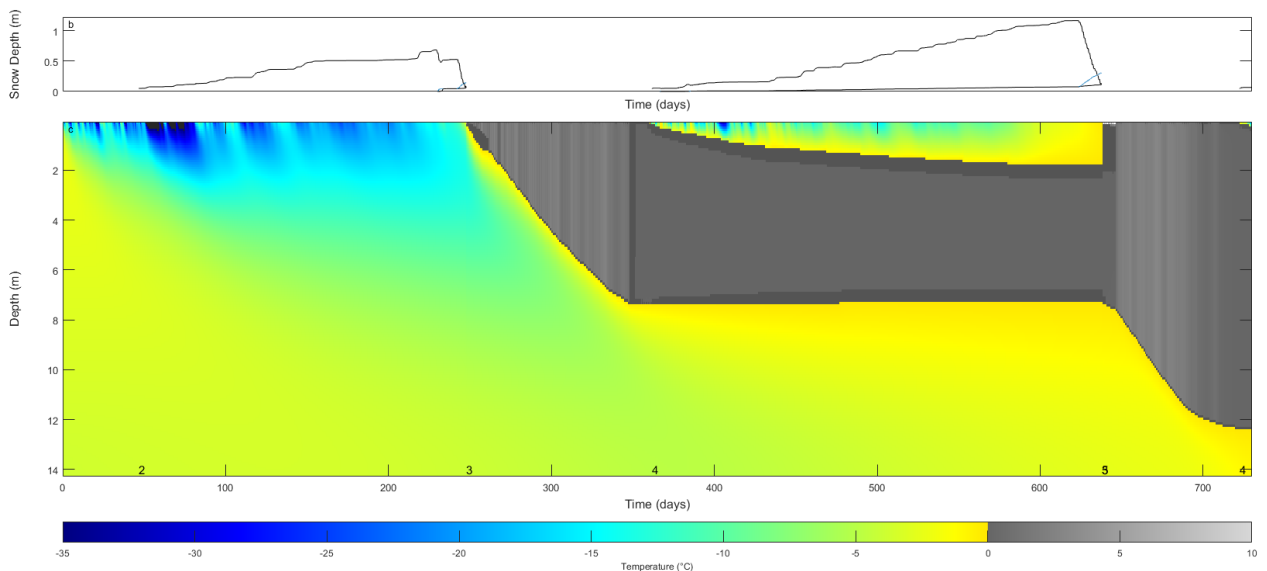


Figure 19: model output when run with no input hydrograph, as seen by absence of white area in upper-left corner and a shallower lake depth at the time of lid formation. Surface energy forcing omitted as graph is indiscernible to figure 18.

### Excluding precipitation

Figure 20 shows the effect of excluding precipitation to be substantial, particularly in relation to lid dynamics. Commentary on highlighted points in figure 20 is given in the discussion.

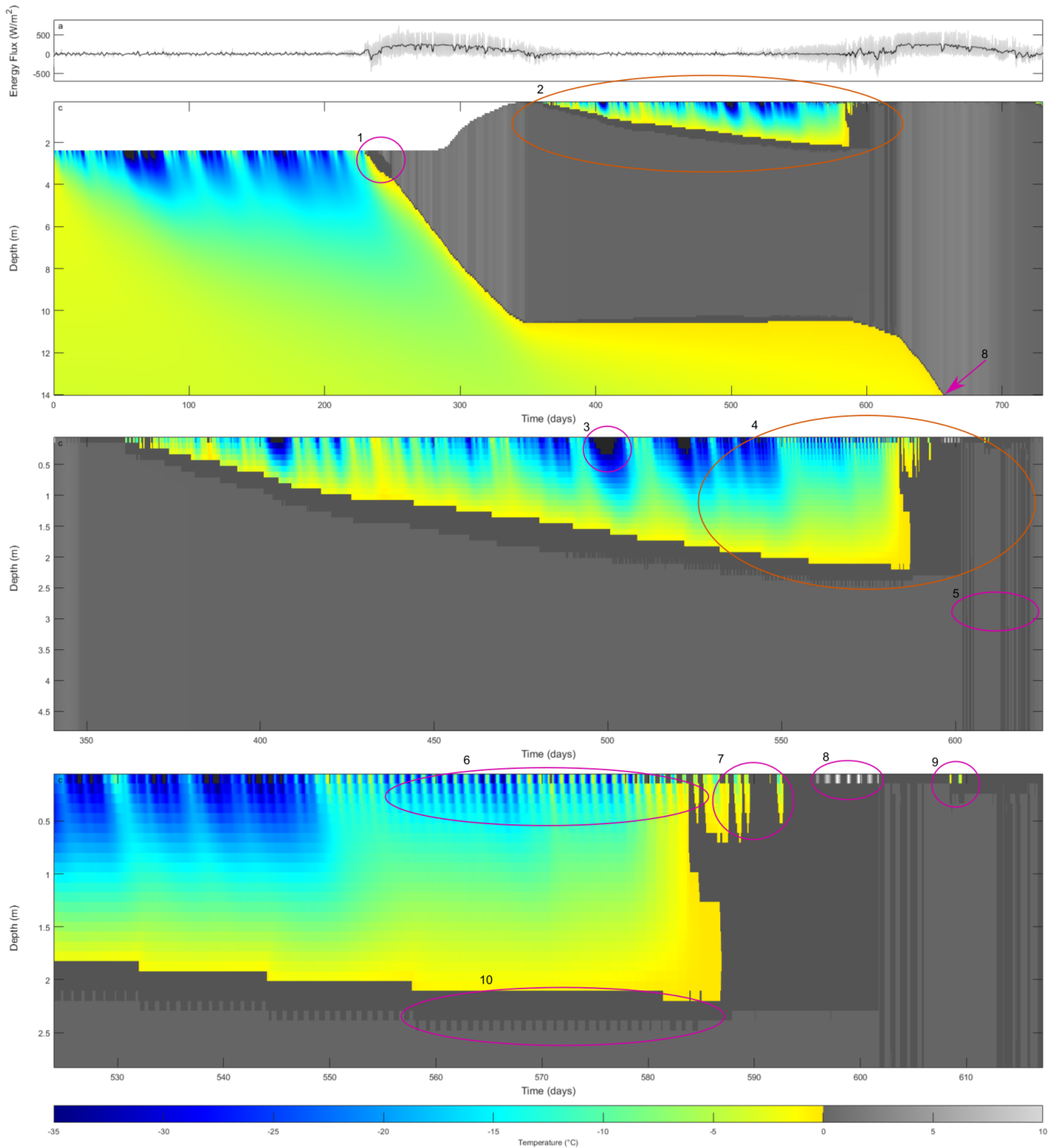


Figure 20: effect of removing snow layer entirely. Purple circles indicate point of interest, orange circle indicates area of close up. See table x in discussion section for more information.

### Time step

Increasing the time step to 2 hours results in a stable output, as seen in figure 21. However, some surface energy flux values appear to be transiently unrealistic.

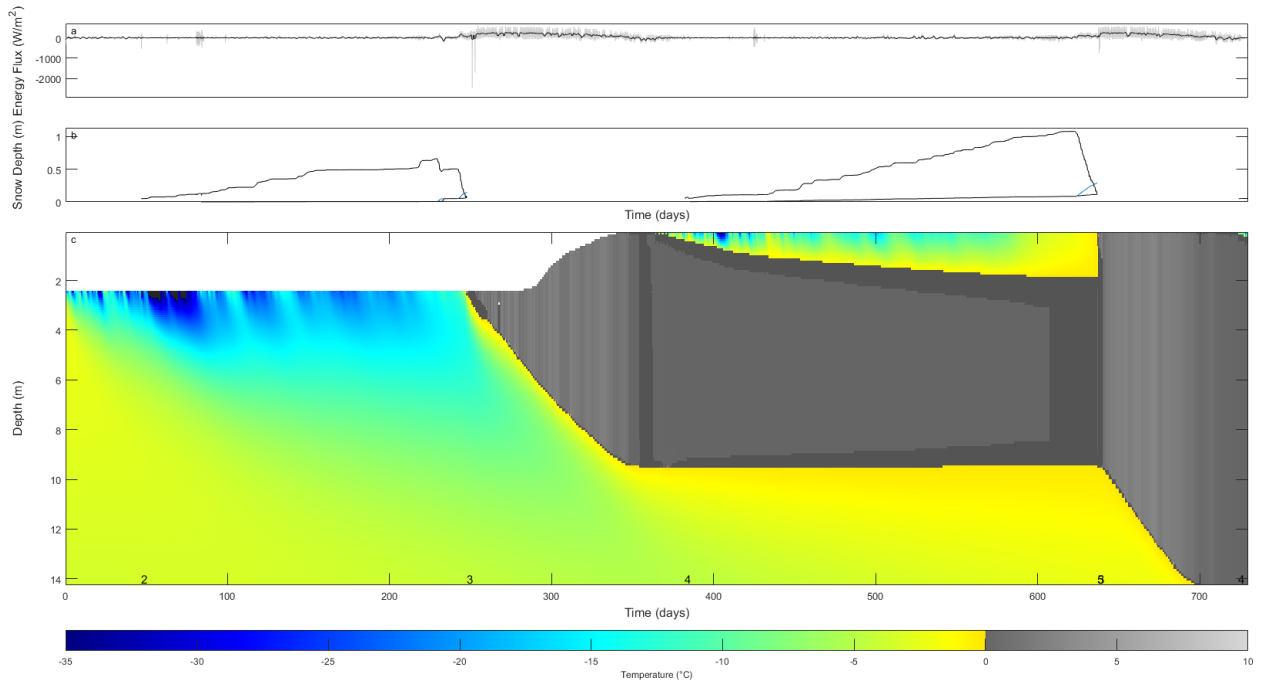


Figure 21: model output when a time step of 2 hours is used (default is 0.2 hours). Note quicker incursion of slush into the subsurface lake and the entire lake becoming slush before lid break-up.

### Overall comparison

Figure 22 shows that sensitivity is concentrated in the  $I_0$  term, hydrograph input, albedo calculation or instrumental uncertainty, and snow cover. Altering the  $I_0$  term causes the greatest response in lake dynamic outputs, with albedo multiplication causing the greatest variation across lake and ice-lid dynamics. Water temperature is seen to be highly insensitive to parameter variation and incoming water temperature, shortwave extinction of water, and snow compaction are seen to only mildly perturb model output.

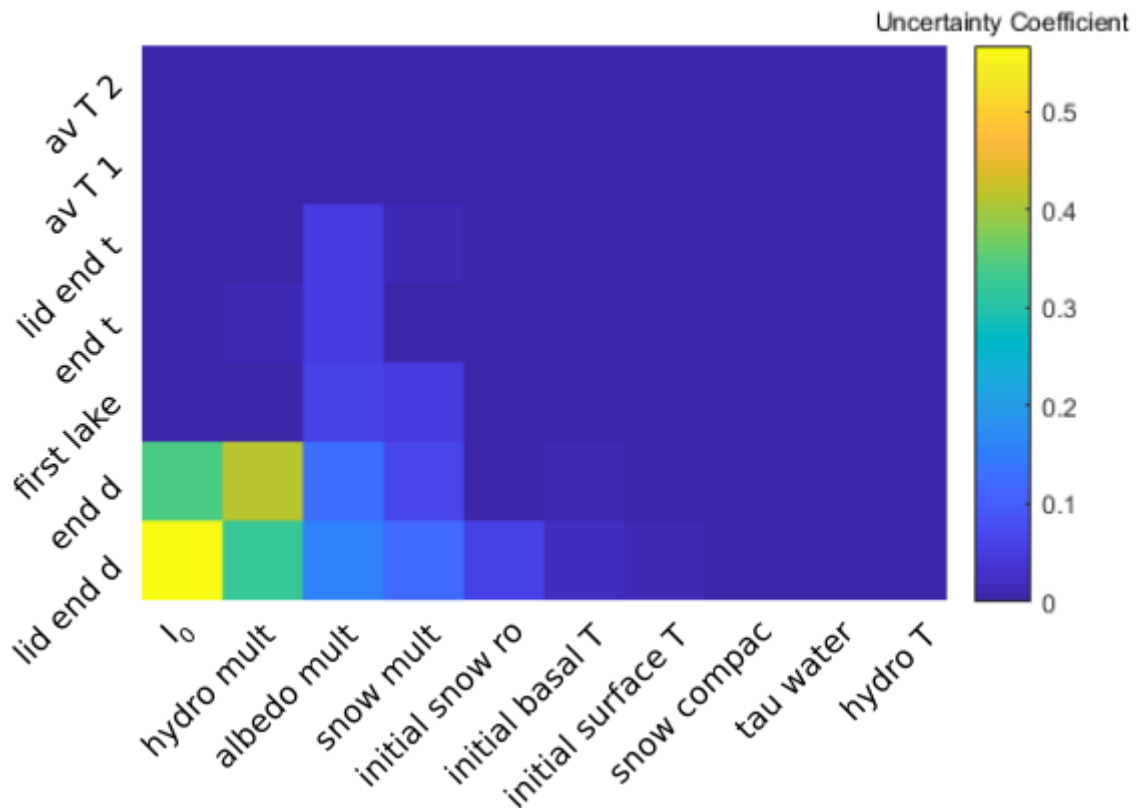


Figure 22: inter-comparison of uncertainty coefficients. Ordered by greatest sum uncertainty in columns and then rows. If abbreviated: hydro mult = hydrograph input multiplication factor; albedo mult = albedo multiplication factor; snow mult = precipitation input multiplication factor; initial snow  $\rho_0$  = initial snow density; snow compac = snow compaction timescale; tau water = shortwave extinction coefficient of water; av T 1/2 = maximum average water temperature in first and second melt seasons respectively; lid end t = when snow cover ends; end t = lid formation; end d = depth at time of lid formation; lid end d = lake depth at time of snowmelt. Lid break-up time and depth were excluded to simplify the diagram.

Model validation: comparison to Tedesco et al. (2012)

Sensitivity to calculation of incoming longwave radiation

The effect of calculating incoming longwave radiation following Benedek (2014), rather than using PROMICE UPE-U AWS data, is shown in figure 23 and the model output is shown in figure 24. The longwave source has relatively little effect on the time of first lake formation, the time of lid formation, or the time of snow melt (0.8, 1.5, and 1.2 days respectively) but causes a sizeable 0.45 decrease in end-of-melt-season lake depth.

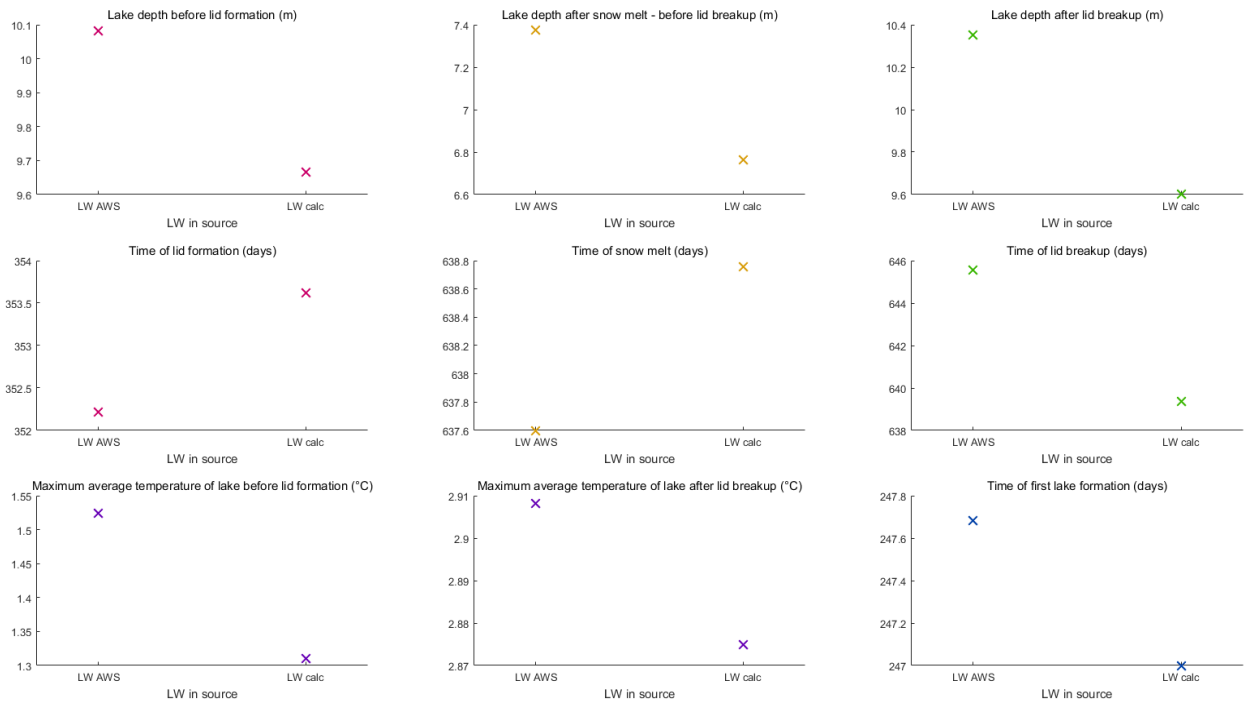


Figure 23: effect of using incoming longwave radiation from LW AWS data or from calculations following Benedek (2014) (LW calc).

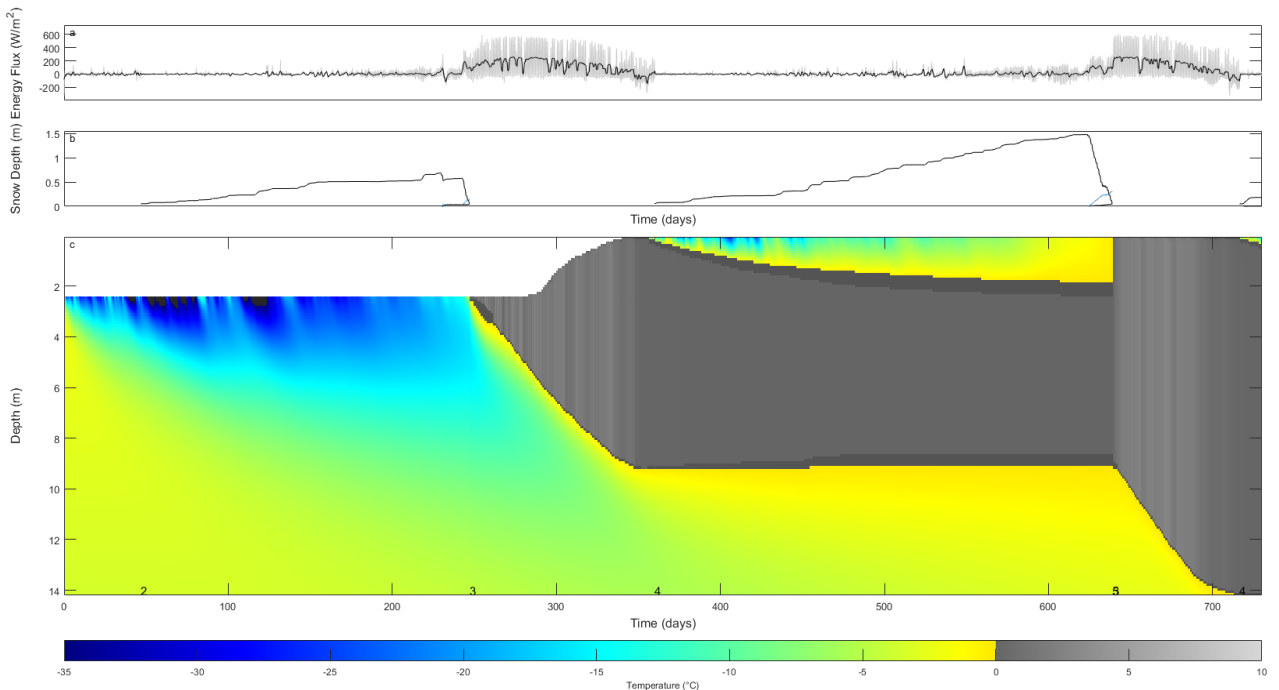


Figure 24: model output when incoming longwave radiation is calculated following Benedek (2014) and all other parameters are held the same.

## Validation results

Figure 25 shows the model output when the forcing data for Lake Ponting is used. Figure 26 shows extremely good agreement between model output and observations with a difference across the common observation period of 5 days of less than 0.1m. The sensitivity of these results to the  $I_0$  term is large but the relationship is still very good and clear if the default value of 0.6 is used (figure 27).

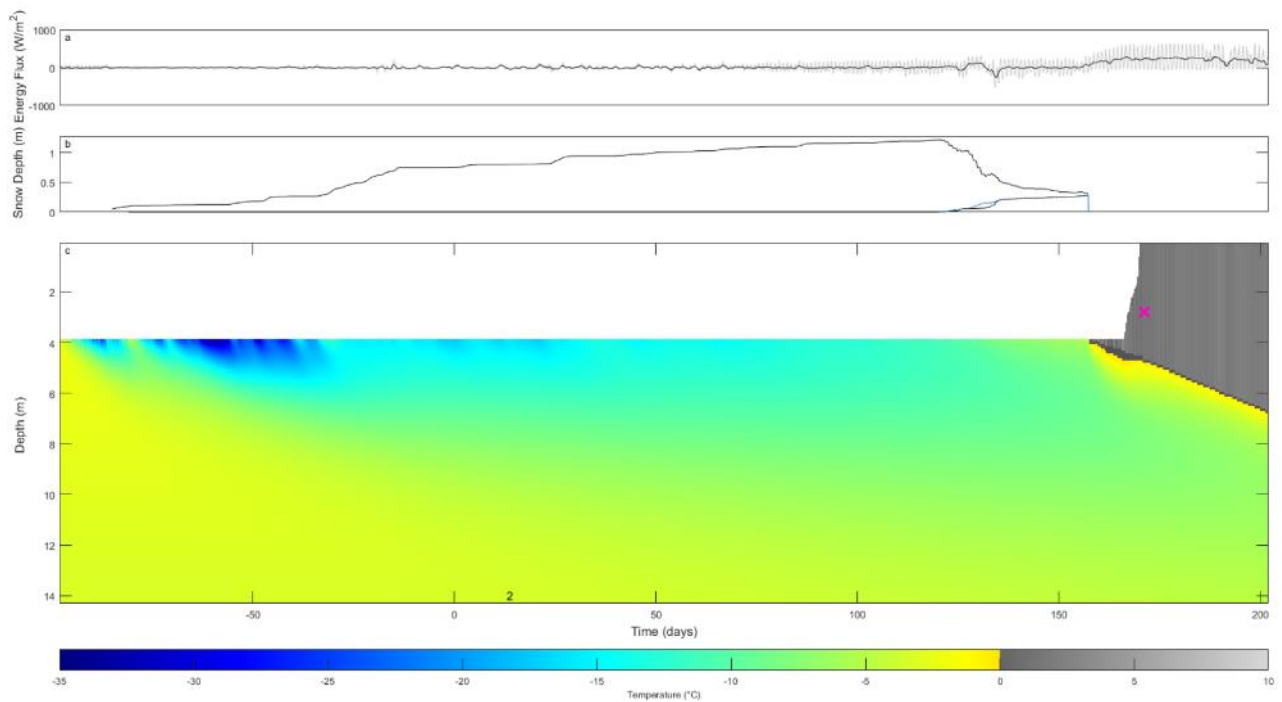


Figure 25: model output when forced using data from Benedek (2014) for Lake Ponting for 26th July 2010 to 25th July 2011. Time in days is the time before or after the 1st of January 2011. The purple cross indicates the time at which the lake was observed to drain by Tedesco et al. (2012).

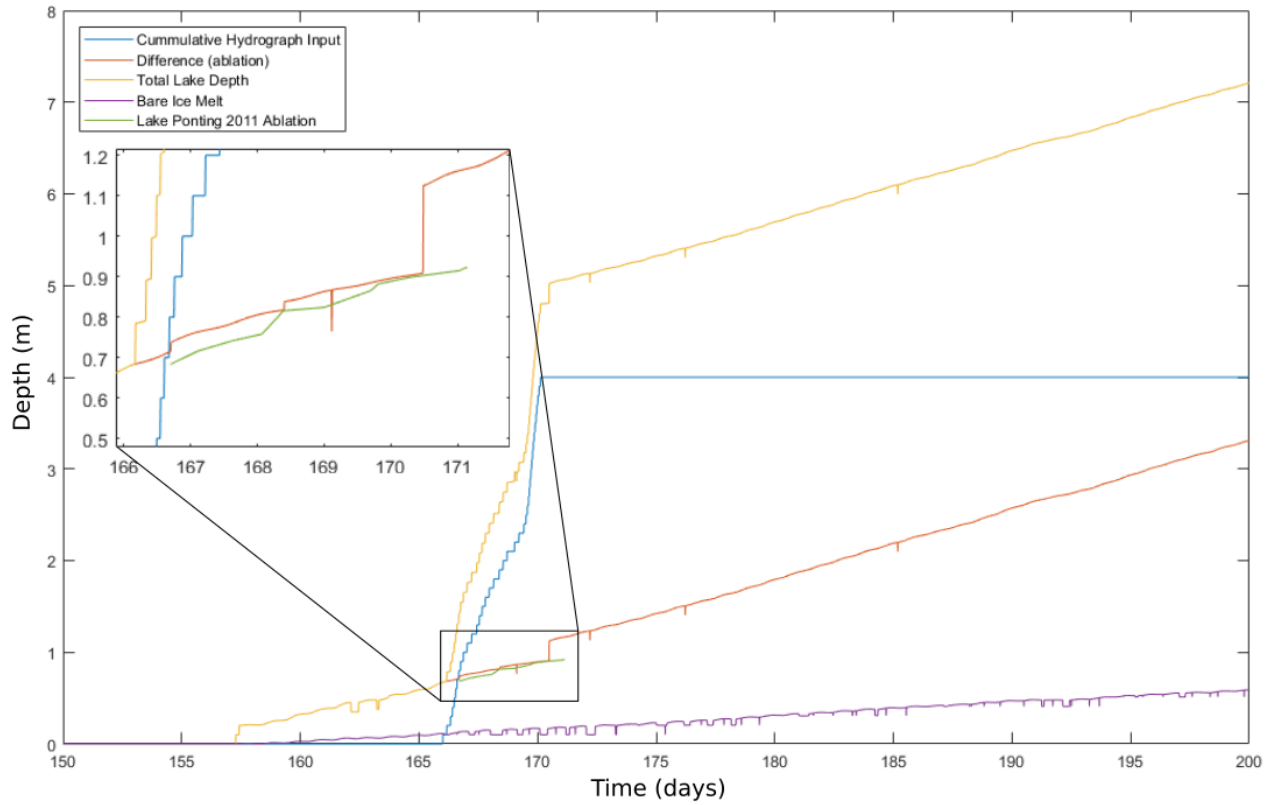


Figure 26: depth from 150 – 200 days from 1st January 2011 to compare modelled and observed lake ablation with an  $l_0$  value of 0.35.

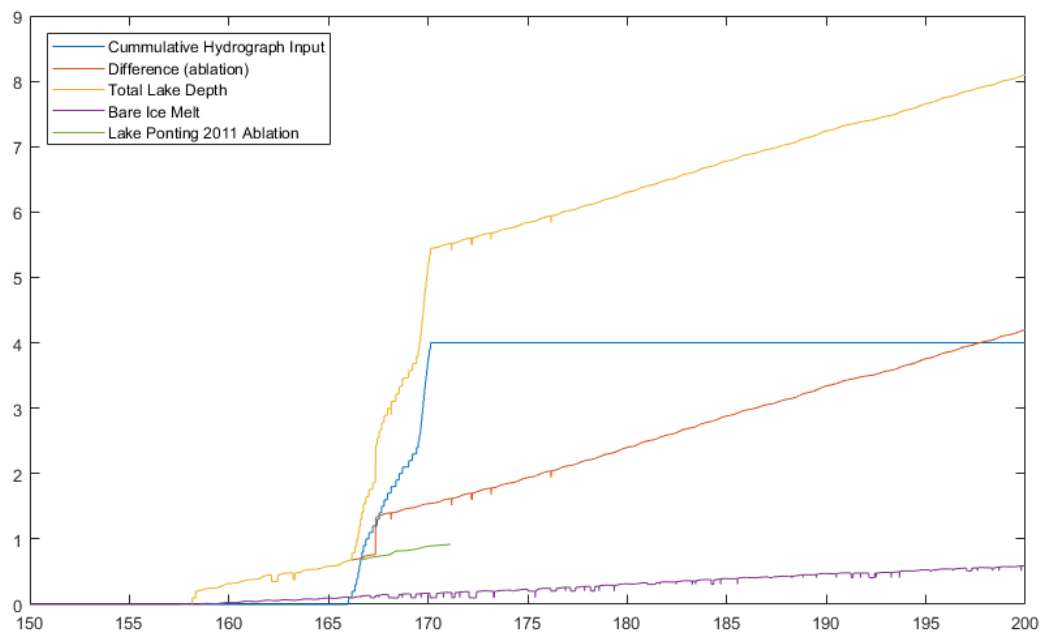


Figure 27: as figure 26 but using an  $l_0$  value of 0.60. The large step increase in basal melt is a result of 2 slush cells becoming water cells at the same time step.

Model inter-comparison with Buzzard et al. (2018)

Figure 28 shows the output when the Benedek (2014) forcing data is used for the model of Buzzard et al. (2018); an overestimation of lake duration is observed.

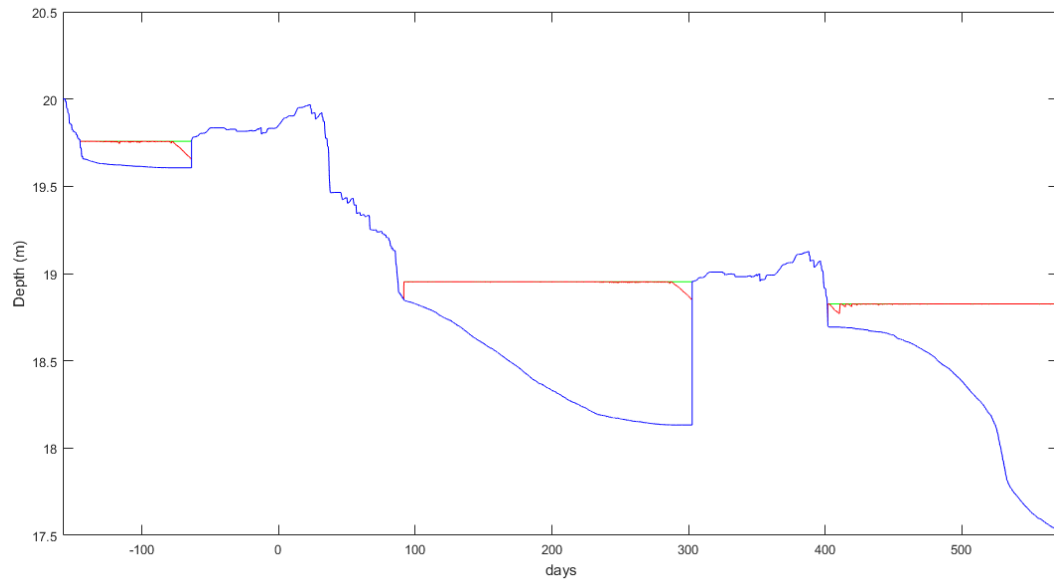


Figure 28: results using the model of Buzzard et al. (2018) with the forcing data for Lake Ponting from Benedek (2014). x-axis is days from 26<sup>th</sup> July 2010. After 365 days, the weather loops back to begin again from 26<sup>th</sup> July 2010. Blue line is the height of the ice/firn surface above the base of the domain, red line is height of the lake above the base of the domain, green line is the height of the lid above the base of the domain.

### Endless winter

Figure 29 shows the model output when the model is held in a state of permanent winter from 5<sup>th</sup> April 2010, with forcing data from 02:00, 1<sup>st</sup> February 2010. Cells in the middle of the lake appear as slush in figure 30 as the resolution of the temperature scale is not sufficiently high to detect water temperatures within  $10^{-12}$  of 0 °C. The water content of each cell can be seen in figure 30. The rate of freezing from the top of the lake downwards is  $0.91 \text{ m yr}^{-1}$ , if assumed to be linear. Figure 31 shows the effect if snow is excluded from the second lid, with an exponential decrease in thickening rate.

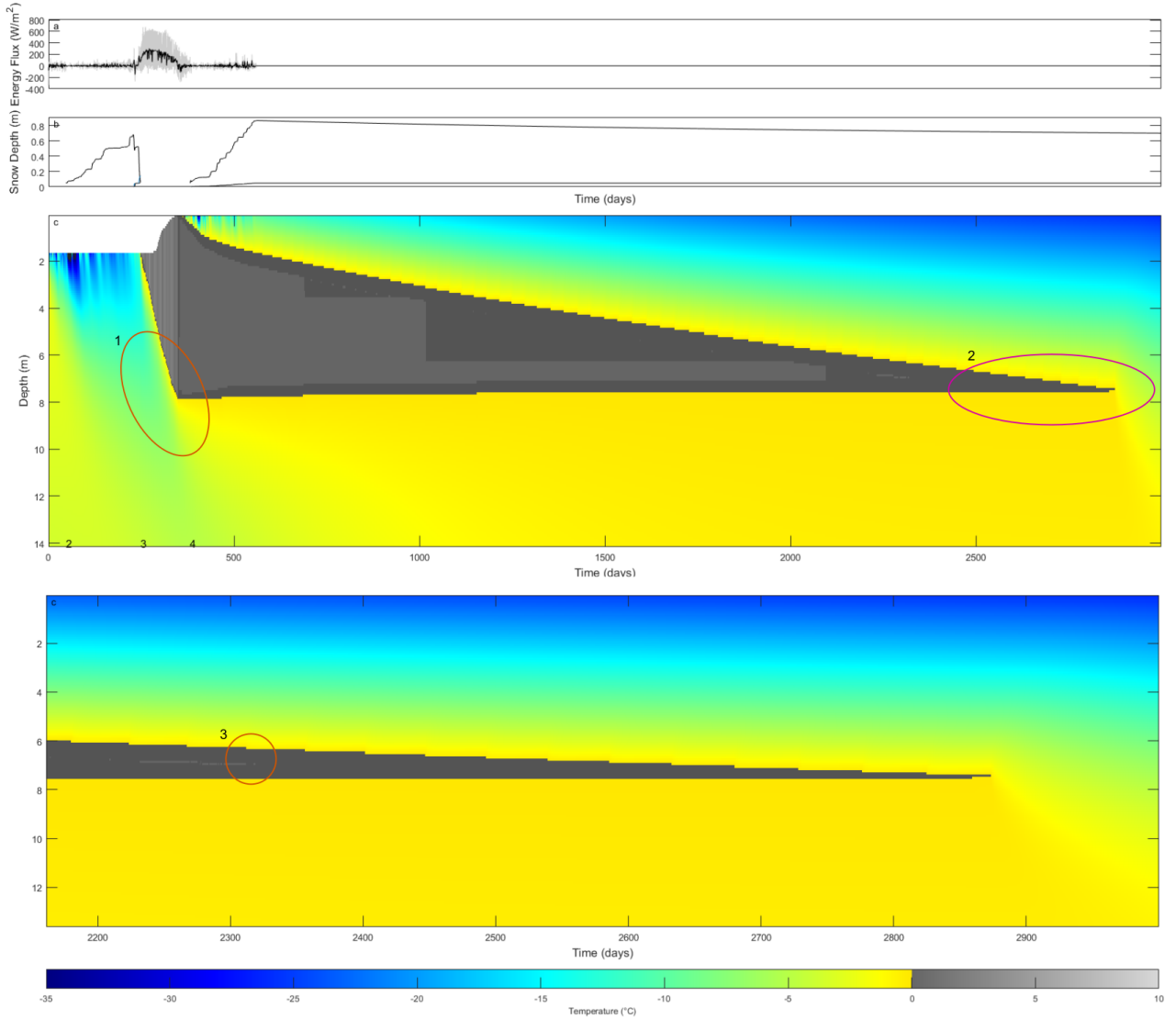


Figure 29: using 02:00, 1<sup>st</sup> February from 5<sup>th</sup> April. Descriptions of highlighted areas: 1, colder ice at 8 m is brought up to  $\sim -1.5$   $^{\circ}C$  after lake is above it. The ice underneath the lake gradually warms to  $\sim -0.5$   $^{\circ}C$  degrees up until the lake vanishes entirely. 2, close-up of bottom panel, it is possible to see cold ice immediately penetrating deeper into the column as soon as lake vanishes entirely.

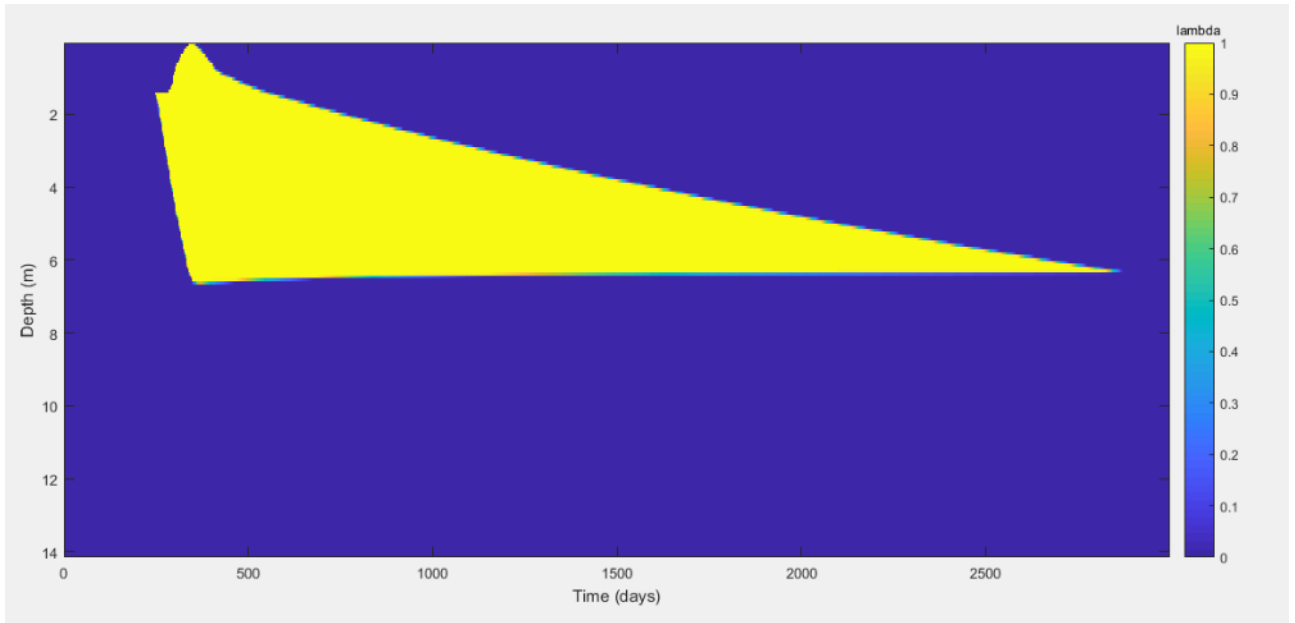


Figure 30:  $\lambda$  values of the cells in figure 29. All yellow cells show a value of exactly 1, meaning they are water cells, and not slush cells.

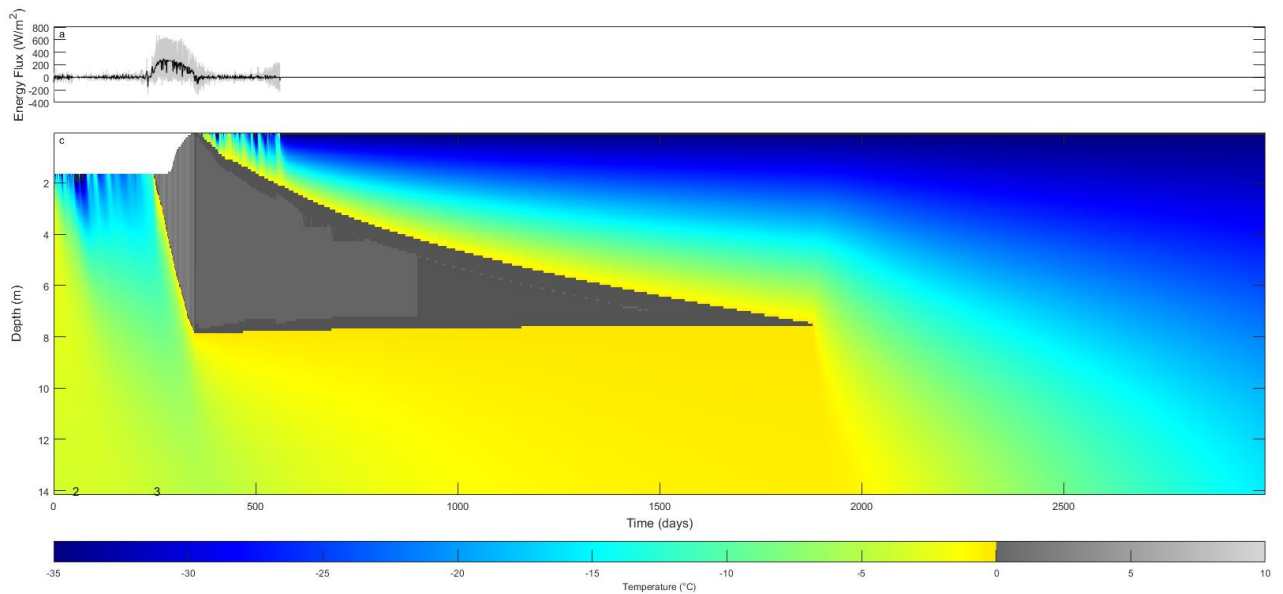


Figure 31: same setup as figure 29 but snow is excluded from the lid. Note the rapid diffusion of heat away from ice underlying the lake as soon as the lake disappears entirely.

Application: elevation-lake evolution relationship

RACMO-UPE-U comparison

Figure 32 shows a comparison of model output when UPE-U AWS or RAMCMO data are used. Output variable comparison is given in table 3, showing RACMO data cause earlier lake formation and a deeper lake before lid formation.

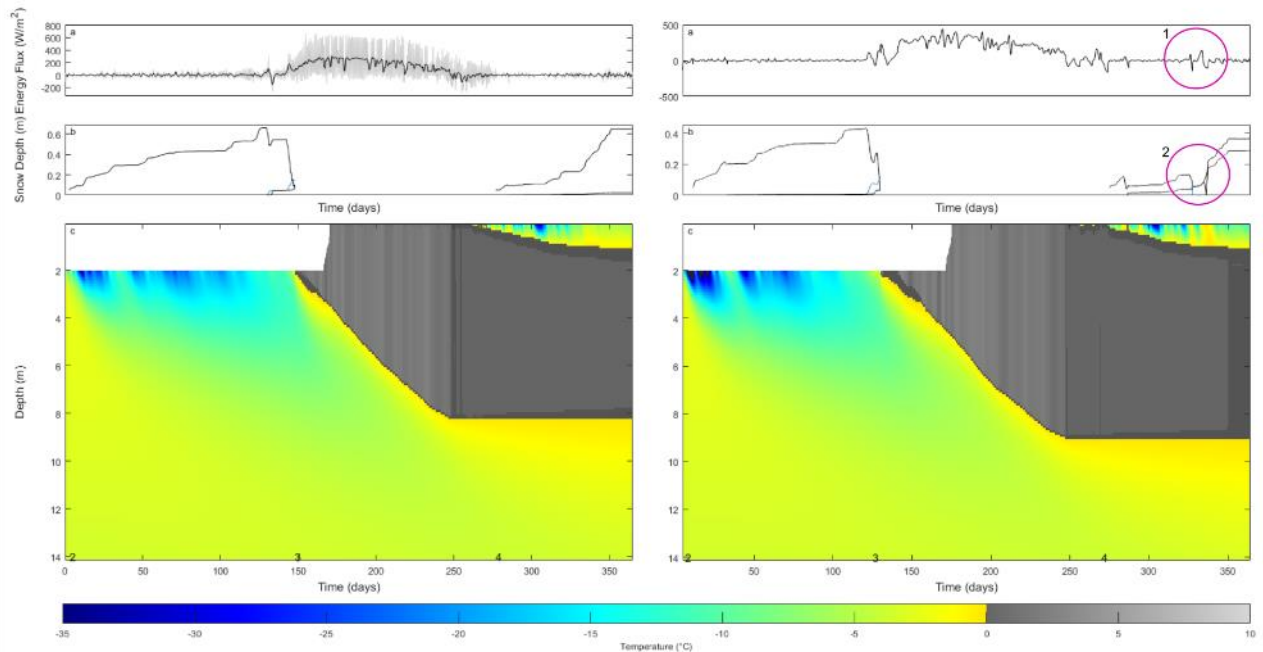


Figure 32: difference between PROMICE UPE-U AWS data (left) and RACMO data for 11km grid at 72.89°N, 53.53°E. Circles 1 and 2 covered in discussion.

	UPE-U	RACMO
<b>Lake formation day</b>	151.5	141.3
<b>Lid formation day</b>	271.9	273.8
<b>Lake depth</b>	8.09	8.92

Table 3, comparison in output between UPE-U and RACMO data.

### Elevation-lake evolution relationship results

Figures 33 and 34 show the model output for selected RACMO grid cells, with figure 35 showing the observed output variable trends with increasing elevation. Figure 36 shows the output for selected RACMO grid cells when precipitation is excluded, with trends for increasing elevation seen in figure 37. If 5 m of hydrograph input is included at RACMO grid

cell n (at 2,208 m a.sl., the highest elevation used), the lake does not freeze entirely and the maximum lid thickness (when precipitation is excluded) is 2.71 m.

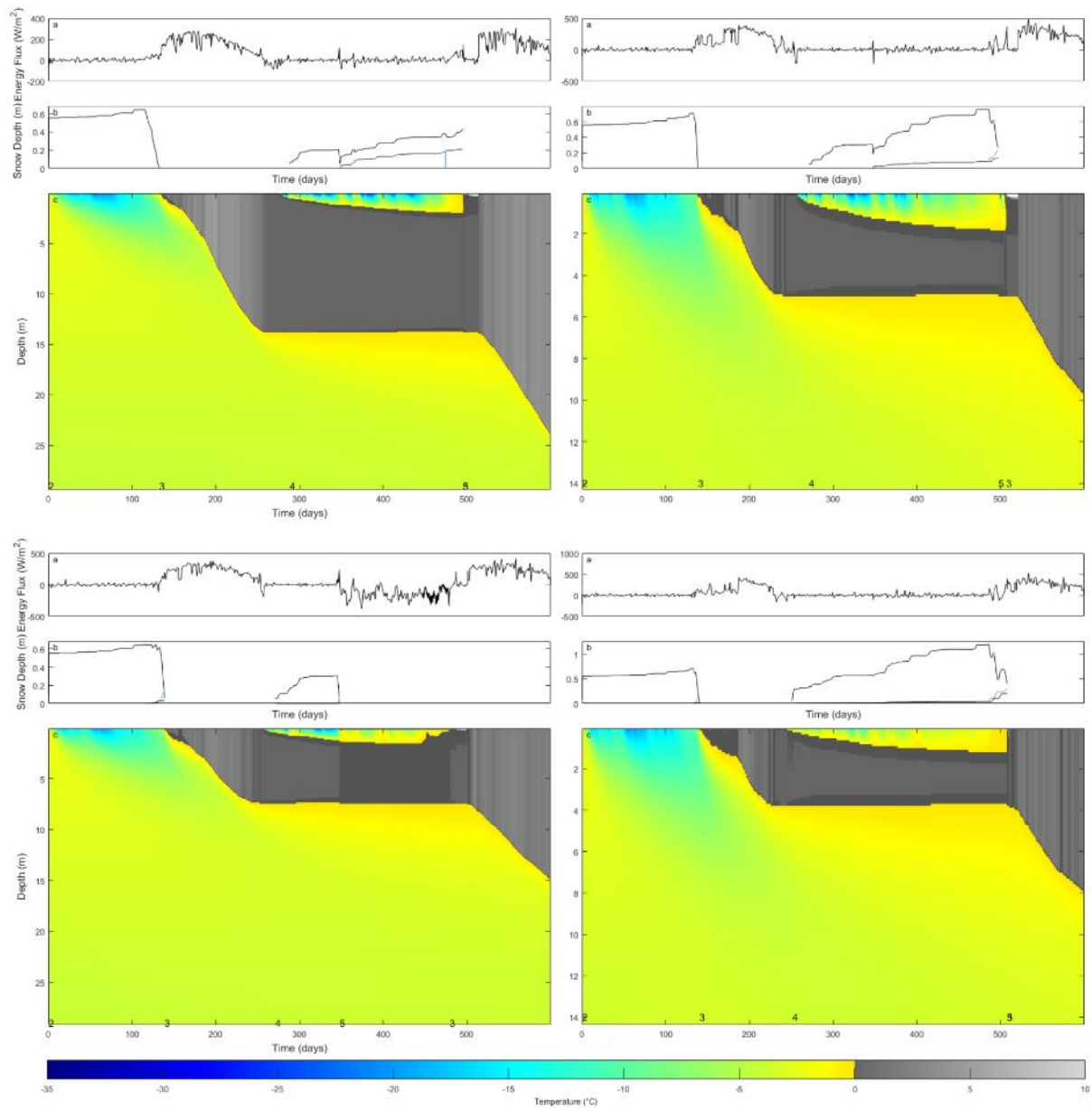


Figure 33: elevation-lake evolution relationship. Left to right and top to bottom: point a, 130 m elevation, note 30 m y axis; point c, 752 m elevation; point e, 1255 m elevation; point g, 1581 m elevation

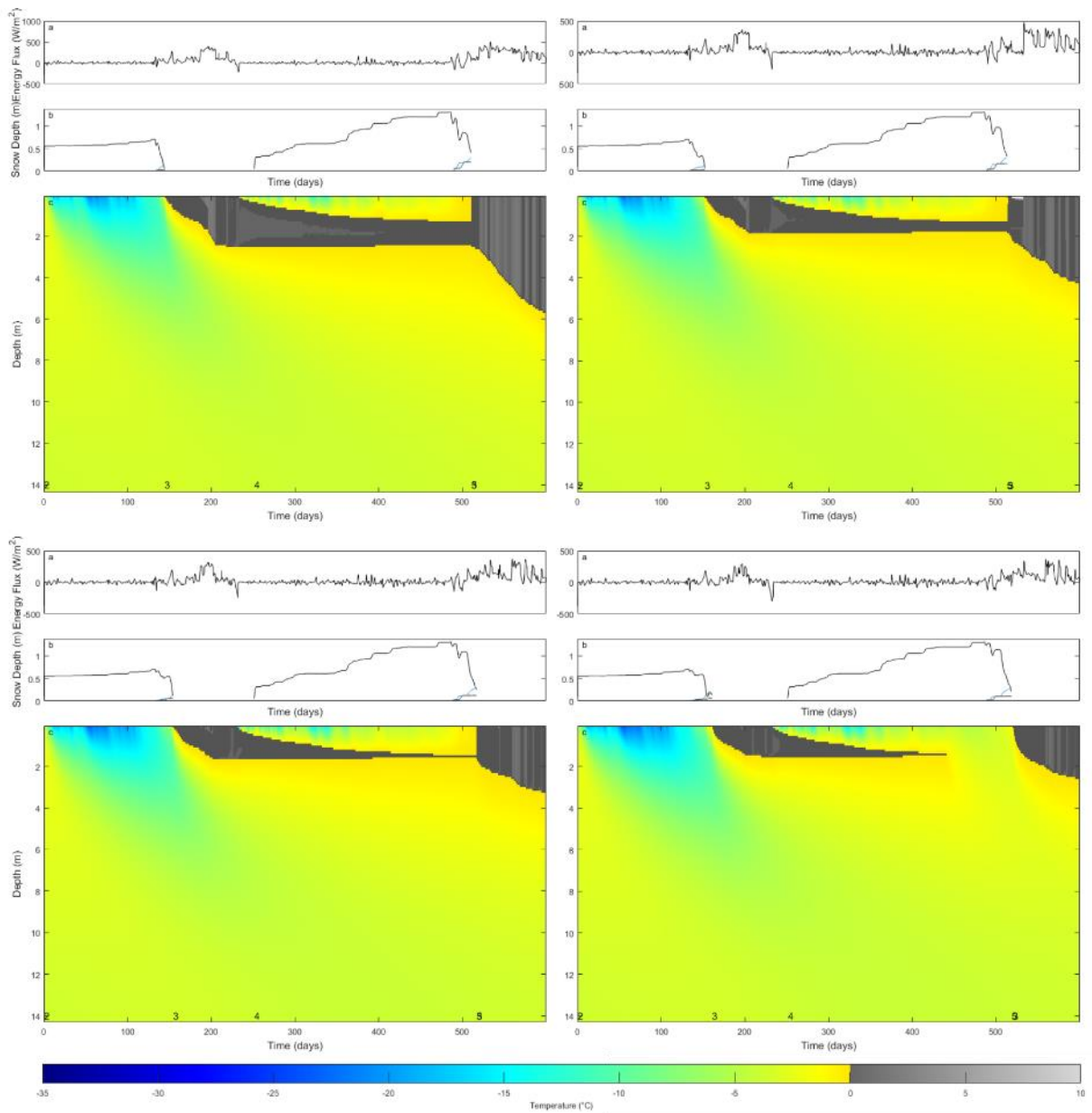


Figure 34: elevation-lake evolution relationship. Left to right and top to bottom: point i, 1791 m elevation; point k, 1972 m elevation; point m, 2137 m elevation; point n, 2208 m elevation

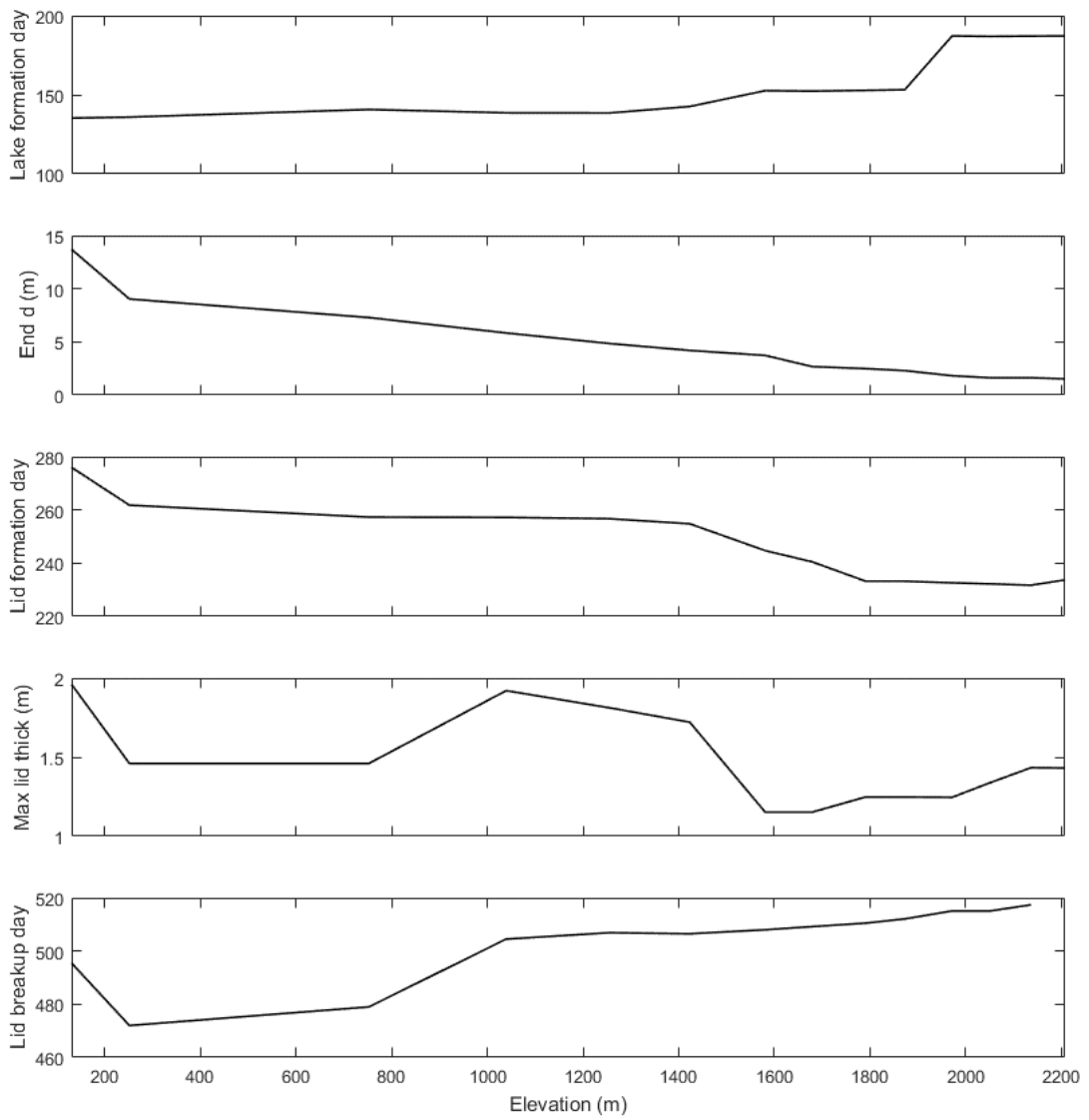


Figure 35: model output-elevation relationships. If abbreviated: end d, depth at end of first melt season; max lid thick, the maximum observed thickness of the ice-lid.

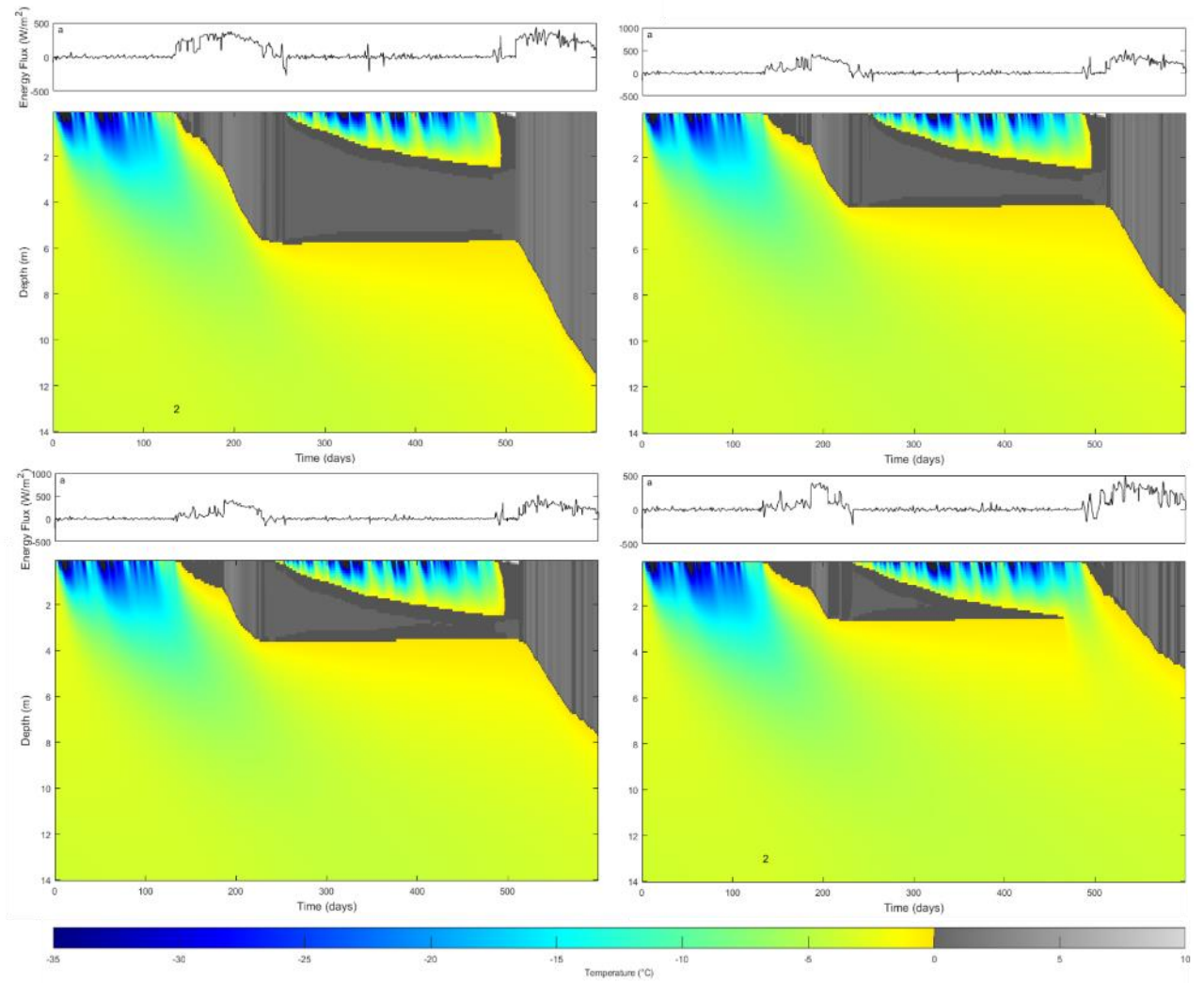


Figure 36: elevation-lake evolution relationship with no snow. Left to right and top to bottom: point d, 1039 m elevation; point f, 1423 m elevation; point g, 1581 m elevation; point i, 1791 m elevation

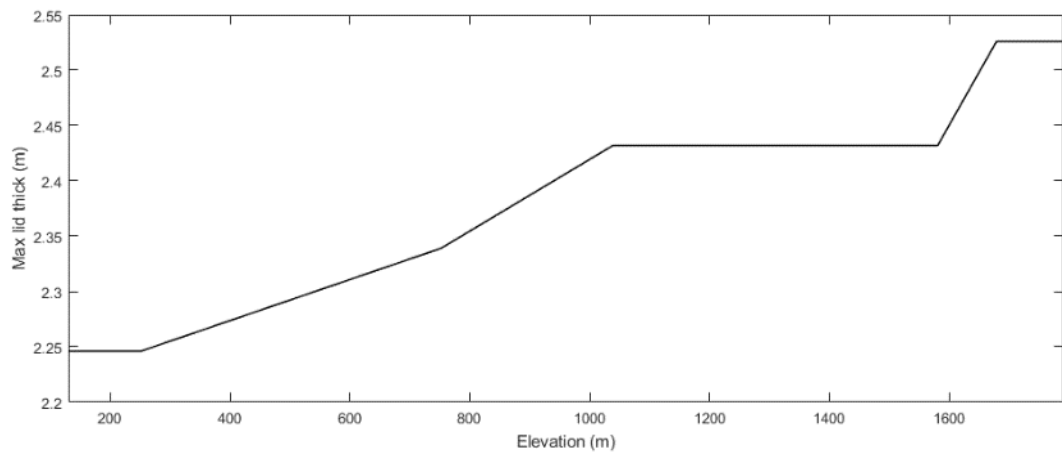


Figure 37: lid thickness with elevation.

## Model performance

For the 365-day run, to compare model results to the Tedesco et al. (2012) field data, using a 3.2GHz Intel Core i5-6500 processor, the initial run including loading NetCDF files takes 30 seconds and subsequent runs take 17 seconds. This is using 160 vertical grid cells and a timestep of 12 minutes. The three largest time expenditures are 29% for the heat diffusion equation, 15% for indexing the lake location, and 9% for convection. By comparison, the model of Buzzard et al. (2018) takes 46 minutes using the same computer for a 365-day period using 200 vertical grid cells and a timestep of 1 hour, and requires the same amount of time again for spin-up.

## Discussion

### Broad model behaviour

Figure 38 shows the output when the model is run using PROMICE UPE-U weather data for 800 days from 1<sup>st</sup> September 2009, with the hydrograph input of lake 200 from Arnold et al. (2014). Figure 39 shows close-ups of aspects of model behaviour and figure 40 shows snow-layer behaviour. Many qualitative aspects of lake evolution can be observed from this figure before it is applied quantitatively to elevation-evolution relationships. Where discussion points from the figures are brief, they are tabulated in table 4 to aid navigation.

It is important to note the year-on-year increase in lake depth. The first lake forms over ice that has been cooled significantly over-winter from the initial temperature of -2 °C to a minimum of less than -35 °C, although by the time snow melt has occurred, the upper 2 m of ice are closer to -15 °C with the rest of the profile at approximately -5 °C. By comparison, the second lake forms from a temperate 2 m lid and 7 m of water with > -2.5 °C ice below this. Even if the lake vanishes entirely, the remaining ice is far warmer ice than if no lake had been present. This means that lake depth can be expected to deepen year-on-year due to the warming effect of previous lakes, and is hampered only by the advection of cooler, thicker ice into the depression. The impact on downstream morphology of the advecting, deepened lake basin warrants further investigation, but the observation that lakes form in the same locations

year-on-year (Echelmeyer, 1991; Lampkin and Vanderberg 2011) shows it is not sufficient to outpace the influence of bed topography. It is possible that the advecting basin generates a preferential flow pathway for lake overtopping or attenuates the profile of the following year's lake.

In figure 38 and in the sensitivity testing, the maximum average lake water temperature does not exceed 4 °C, other than for shallow depths when lid-break-up occurs and turbulent heat flux is unaccounted for. This means that dense, cold water is always at the surface of the lake, encouraging ice-lid formation. It may also imply that the rate of lake growth is partly controlled by lake temperature, with high lake temperatures prompting basal melting which in turn lower the lake temperature. The last section of the ice lid to become slush is the centre (Figure 39: a and b), as expected with both a positive surface energy flux at the start of the melt season, and a negative temperature gradient resulting from the ice-water interface acting as a 0 °C boundary. Following this, slush cells progressively become entirely water from the top downwards. The covered lake once more begins to expand downwards, though at a rate far lower than the rate when no lid is present. Here, the impacts of homogenising the vertical enthalpy profile on the lid break-up threshold are clear, with a brief, quarter-day period where the entire profile is comprised of slush cells before the entire profile becomes fully liquid again. This section of the model could be improved to allow dense surface melt to seep beneath a predominately slush lid. However, it is likely that this would not significantly change the date of lid break-up, especially as the lid break-up date proves insensitive when altering lid break-up parameters (see sensitivity discussion). There is very little lag time after lid break-up before the lake temperature rises several degrees, showing the large impact of the lake's exposure to surface energy flux and again supporting a temperature-controlled basal melt rate.

Number	Comments
Fig 38, 1	There is a clear leap in surface energy flux as the lake becomes established due to the associated decrease in albedo. The sinusoidal increase and decrease of surface energy flux reflects the diurnal pattern of the incoming shortwave radiation. The noticeable negative surface energy flux at the end

	of each of these periods reflects the release of latent heat as a phase transition from water to ice occurs.
Fig 38, 2	Behaviour of the snow layer from the end of its accumulation phase until full snowmelt. Described in greater detail in figure 39.
Fig 38, 3	A short-lived cold section just after lid formation that is noticeably less cold or continuous than the cold section seen before the presence of a lake. This is the result of a 0 °C constant boundary at very shallow depth due to the water-ice transition, which retards the occurrence of cold spots as any heat loss is quickly shifted into latent heat when water turns to slush or ice.
Fig 38, 4	Lid break-up, seen in greater detail in figure 39 a.
Fig 38, 5	Lid formation, seen in greater detail in figure 39 d and e.
Fig 38, 6	Gradual freeze-up of lake from its base at a rate much lower than freeze-down from lid. Also note increase in temperature of basal ice below the lake throughout the winter due to the 0 °C lake-bottom boundary.
Fig 38, 7	Basal melt during the melt season mirrors the neat progression observed in Benedek (2014) with only one slush cell being present at once. This is most likely a result of a greater temperature gradient when the lake is warm and melting its base than when the lid has formed and a thicker slush zone is observed during lake freeze-up. The rate of melt seen here is greater than that for the first melt season, possibly a result of warmer underlying ice. This is presented as a close-up in figure 39, f.
Fig 39, c	A slush buffer zone between lake water and ice. Benedek (2014) takes the presence of multiple slush cells as a sign that the model does not replicate heat transfer at a sufficiently fast rate. Here, however, it likely reflects the extremely small temperature gradient between the extremely cold water and relatively warm ice.
Fig 39, d	Diurnal temperature variations within ice (indicated by the presence of a slush cell) forming on repeated nights before a constant slush layer occurs at 710 days. The temperature profile of the lake can also be seen here, with temperature decreasing towards the surface as expected. Figure 39e shows the clear transition from basal ice to water when a lid begins to form. Once the lid forms, the temperature drops markedly to within a fraction of 0 °C and continues to approach freezing point, a trend that continues until lid break-up. Lid growth is initially rapid, with a 0.7 m lid forming within 18 days before a far slower rate of development. Close-up in figure 39, f.
Fig 39, e	Lid formation at 727 days with large diurnal temperature variation in the top ice cell following formation, reflecting the lack of overlying insulating snow. Figure 40: 3 highlights the temporary formation of a 10 cm ice lid before a further 4.5 days of lake surface slush.

Fig 39, f	Neatly progressing basal lake melt, with a $\sim 2$ °C temperature difference over 10 cm.
Fig 40, 1	Normal snow addition.
Fig 40, 2	$\sim 20$ cm of snow melt and corresponding increase in water content. The water then freezes, leading to the formation of the snow-ice layer that displaces the overlying snow (along with an increase from additional snowfall).
Fig 40, 3	Diurnal fluctuation in melt rate with some overnight refreezing and snow-ice layer growth. All snow then melts leaving a depth of ice and water to be carried forward to lake initialisation.

Table 4, discussion of highlighted aspects of figures 38, 39, and 40.

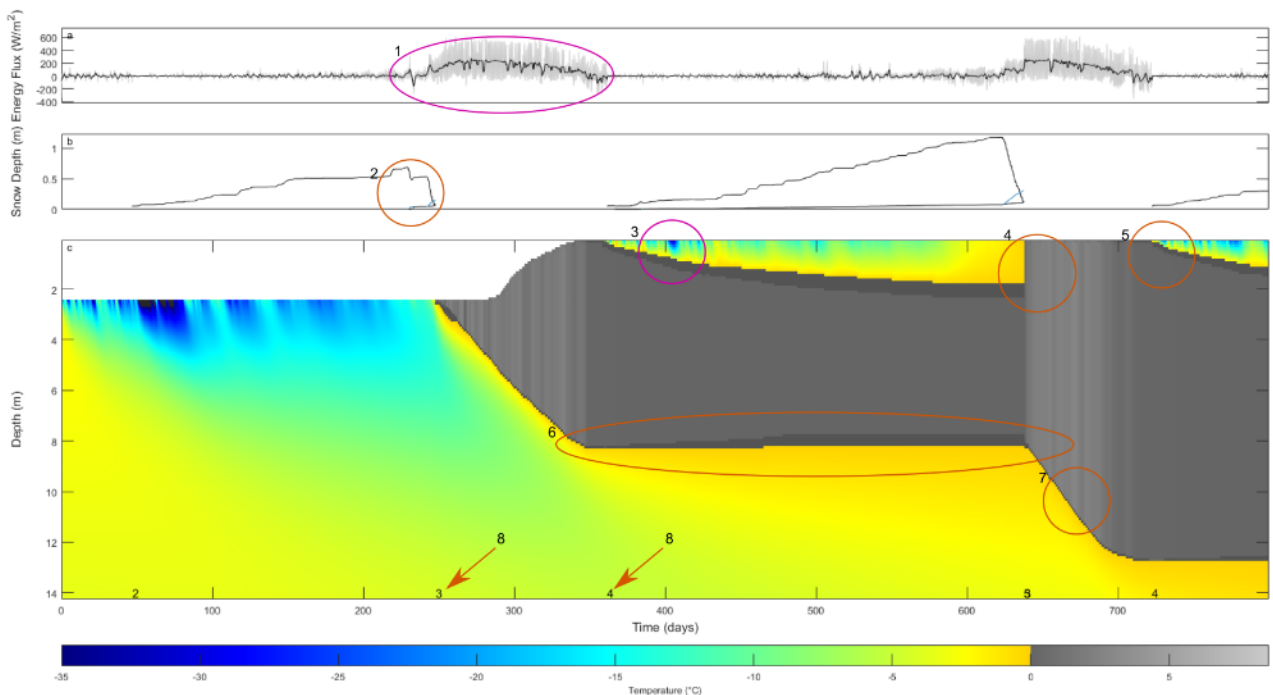


Figure 38: example of the main figure produced by the model. See text for description of circled and arrowed features. Run for 800 days from 9<sup>th</sup> September using AWS data from PROMICE UPE-U and hydrograph input from lake 200 of Arnold (2014). Precipitation from RACMO re-analysis.

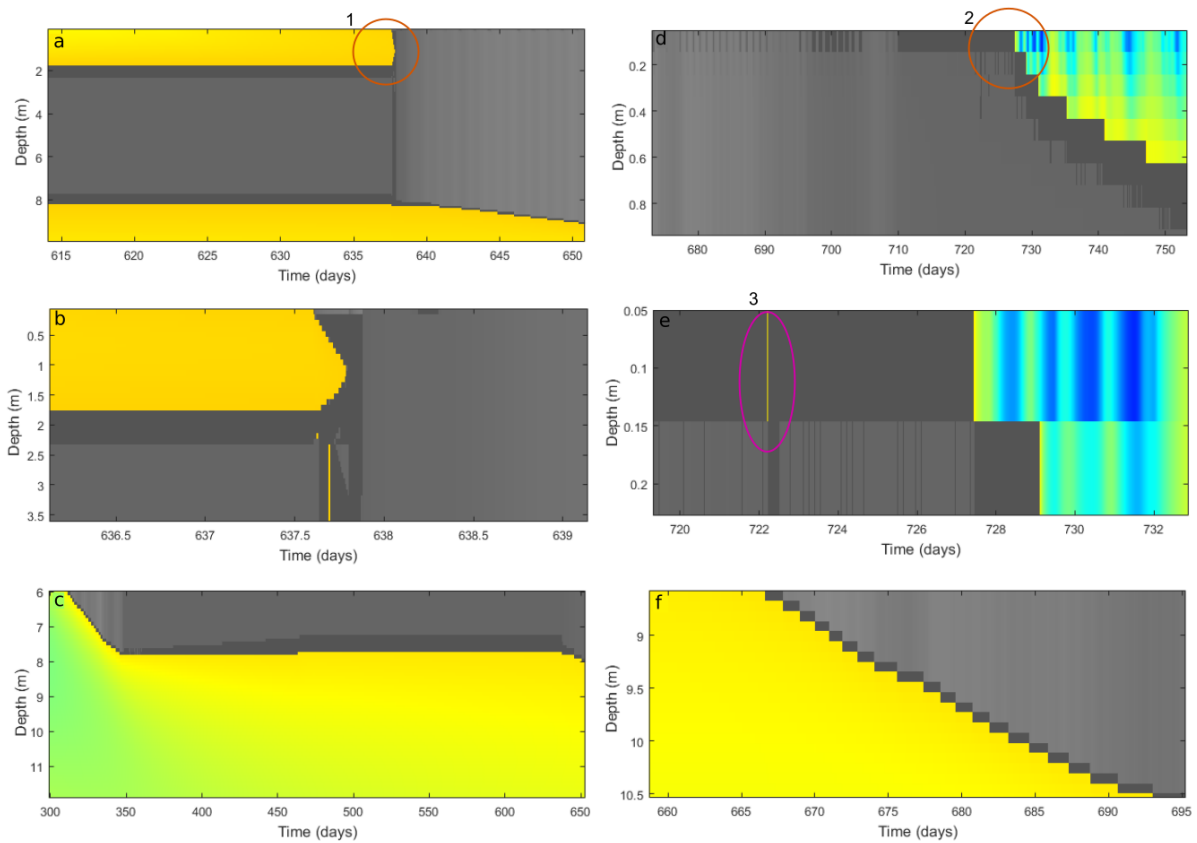


Figure 39: close-ups of areas highlighted in figure 38. Highlighted areas are discussed in the text and table x.

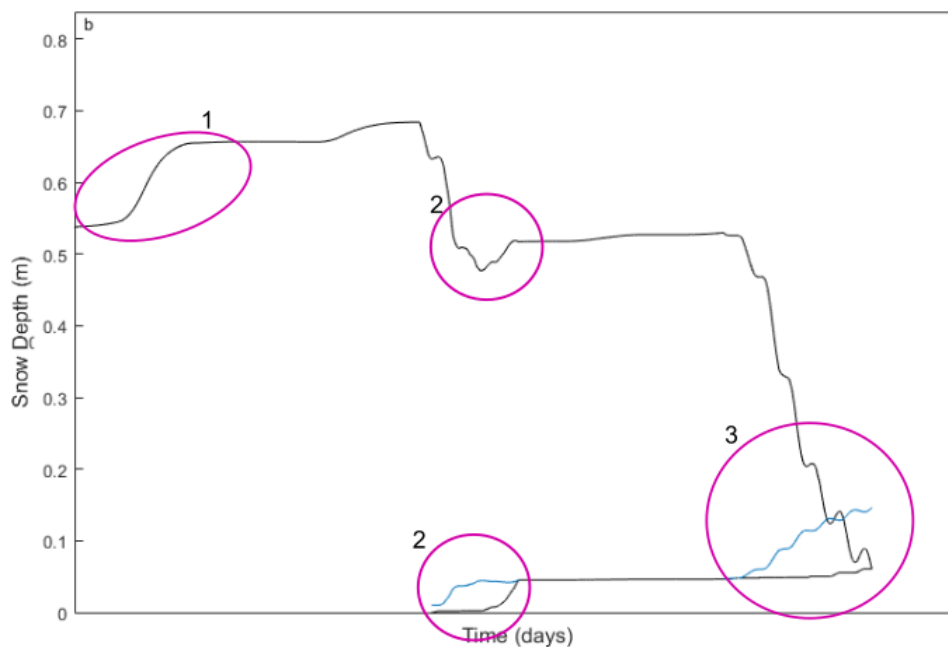


Figure 40: close-up of snow layer behaviour in figure 38. Highlighted areas are discussed in table x.

## Sensitivity testing

Results of the sensitivity testing give an idea of how much confidence can be placed in the model if the values of parameters are uncertain. Due to the exact range under consideration for each parameter being unclear, explicit uncertainty ranges were not derived, but the sensitivity coefficient values allow a good comparative basis for the importance of each parameter tested. Overall, figure 22 shows that most uncertainty is confined to a the  $I_0$  value and that the model is fairly insensitive to most changes. In addition, the trends described below (and seen in the results) show that small perturbations to model setup do manifest themselves in the output in an expected manner, even if only on a very small scale. This shows that the model is receptive to minute changes in forcing or parameter space, and adds confidence to its functioning in a realistic fashion. Below, the impact of altering each parameter is discussed in turn, and possible reasons are given for the choice of a default value if necessary.

#### Temperature of incoming water

Benedek (2014) found the impact of varying incoming water temperature from 0.5 °C to 2.5 °C to be small, and this is borne out here. Although small, there is a very clear linear trend for increasing first season lake depth with increasing incoming water temperature, but a change of 2 °C only increases lake depth by 6 cm (0.7%). There is effectively no impact on any other outputs, with extremely small, or zero value sensitivity coefficients. For the choice of incoming water temperature, a study modelling the formation of lateral meanders in supraglacial meltwater systems used a temperature difference between water and surrounding (temperate) ice of between 0.05 and 0.5 °C (Karlstrom et al., 2013), but found that to fit field data accurately, a temperature of < 0.05°C was required. For Antarctic ice shelves, Buzzard (2017) incorporated incoming water at freezing point as meltwater there predominately passes through firn towards the lake domain, meaning it is isothermal with its surroundings. Given that meltwater in the ablation zone of the GrIS is mostly observed to pass overland rather than through firn (Smith et al., 2017), it is unlikely to be isothermal with temperate snow and ice. For these reasons, a value of 0.01 °C is retained as the default incoming water temperature.

#### Albedo variation

Incoming shortwave radiation is the dominant component of energy transfer during summer, so it is unsurprising that a small perturbation to the amount of radiation absorbed results in a large response. Appendix 1, figure 2, reveals large sensitivity coefficient values for lake depth at the end of the first melt season, the time of snow melt and the time of initial lake formation. Altering albedo by 5% leads to around a 5% change in overall lake depth, broadly in agreement with the sensitivity testing of Buzzard (2017). The response is greater outside of this range, but these albedo values are considered less likely. This uncertainty is probably more important for the elevation testing where albedo is derived from snow, ice, and lake properties as there is likely more uncertainty inherent in these values than in the AWS data.

#### The $I_0$ term

Appendix 1, figure 3, shows the  $I_0$  term to be the single largest influence on the lake depth at all points recorded as model outputs. A  $\pm 0.08$  change in its value was responsible for a 0.47 m decrease or 0.32 m increase in end of melt season lake depth, respectively. Due to this sensitivity it was found to have a large impact on model accuracy and final results; a full discussion is provided following the Tedesco et al. (2012) comparison.

#### Shortwave extinction coefficient for water

Lüthje et al. (2006), Benedek (2014) and Buzzard (2017) all use a constant shortwave extinction coefficient for water ( $T_{\text{water}}$ ) of 0.025 following Taylor and Feltham (2004) who used it in their sea-ice model. Conversely, Saloranta and Andersen (2007) base the attenuation of shortwave radiation for MyLake on the concentrations with depth of suspended sediment load and phytoplankton. The latter is not important in Greenland but it is likely that the former may play a role, especially as algal blooms and particulates are observed to be widespread across the ablation zone (Bøggild et al., 2010; Yallop et al., 2012; Benning et al., 2014), and as some studies find water clarity to play an important role in energy transfer and stratification (Heiskanen et al., 2015). In addition, the value of  $T_{\text{water}}$  is variously reported as being between 0.01 and 0.05  $\text{m}^{-1}$  in the scientific literature (Tilzer, 1983) so it is very possible that the value used in this, and former studies, is incorrect. Fortunately, the output sensitivity to this

parameter is low, with no impact on the lake depth at the end of the first melt season. This is probably a result of plausible values all being quite low and therefore not markedly influencing the energy distribution of incoming shortwave radiation. This reasoning may also explain the reason for which Benedek (2014) found path length did not have a great influence on lake-bottom melting, as an increasing path length only fractionally increased an already-small energy sink.

#### Initial surface and basal ice temperature

As detailed in the methods, the initial surface and basal ice temperatures will influence the entire initial temperature profile as this is derived using linear interpolation between the two values. The basal ice temperature also acts as the constant basal boundary condition, so it is expected that the response to surface temperature will be more transient. Starting the model in autumn or winter should enable some degree of convergence to a realistic value for the upper few metres of the profile, before the lake forms. That said, the trend in lake depth at the end of the first melt season is uniformly linear and fairly large, with a change of 20 °C causing a 0.4 m difference. This impact is amplified for the depth at the end of snow melt under the lid, with a 0.8 m difference caused by a 20 °C change, possibly a result of faster basal freeze-up of the lake due to colder ice temperatures just below the lake.

The basal ice temperature also has a clear, linear impact on lake depth at the end of the first melt season, though a 29 °C rise in temperature only prompts a 0.3 m depth increase (3.75%). The most notable impact is on the lake depth under the lid after snow melt, where the same temperature increase causes a 0.6 m depth increase (12.4%). This is to be expected, as the basal boundary temperature is the only active control on the basal freeze-up rate. The fact that there is zero response from the time of snow melt or the time of first lid formation suggests that the basal boundary condition has no discernable impact on the top-most ice cells or snow layer, as the subsurface lake effectively buffers it.

Accurately obtaining the correct initial temperature profile for the model, defined here in relation to the surface and basal temperatures, presents difficulty. Assuming no difference in forcing year-on-year, the temperature profile will undergo an annual cycle as a function of

climatic forcing and advection. As lakes are seen to markedly elevate the temperature of underlying ice during the winter (figure 38), if one was present, but drained before the initiation of another, the temperature profile would be quite different from if a lake were forming for the first time. Advection rates, which vary greatly towards the margins of the ice sheet (Rignot and Kanagaratnam, 2006) would also play a part. Harrington et al. (2015) obtain five profiles (two of which can be specified as inputs) for the ablation zone of western GrIS extending close to the base, but shallow depths are only covered at low resolution. The profiles obtained by Harrington et al. (2015) and recorded in September, show surface temperatures ranging from 0 to -10 °C although the exact depth of the first reading is unclear (0–20 m). The temperature gradient switches sign twice with increasing elevation between 0 and 40 m depth, further adding to the uncertainty. Meierbachtol et al. (2015) provide higher-resolution profiles for the topmost 20 m, with surface values varying between 0° C and -30 °C, and temperature variation decreasing markedly below 12 m (figure 41), though they do not give exact location or elevation data for the cores. Following their data, a constant basal value of -5 °C and a surface value between 0 °C and -10 °C seems reasonable. Prescribing a much colder surface temperature may have an unrealistic impact on deeper ice in the interpolated initial profile. Uncertainty at depth is mitigated by an additional 10, 1 m cells at the base of the domain which could be extended for future IceLake experiments.

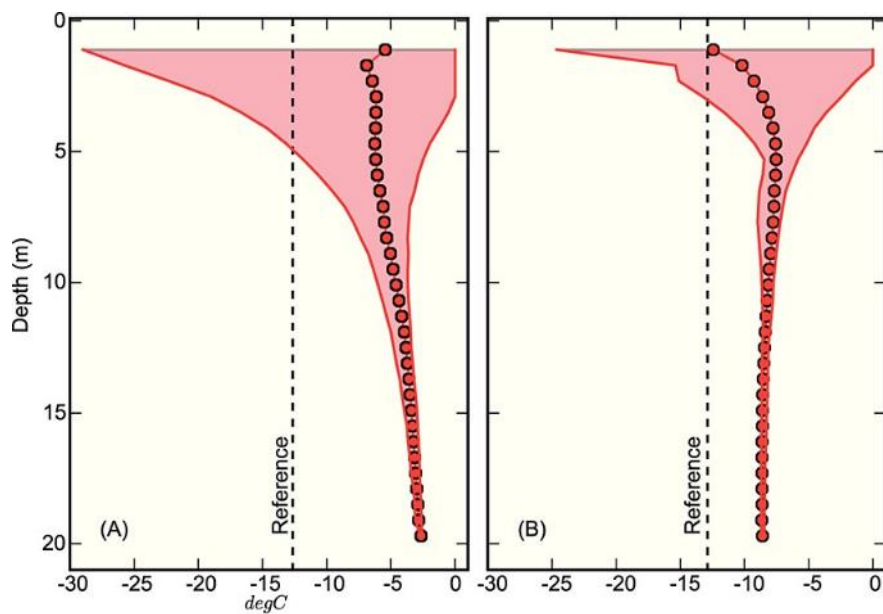


*Figure 41: measured temperatures in two boreholes from the western margin of the GrIS at 67°N and 600 and 800m elevation respectively. Red circles are the ablation averaged mean and boundary lines are maximum and minimum temperatures recorded. From Meierbachtol et al. (2015).*

### Hydrograph input variation

Hydrograph input is the least uniform forcing for the model. As outlined in chapter x it is as much a function of elevation as it is of catchment area, with order of magnitude variation even in adjacent catchments. The standard input used for these tests allows the hydrograph's influence beyond simply adding water to be examined. It appears that the impact of changing the hydrography multiplication factor is linear, i.e. it does not greatly perturb the system beyond its own addition. The non-linear response of lake depth at the end of the first melt season is not the result of a change in basal melt rate, rather, the initial decrease is due to an early transient lid forming, obscuring the true depth before lid formation and the later increase is rebound as this effect disappears. These sensitivity tests show that accurate hydrograph input and maximum lake depth must be obtained if lake specific conclusions, rather than broad trends, are required.

### Precipitation and its absence

The quantity of precipitation has a notable influence across the model outputs tested. A two-fold increase in precipitation leads to a 0.5 m decrease in maximum lake depth, probably linked to the lake forming 10 days later. Additionally, although extra snow would lead to a greater initial lake depth, it is likely that the low conductivity of the snow layer insulates cold underlying ice (which undergoes a clear reduction in temperature before the snow layer thickens significantly) and prompts slower melt than if there is no snow, or only a thin layer. The amount of snow unsurprisingly influences the date of snowmelt atop the lid, and also prolongs the life of the lid. Figure 20 shows the impact of removing the snow layer entirely with features described in table 5. As seen, the inclusion of the snow layer, one of the largest distinctions between IceLake and the work of Lüthje et al. (2006) and Benedek (2014), is an important component in making IceLake behaviour more realistic over seasonal-to-annual

time periods. The quantity of snow also exerts a strong influence on lid growth rates and is discussed in relation to elevation-evolution relationship results later.

Number	Comments
1	Deeper, longer lasting slush swamp than if the snow layer is used. Possibly a result of warmer ice underneath which has not been insulated to keep a cold winter temperature.
2	Close-up in middle panel.
3	Distinct, sharp mid-winter cold patches due to no insulation or modulation from an overlying snow layer.
4	Close-up in bottom panel. Lid thickness is 0.5m greater when no snow is present due to lack of insulation.
5	Lake transitions between all slush and all water several times before full lid break-up. Possibly due to lid break up earlier in the season when occasional cold weather snaps persist.
6	Diurnal temperature variations propagating into the lid with a phase difference of approximately half a day.
7	Lid continues reforming even after melt of the upper section. With snow included the lid would still be entirely snow covered at this point, so this probably represents susceptibility to late winter warm spells when no insulation is present.
8	Water temperatures which are probably unrealistically high due to turbulence not being accounted for.
9	Final transient occurrence of ice comes just before ice lid is seen to break-up when snow is included.
10	Diurnal temperature variations seen to propagate through the entire ice lid and cause transient slush cells at the top of the covered lake.

*Table 5, discussion of points highlighted in figure 20.*

Another important factor to discuss is snow drift, widely acknowledged to influence snow properties, valley-glacier development, and-ice sheet mass balance amongst other cryosphere processes (Purves et al., 1999; Gallée et al., 2001; Libois et al., 2014). For permafrost lakes, which can be treated as proxies for supraglacial lakes, Duguay et al. (2003) observed significant variability within some study areas (~10 km<sup>2</sup>), with the depth of snow over lakes sometimes being thin and dense to non-existent, even if thick snow cover was observed in the surroundings. As snow drift is frequently observed on the GrIS (Box and Stefen, 2001), it is likely that the actual quantity of snow overlying the ice lid could easily be misrepresented. Predicting snow cover including snow drift would require coupling IceLake

to a snow-drift model such as Walter et al. (2004), although inaccuracies may still persist even if they were implemented and DEM data would be required for verification.

#### Snow compaction timescale

The snow compaction timescale is identified as important by Essery (2015) in the snowpack model on which this model is based, however varying its value has little impact on model outputs (though its effect on snow depth is clearly seen in figure 29). Even a comparatively extremely low value does little to perturb model results.

#### Initial snow density

Initial snow density has surprisingly little effect on most outputs considered, notably on the time of first lake formation, suggesting that either snow density is of little importance in snowpack energy absorption or that the snowpack model implemented here does not accurately capture this effect. The largest impact is on the lake depth beneath the lid after snow melt, with greater density associated with shallow subsurface lakes. As greater snow density leads to greater thermal conductivity, the observed trend is probably the impact of more heat escaping from the lake during winter months.

#### Break-up threshold

Sensitivity coefficients for every output were zero suggesting it is not important for the outcome whatsoever. For this reason, it is omitted from the overall analysis. This means that the averaging of lake enthalpies upon breakup does not noticeably alter model results.

#### Implementation of longwave calculation

Both Benedek (2014) and Lüthje et al. (2006) calculate incoming longwave radiation as detailed in the methods. Figure 24 displays the model output if incoming longwave is calculated following Benedek (2014) and figure 23 shows the difference in model output depending on which model is used. As the output variation is independent of a continuous parameter, sensitivity coefficients comparable to those above cannot be obtained. Visual

inspection however shows the impact to be very large, with an impact on lake depth at the end of the first melt season comparable to that of changing  $l_{o\_water}$  from 0.54 to 0.69 (i.e. the range used in calculating the sensitivity coefficient). The effect on lake depth is amplified moving to lake depth after snow melt under lid and lake depth after lid break-up with a total difference at the start of the second melt season of 0.8 m (~8%). An additional impact is on the timing of lid formation and break-up, an output which has proven fairly insensitive to other parameter tests. The lid forms 2 days later than when AWS longwave is used, and breaks up nearly a week later.

### Time step

If time step is increased ten-fold (meaning a comparable reduction in model run time) the model holds up well (figure 21), exhibiting the stability of the model. If the divergence associated with a two-hour time step were deemed acceptable, the model could be used in a holistic hydrology model with an even lower computational expense.

### Improving upon the sensitivity testing

The sensitivity testing presented here could be improved upon by following the approach of Saloranta and Andersen (2007), and coupling IceLake to an Extended Fourier Amplitude Sensitivity Test (Extended FAST) such as that presented by Saltelli et al. (1999). In this method, parameters are sampled from each distinct model run from a wave-like form with incommensurate frequencies, meaning the sampling takes good coverage of the entire multidimensional parameter space. This would allow higher-order interactions with other parameters to be detected. Complete testing in this manner could be carried out using ~10,000 runs and would take ~80 hours to complete. The model could also be used in a simple Monte Carlo simulation to obtain a probability distribution of lid thickness at the start of the melt season as a function of a predefined probability distribution of snow-layer thickness.

### Model validation: comparison to Tedesco et al. (2012)

The comparison to field data from Tedesco et al. (2012) shows that the model can accurately predict the lake depth-day relationship, even if it is started at the end of the preceding melt season. It shows that the parameter values selected are suitable, that the treatment of the snow layer is correct (as without it, the results vary markedly), and that the ice temperature profile at the time of lake formation is accurate, or does not impede the correct time of lake formation and rate of basal melting. The good agreement also indicates that the new heat diffusion discretization works well. The only uncertainty in this analysis is that the lake data from Tedesco et al. (2013) begins at 0.7 m, and it is not clear if the main component of this is basal melting or meltwater input from the surrounding catchment. The placement of the observation data in figure 26 assumes the former, which is reasonable since the hydrograph data of Arnold et al. (2014) show little water input at the beginning of the melt season.

#### Model inter-comparison with Buzzard et al. (2018)

It was expected that forcing the model of Buzzard et al. (2018) with the same weather data as IceLake would yield similar results. Figure 28 shows that this is not the case, with the lake forming over two months earlier than expected. It is not clear exactly why this occurs: it is possible that the model works poorly on solid ice, although the initial density was set to that of ice. IceLake functions  $\sim 150 \times$  faster than Buzzard et al's. (2018) model and does not require a spin-up period which further increases run time.

#### The $I_0$ term: further discussion

This study showed that model sensitivity to the value of  $I_0$  is large, that an  $I_0$  value of 0.35 best replicates field measurements, and that if other parameter values are held constant, an  $I_0$  value of 0.6 as used by Lüthje et al. (2006), Tedesco et al. (2012), Benedek (2014) and Buzzard et al. (2018) results in an overestimation of lake depth. The good performance of the model, as seen above and below, and the dominance of the  $I_0$  term in the uncertainty analysis suggests that an incorrect  $I_0$  value is responsible for the departure from the field measurements of Tedesco et al. (2012) when an  $I_0$  value of 0.6 is used, rather than poor model skill. Examining the history of the  $I_0$  term, its implementation in models appears to have changed over decades. Ebert and Curry (1993) use  $I_0$  in the Beer-Lambert law (equation 8)

when calculating shortwave energy absorption in ice with brine pockets, not when a meltwater lake is present where they use the equation

$$F_p = F_{SW} [a_p + a_p \alpha_i t_p + t_p (1 - \alpha_i) (1 - I_0)] \quad (35)$$

where:

$a_p$  = fraction of shortwave absorbed by the pond

$\alpha_i$  = bare ice albedo

$t_p$  = pond transmissivity as a function of depth

$I_0$  = fraction of ice shortwave to penetrate ice

They take an  $I_0$  value that varies with cloud cover, with a maximum value of 0.35 under cloudy skies and a minimum value of 0.18 under clear skies, following Grenfell and Maykut (1977). This reflects the fact that there is more incoming radiation in the infrared range under clear skies, most of which is absorbed in the upper 10 cm of the ice profile (Grenfell and Maykut, 1977).

Lüthje et al. (2006) deviate and take  $I_0$  as the proportion of shortwave radiation that propagates below the surface water layer, as does this model. They use 0.6 as the value of  $I_0$  as Grenfell (1979), finding the fraction of incident shortwave radiation above 700 nm (i.e. infrared) to be 40% (in disagreement with Kirk (1988) who suggests a value of 50%). This is as infrared radiation is strongly absorbed by the top 0.5 m of the water profile (Kirk, 1988). The calculation of Lüthje et al. (2006) however, excludes reflection back from the bare ice surface so may result in an oversupply of shortwave radiation to the upper ice layers beneath the lake. Lüthje et al. (2006) do not run sensitivity tests of the  $I_0$  value and it is subsequently used in Tedesco et al. (2012), Buzzard et al. (2018) and the sea ice lake model of Scott and Feltham (2010) amongst others, without further testing. Benedek (2014) tests the impact of varying this parameter between 0.4 and 0.6, finding minimal differences for a 5-day run, contrasting with the large impact observed here over longer model runs.

The importance of the  $l_0$  term is that a proportion of incoming shortwave radiation,  $(1 - l_0)$ , will not be factored into the Beer-Lambert law and will therefore not be accessible to the underlying ice. As the temperature profile is averaged later in the time step, it is not distorted by extra energy addition to the surface cell. The large sensitivity coefficient arises as a greater  $l_0$  means a greater energy flux for the upper ice cells, as shortwave infiltration is a more effective transfer mechanism than turbulent transfer and heat diffusion. This can be thought of as being equivalent to an  $l_0$  value of 1 (i.e. all shortwave radiation enters the water column) and having a certain fraction of water that penetrates to the lake base reflected backwards. In light of these points, the  $l_0$  term in its form used here is tweaked to obtain the closest match with field results as it is the model parameter that is least tied to in-depth studies and is no longer related to its original use. It is likely that an  $l_0$  value of 0.35 better represents reflection back from the water-ice or water-slush interface.

### **Application: elevation relationships**

#### RACMO-UPE-U comparison

As explained in the methods, RACMO data was chosen over altering PROMICE AWS data so that an existing published, extensively tested data set could be used, and to allow easy application to the entire ice sheet if necessary. The most notable difference in output when RACMO data is used is the lack of clear diurnal variation in surface energy flux due to the coarse 12-hour resolution, and the presence of high magnitude energy fluxes in the middle of winter, a feature that is entirely absent when using the UPE-U data (figure 32, left). This has the unrealistic effect of melting the snow nearly entirely before a large refreeze causes a thick snow-ice layer (figure 32: right). Overall, the agreement between the two (i.e. 2-day difference in lid formation, 12% difference in lake depth) is sufficient to use RACMO data to derive broad elevation-evolution trends, especially as any inconsistency is likely to affect each section of the chosen transect equally.

#### Elevation-lake evolution relationship

Of the five output variables tested, four show a clear increase or decrease with elevation (the initial decrease in lid break-up day results from the erroneous snow-layer behaviour outlined above). Entirely consistent with expectations of a colder environment as elevation increases, the date of lake formation is pushed back, total lake depth at the end of the first melt season decreases, and the lid remains present for longer. The unexpected result is that lid thickness only shows a consistent, increasing trend above 1800m. The clear reason for this is snow cover: the 2-m-thick lid at sea level is a result of the snow layer not forming correctly, allowing latent lake energy to escape through the uninsulated lid in the depths of winter. The same reasoning applies to the thick lid seen in figure 33, d, where initial snow melt has prompted a layer of snow-ice, thereby reducing the thickness of insulating snow and again allowing the escape of latent lake energy. The increase in lid thickness above 1800 m occurs with full snow thickness atop the lid, indicating a control from the increasing atmospheric-lake temperature gradient. This conclusion is supported by figures x and y, showing a clear increase in lid depth from 2.25 m to 2.53 m when the snow layer is omitted, and a decrease in elevation needed for complete lake freeze-up of over 400 m.

Aside from these relationships, figures x and y reveal that so long as the lake is present throughout winter, even if it is entirely comprised of slush cells at the start of the following melt season, underlying ice continues to warm as a result of the 0 °C lake bottom boundary condition. Even in figure 34, n, where at 2208 m the lake is seen to freeze entirely, the insulated ice remains above -5 °C and enables a deeper lake to form the following melt season. Poinar et al. (2015) point to the presence of 'slush swamps' at 66.5°N on the west coast at an elevation of 1900 m with fuzzy boundaries. This result is nicely replicated here, with the lake at 1972 m (figure 34, k) comprised of slush for the majority of its presence with only a few days showing a full water column. It is difficult to comment on the relation of these results to the ELA, as this measures the point of zero surface mass balance and does not assume that melt remains *in situ* (i.e. bare ice melting rates). The continuation of lakes beyond the equilibrium line altitude (Van de wal et al., 2012), and 200 m beyond the uppermost buried lake observed by Koenig et al. (2015) does suggest however, that melt may be overestimated by IceLake, though melt is occasionally seen at such great elevations (Ngheim et al., 2012). This overestimation may be the result of insufficient snow input over winter as snowfall for sea level is used, the greater melting observed when RACMO data is used in place

of AWS data, or the model not correctly replicating lakes at higher elevations. The latter is entirely possible as firn rather than ice is found at these elevations and meltwater percolation into the firn would impede lake formation, making the model of Buzzard et al. (2018) a more suitable choice.

The results show very good agreement with the radar observations of Koenig et al. (2015). The thickness of snow overlying the lake is predominantly controlled by incoming precipitation (i.e. it is not heavily influenced by the model) and is likely to vary with locality and year, but a maximum value of 1.2 m does fall well within the range of Koenig et al. (2015). The average ice lid thickness of 1.4 m recorded by Koenig et al. (2015), with a range from 0.4-4.58 m, shows excellent agreement with the mean thickness of 1.45 m obtained here across the elevational transect. Although untested, it is likely that far thicker snow cover could be responsible for insulating a thin, 0.4 m lid. No explanation can be offered for a thickness of 4.58 m as this greatly exceeds the maximum depth of 2.71 m observed at RACMO grid cell n with abundant hydrograph input and no snow layer. Given this great disparity, it is perhaps more likely that this results from an observational error in the radar data. These results do not agree with the suggestion of Miles et al. (2017) that the lakes freeze-through entirely. The disparity is likely due to the C-band radar used by Miles et al. (2017) only penetrating to a few metres and the full lake presence being hidden from view.

### **Possible model improvements**

#### Lake surface area

One of the clearest improvements, which would enable modelling of lake areas along with lake depths, would be to allow a radially shallowing lake depth. This would be similar to the functionality of MyLake1.2 (Saloranta and Andersen, 2007), which incorporates varying volume as a function of depth by allowing a relationship to be specified between width and depth. In the case of average GrIS supraglacial lake bathymetry (Box and Ski, 2007), this would mean that inflow would first lead to a quick increase in surface area, followed by a slower and more steady increase, and lastly a quick increase again. One way to model lake area change with inflow volume, without fully implementing a changing grid width with depth, would be

to approximate the lake form to a sigmoid function, or a cylinder as in Koziol et al. (2017), and multiply surface energy exchange,  $q$ , accordingly. If lake temperature were assumed to be constant across its base, the relationship could be extended to heat transfer at the lake base as, due to the very low bathymetry gradients observed in GrIS supraglacial lakes, it approximates the surface area. Another clear improvement would be to replace the shortwave propagation calculation and  $I_0$  usage of Lüthje et al. (2006) with that of Ebert and Curry (1993) as outlined in the  $I_0$  discussion.

#### Further validation

Further validation could be carried out by comparing results to remote-sensing calculations of lake area and volume (e.g. Selmes et al., 2011, 2013; Williamson et al., 2018a, 2018b) or using a pre-existing tracking algorithm to derive tailored validation data. Tedesco et al. (2012) also present lake bottom ablation data for 2010 which could be used to add confidence in IceLake output.

#### 2-Dimensional extension

The speed of the model setup would mean that it would be feasible to extend the model to a 2-dimensional domain. Along with a more accurate physical representation of the lakes, this would mean that the effects of advecting ice on lake bathymetry and basal ice temperature could be quantitatively examined. It would also be possible to investigate crevasse healing rates over winter and the impact of an overlying lake on them.

#### Albedo

Improvements could also be made by more accurately calculating surface energy flux by using spectral albedo rather than bulk albedo, as the albedo of snow, ice and melt ponds is seen to vary markedly with wavelength (figure 42), and the incoming radiation spectrum varies with cloud cover. This variation was accounted for in Ebert and Curry (1993), who developed a four band approach for incoming radiation but excluded in following models. The impact this could have on model output would be similar to changing the albedo, as in the sensitivity testing

(appendix 1, figure 2), as it would influence the shortwave energy flux that enters the model domain. The sensitivity coefficients for albedo are the second-most important unknown quantity after  $I_0$ , so improvements in albedo calculations have the potential to improve model accuracy. For modelling purposes, Cathles (2011) showed that the best representation of surface energy transfer is achieved when spectral albedo is divided into 18 discrete bands. One method of implementing this would be using software such as libRadTran, which can compute the spectral impact of clouds (Emde et al., 2016), to process AWS data based on algorithms applied to define cloud cover from satellite imagery, before calculating the bulk shortwave transfer based on spectral albedo at each time step.

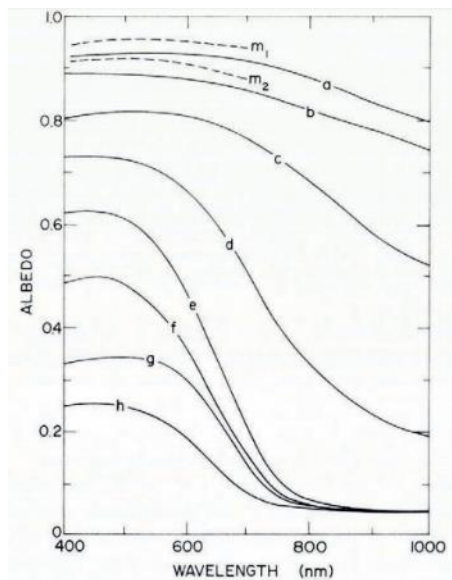


Figure 42: spectral albedos over snow and melt ponds. Selected lines: a, dry snow, c, melting old snow, e, early-season melt pond, h, old melt pond. From Grenfell and Maykut (1977).

## **Conclusion**

This study has presented the first model for the full multi-year evolution of supraglacial lakes in the ablation zone of Greenland. This model therefore represents the most comprehensive among all existing models used to investigate surface lakes on ice masses. IceLake can effectively replicate field data for ablation and lake formation from Tedesco et al. (2012) and lid thickness from Koenig et al. (2015). IceLake shows that winter lids thicker than 2.5 m with no snow cover, or 1.8 m with snow cover, are unlikely to form at elevations where lakes are commonly observed (Koenig et al., 2015). This means most lakes will effectively impede

cooling of underlying ice throughout winter, with potentially important ramifications for enabling moulines to persist year on year (Catania and Neumann, 2010), and for the development of the supraglacial hydrological system in the following melt season due to a pre-existing latent heat store. The computational efficiency of IceLake means it could be incorporated into a holistic model of Greenland supraglacial hydrology without impeding run time, and that it could be easily used in ice sheet-wide studies. IceLake could also be easily adapted to valley glacier supraglacial lakes and possibly to Antarctica, where lakes are seen in increasing number (Langley et al., 2016), if firn could be incorporated.

These results are vital for better understanding the role of lakes in forming surface-bed linkages within inland sectors and marine-terminating regions of the GrIS, where the transfer of supraglacial meltwater to the subglacial hydrological system may have more significant implications for ice dynamics. It is hoped that the work presented here will feed into an overall better understanding of GrIS surface-melt processes; such processes ultimately drive a significant and accelerating component of global sea-level rise.

## **References**

Alexiades, V., & Solomon, A. D. (1993). Mathematical modeling of melting and freezing processes. Hemisphere Pub. Corp.

ALLEY, R. B., & WHILLANS, I. M. (1991). Changes in the West Antarctic Ice Sheet. *Science*, 254(5034), 959–963. <https://doi.org/10.1126/science.254.5034.959>

Alley, R. B., Dupont, T. K., Parizek, B. R., & Anandakrishnan, S. (2005). Access of surface meltwater to beds of sub-freezing glaciers: preliminary insights. *Annals of Glaciology*, 40, 8–14. <https://doi.org/10.3189/172756405781813483>

AMAP. (2017). Snow, Water, Ice and Permafrost in the Arctic (SWIPA) 2017. Arctic Monitoring and Assessment Programme (AMAP), Oslo, Norway. xiv + 269 pp.

American Meteorological Society. (2012). Mixing ratio - AMS Glossary. Retrieved June 8, 2018, from [http://glossary.ametsoc.org/wiki/Mixing\\_ratio](http://glossary.ametsoc.org/wiki/Mixing_ratio)

Anthoff, D., Nicholls, R. J., Tol, R. S. J., & Vafeidis, A. T. (2006). Global and regional exposure to large rises in sea-level: a sensitivity analysis. Retrieved from [http://dcms2.lwec.ulcc.ac.uk/sites/default/files/wp96\\_0.pdf](http://dcms2.lwec.ulcc.ac.uk/sites/default/files/wp96_0.pdf)

- Arnold, N. S., Banwell, A. F., & Willis, I. C. (2014). High-resolution modelling of the seasonal evolution of surface water storage on the Greenland Ice Sheet. *The Cryosphere*, 8(4), 1149–1160. <https://doi.org/10.5194/tc-8-1149-2014>
- Bamber, J. L., Alley, R. B., & Joughin, I. (2007). Rapid response of modern day ice sheets to external forcing. <https://doi.org/10.1016/j.epsl.2007.03.005>
- Banwell, A. F., Arnold, N. S., Willis, I. C., Tedesco, M., & Ahlstrøm, A. P. (2012). Modeling supraglacial water routing and lake filling on the Greenland Ice Sheet. *Journal of Geophysical Research: Earth Surface*, 117(F4), n/a-n/a. <https://doi.org/10.1029/2012JF002393>
- Banwell, A., Hewitt, I., Willis, I., & Arnold, N. (2016). Moulin density controls drainage development beneath the Greenland ice sheet. *Journal of Geophysical Research: Earth Surface*, 121(12), 2248–2269. <https://doi.org/10.1002/2015JF003801>
- Benn, D. I., & Evans, D. J. A. (2010). *Glaciers and glaciation*. London: Hodder Education.
- Benning, L. G., Anesio, A. M., Lutz, S., & Tranter, M. (2014). Biological impact on Greenland's albedo. *Nature Geoscience*, 7(10), 691–691. <https://doi.org/10.1038/ngeo2260>
- Bindschadler, R., Harrison, W. D., Raymond, C. F., & Crosson, R. (1977). Geometry and Dynamics of a Surge-type Glacier. *Journal of Glaciology*, 18(79), 181–194. <https://doi.org/10.3189/S0022143000021298>
- Bindschadler, R., & Vornberger, P. (1992). Interpretation of sar imagery of the greenland ice sheet using coregistered TM imagery. *Remote Sensing of Environment*, 42(3), 167–175. [https://doi.org/10.1016/0034-4257\(92\)90100-X](https://doi.org/10.1016/0034-4257(92)90100-X)
- Bøggild, C. E., Brandt, R. E., Brown, K. J., & Warren, S. G. (2010). The ablation zone in northeast Greenland: ice types, albedos and impurities. *Journal of Glaciology*, 56(195), 101–113. <https://doi.org/10.3189/002214310791190776>
- Boon, S., & Sharp, M. (2003). The role of hydrologically-driven ice fracture in drainage system evolution on an Arctic glacier. *Geophysical Research Letters*, 30(18). <https://doi.org/10.1029/2003GL018034>
- Boone, A., Etchevers, P., Boone, A., & Etchevers, P. (2001). An Intercomparison of Three Snow Schemes of Varying Complexity Coupled to the Same Land Surface Model: Local-Scale Evaluation at an Alpine Site. *Journal of Hydrometeorology*, 2(4), 374–394. [https://doi.org/10.1175/1525-7541\(2001\)002<0374:AIOTSS>2.0.CO;2](https://doi.org/10.1175/1525-7541(2001)002<0374:AIOTSS>2.0.CO;2)
- Box, J. E., & Ski, K. (2007). Remote sounding of Greenland supraglacial melt lakes: implications for subglacial hydraulics. *Journal of Glaciology*, 53(181), 257–265. <https://doi.org/10.3189/172756507782202883>

Box, J. E., & Steffen, K. (2001). Sublimation on the Greenland Ice Sheet from automated weather station observations. *Journal of Geophysical Research: Atmospheres*, 106(D24), 33965–33981. <https://doi.org/10.1029/2001JD900219>

Braithwaite, R. J. (1995). Positive degree-day factors for ablation on the Greenland ice sheet studied by energy-balance modelling. *Journal of Glaciology*, 41(137), 153–160. <https://doi.org/10.3189/S0022143000017846>

Buzzard, S. C., Feltham, D. L., & Flocco, D. (2018). A Mathematical Model of Melt Lake Development on an Ice Shelf. *Journal of Advances in Modeling Earth Systems*, 10(2), 262–283. <https://doi.org/10.1002/2017MS001155>

Catania, G. A., & Neumann, T. A. (2010). Persistent englacial drainage features in the Greenland Ice Sheet. *Geophysical Research Letters*, 37(2), n/a-n/a. <https://doi.org/10.1029/2009GL041108>

Chandler, D. M., Wadham, J. L., Lis, G. P., Cowton, T., Sole, A., Bartholomew, I., ... Hubbard, A. (2013). Evolution of the subglacial drainage system beneath the Greenland Ice Sheet revealed by tracers. *Nature Geoscience*, 6(3), 195–198. <https://doi.org/10.1038/ngeo1737>

Christoffersen, P., Bougamont, M., Hubbard, A., Doyle, S. H., Grigsby, S., & Pettersson, R. (2018). Cascading lake drainage on the Greenland Ice Sheet triggered by tensile shock and fracture. *Nature Communications*, 9(1), 1064. <https://doi.org/10.1038/s41467-018-03420-8>

Christoffersen, P., Bougamont, M., Hubbard, A., Doyle, S. H., Grigsby, S., & Pettersson, R. (2018). Cascading lake drainage on the Greenland Ice Sheet triggered by tensile shock and fracture. *Nature Communications*, 9(1), 1064. <https://doi.org/10.1038/s41467-018-03420-8>

Chu, V. W. (2014). Greenland ice sheet hydrology. *Progress in Physical Geography*, 38(1), 19–54. <https://doi.org/10.1177/0309133313507075>

Cooley, S. W., & Christoffersen, P. (2017). Observation Bias Correction Reveals More Rapidly Draining Lakes on the Greenland Ice Sheet. *Journal of Geophysical Research: Earth Surface*, 122(10), 1867–1881. <https://doi.org/10.1002/2017JF004255>

Cowton, T., Nienow, P., Sole, A., Bartholomew, I., & Mair, D. (2016). Variability in ice motion at a land-terminating Greenlandic outlet glacier: the role of channelized and distributed drainage systems. *Journal of Glaciology*, 62(233), 451–466. <https://doi.org/10.1017/jog.2016.36>

Cowton, T., Nienow, P., Sole, A., Wadham, J., Lis, G., Bartholomew, I., ... Chandler, D. (2013). Evolution of drainage system morphology at a land-terminating Greenlandic outlet glacier. *Journal of Geophysical Research: Earth Surface*, 118, 29–41. <https://doi.org/10.1029/2012JF002540>

Cox, C. J., Walden, V. P., Compo, G. P., Rowe, P. M., Shupe, M. D., & Steffen, K. (2014). Downwelling longwave flux over Summit, Greenland, 2010–2012: Analysis of surface-based

observations and evaluation of ERA-Interim using wavelets. *Journal of Geophysical Research: Atmospheres*, 119(21), 12,317–12,337. <https://doi.org/10.1002/2014JD021975>

Das, S. B., Joughin, I., Behn, M. D., Howat, I. M., King, M. A., Lizarralde, D., & Bhatia, M. P. (2008). Fracture propagation to the base of the Greenland Ice Sheet during supraglacial lake drainage. *Science (New York, N.Y.)*, 320(5877), 778–81. <https://doi.org/10.1126/science.1153360>

Das, S. B., Joughin, I., Behn, M. D., Howat, I. M., King, M. A., Lizarralde, D., & Bhatia, M. P. (2008). Fracture propagation to the base of the Greenland Ice Sheet during supraglacial lake drainage. *Science (New York, N.Y.)*, 320(5877), 778–81. <https://doi.org/10.1126/science.1153360>

De La Peña, S., Howat, I. M., Nienow, P. W., Van Den Broeke, M. R., Mosley-Thompson, E., Price, S. F., ... Sole, A. J. (2015). Changes in the firm structure of the western Greenland Ice Sheet caused by recent warming. *The Cryosphere*, 9, 1203–1211. <https://doi.org/10.5194/tc-9-1203-2015>

Dee, D. P., Uppala, S. M., Simmons, A. J., Berrisford, P., Poli, P., Kobayashi, S., ... Vitart, F. (2011). The ERA-Interim reanalysis: configuration and performance of the data assimilation system. *Quarterly Journal of the Royal Meteorological Society*, 137(656), 553–597. <https://doi.org/10.1002/qj.828>

Doyle, S. H., Hubbard, A., Fitzpatrick, A. A. W., van As, D., Mikkelsen, A. B., Petterson, R., & Hubbard, B. (2014). Persistent flow acceleration within the interior of the Greenland ice sheet. *Geophysical Research Letters*, 41(3), 899–905. <https://doi.org/10.1002/2013GL058933>

Duguay, C. R., Prowse, T. D., Bonsal, B. R., Brown, R. D., Lacroix, M. P., & Ménard, P. (2006). Recent trends in Canadian lake ice cover. *Hydrological Processes*, 20(4), 781–801. <https://doi.org/10.1002/hyp.6131>

Duguay, C. R., Flato, G. M., Jeffries, M. O., Ménard, P., Morris, K., & Rouse, W. R. (2003). Ice-cover variability on shallow lakes at high latitudes: model simulations and observations, 17, 3465–3483. <https://doi.org/10.1002/hyp.1394>

Ebert, E. E., & Curry, J. A. (1993). An intermediate one-dimensional thermodynamic sea ice model for investigating ice-atmosphere interactions. *Journal of Geophysical Research*, 98(C6), 10085. <https://doi.org/10.1029/93JC00656>

Echelmeyer, K., Clarke, T. S., & Harrison, W. D. (1991). Surficial glaciology of Jakobshavns Isbræ, West Greenland: Part I. Surface morphology. *Journal of Glaciology*, 37(127), 368–382. <https://doi.org/10.3189/S0022143000005803>

Emde, C., Buras-Schnell, R., Kylling, A., Mayer, B., Gasteiger, J., Hamann, U., ... Bugliaro, L. (2016). The libRadtran software package for radiative transfer calculations (version 2.0.1). *Geosci. Model Dev*, 9, 1647–1672. <https://doi.org/10.5194/gmd-9-1647-2016>

Essery, R. (2015). A factorial snowpack model (FSM 1.0). *Geoscientific Model Development*, 8(12), 3867–3876. <https://doi.org/10.5194/gmd-8-3867-2015>

Ettema, J., Van Den Broeke, M. R., Van Meijgaard, E., Van De Berg, W. J., Box, J. E., & Steffen, K. (2010). Climate of the Greenland ice sheet using a high-resolution climate model – Part 1: Evaluation. *The Cryosphere*, 4, 511–527. <https://doi.org/10.5194/tc-4-511-2010>

Fahnestock, M., Abdalati, W., Joughin, I., Brozena, J., & Gogineni, P. (2001). High geothermal heat flow, Basal melt, and the origin of rapid ice flow in central Greenland. *Science (New York, N.Y.)*, 294(5550), 2338–42. <https://doi.org/10.1126/science.1065370>

Fausto, R. S., Van As, D., Ahlstrøm, A. P., & Citterio, M. (2012). Assessing the accuracy of Greenland ice sheet ice ablation measurements by pressure transducer. *Journal of Glaciology*, 58(212), 1144–1150. <https://doi.org/10.3189/2012JoG12J075>

Fetterer, F., & Untersteiner, N. (1998). Observations of melt ponds on Arctic sea ice. *Journal of Geophysical Research: Oceans*, 103(C11), 24821–24835. <https://doi.org/10.1029/98JC02034>

Fettweis, X., Franco, B., Tedesco, M., Van Angelen, J. H., Lenaerts, J. T. M., Van Den Broeke, M. R., & Gallée, H. (2013). Estimating the Greenland ice sheet surface mass balance contribution to future sea level rise using the regional atmospheric climate model MAR. *The Cryosphere*, 7, 469–489. <https://doi.org/10.5194/tc-7-469-2013>

Fitzpatrick, A. A. W., Hubbard, A. L., Box, J. E., Quincey, D. J., van As, D., Mikkelsen, A. P. B., ... Jones, G. A. (2014). A decade (2002-2012) of supraglacial lake volume estimates across Russell Glacier, West Greenland. *The Cryosphere*, 8(1), 107–121. <https://doi.org/10.5194/tc-8-107-2014>

Flocco, D., Feltham, D. L., Bailey, E., & Schroeder, D. (2015). The refreezing of melt ponds on Arctic sea ice. *Journal of Geophysical Research: Oceans*, 120(2), 647–659. <https://doi.org/10.1002/2014JC010140>

Flowers, G. E. (n.d.). Modelling water flow under glaciers and ice sheets. <https://doi.org/10.1098/rspa.2014.0907>

Forster, R. R., Box, J. E., van den Broeke, M. R., Miège, C., Burgess, E. W., van Angelen, J. H., ... McConnell, J. R. (2014). Extensive liquid meltwater storage in firn within the Greenland ice sheet. *Nature Geoscience*, 7(2), 95–98. <https://doi.org/10.1038/ngeo2043>

Forster, R. R., Box, J. E., van den Broeke, M. R., Miège, C., Burgess, E. W., van Angelen, J. H., ... McConnell, J. R. (2014). Extensive liquid meltwater storage in firn within the Greenland ice sheet. *Nature Geoscience*, 7(2), 95–98. <https://doi.org/10.1038/ngeo2043>

Gallée, H., Guyomarc'h, G., & Brun, E. (2001). Impact Of Snow Drift On The Antarctic Ice Sheet Surface Mass Balance: Possible Sensitivity To Snow-Surface Properties. *Boundary-Layer Meteorology*, 99(1), 1–19. <https://doi.org/10.1023/A:1018776422809>

Gledhill, L. A., & Williamson, A. G. (2017). Inland advance of supraglacial lakes in north-west Greenland under recent climatic warming. *Annals of Glaciology*, 1–17. <https://doi.org/10.1017/aog.2017.31>

Goelzer, H., Nowicki, S., Edwards, T., Beckley, M., Abe-Ouchi, A., Aschwanden, A., ... Ziemen, F. A. (2018). Design and results of the ice sheet model initialisation experiments initMIP-Greenland: an ISMIP6 intercomparison, 125194, 1433–1460. <https://doi.org/10.5194/tc-12-1433-2018>

Grenfell, T. C., and G. A. Maykut (1977), The optical properties of ice and snow in the Arctic Basin, *J. Glaciol.*, 18, 445 – 463.

Hall, D. K., Comiso, J. C., DiGirolamo, N. E., Shuman, C. A., Box, J. E., & Koenig, L. S. (2013). Variability in the surface temperature and melt extent of the Greenland ice sheet from MODIS. *Geophysical Research Letters*, 40(10), 2114–2120. <https://doi.org/10.1002/grl.50240>

Harrington, J. A., Humphrey, N. F., & Harper, J. T. (n.d.). Temperature distribution and thermal anomalies along a flowline of the Greenland ice sheet. <https://doi.org/10.3189/2015AoG70A945>

Harris, I., Jones, P. D., Osborn, T. J., & Lister, D. H. (2014). Updated high-resolution grids of monthly climatic observations - the CRU TS3.10 Dataset. *International Journal of Climatology*, 34(3), 623–642. <https://doi.org/10.1002/joc.3711>

Hawkings, J. R., Benning, L. G., Raiswell, R., Kaulich, B., Araki, T., Abyaneh, M., ... Tranter, M. (2018). Biolabile ferrous iron bearing nanoparticles in glacial sediments. *Earth and Planetary Science Letters*, 493, 92–101. <https://doi.org/10.1016/J.EPSL.2018.04.022>

Heiskanen, J. J., Mammarella, I., Ojala, A., Stepanenko, V., Erkkilä, K.-M., Miettinen, H., ... Nordbo, A. (2015). Effects of water clarity on lake stratification and lake-atmosphere heat exchange. *Journal of Geophysical Research: Atmospheres*, 120(15), 7412–7428. <https://doi.org/10.1002/2014JD022938>

Heron, R., & Woo, M.-K. (1994). Decay of a High Arctic lake-ice cover: observations and modelling. *Journal of Glaciology*, 40(135), 283–292. <https://doi.org/10.3189/S0022143000007371>

Hodson, A. J., & Ferguson, R. I. (1999). Fluvial suspended sediment transport from cold and warm-based glaciers in Svalbard. *Earth Surface Processes and Landforms*, 24(11), 957–974.

Hoffman, M. J., Perego, M., Andrews, L. C., Price, S. F., Neumann, T. A., Johnson, J. V., ... Lüthi, M. P. (2018). Widespread Moulin Formation During Supraglacial Lake Drainages in

Greenland. *Geophysical Research Letters*, 45(2), 778–788.

<https://doi.org/10.1002/2017GL075659>

Hoffman, M. J., Perego, M., Andrews, L. C., Price, S. F., Neumann, T. A., Johnson, J. V., ... Lüthi, M. P. (2018). Widespread Moulin Formation During Supraglacial Lake Drainages in Greenland. *Geophysical Research Letters*, 45(2), 778–788.

<https://doi.org/10.1002/2017GL075659>

Howat, I. M., Negrete, A., & Smith, B. E. (2014). The Greenland Ice Mapping Project (GIMP) land classification and surface elevation data sets. *The Cryosphere*, 8, 1509–1518.

<https://doi.org/10.5194/tc-8-1509-2014>

Hubbard, B., Luckman, A., Ashmore, D. W., Bevan, S., Kulesa, B., Kuipers Munneke, P., ... Rutt, I. (2016). Massive subsurface ice formed by refreezing of ice-shelf melt ponds. *Nature Communications*, 7, 11897. <https://doi.org/10.1038/ncomms11897>

Hubbard, B., & Nienow, P. (1997). Alpine subglacial hydrology. *Quaternary Science Reviews*, 16(9), 939–955. [https://doi.org/10.1016/S0277-3791\(97\)00031-0](https://doi.org/10.1016/S0277-3791(97)00031-0)

Ignéczi, Á., Sole, A. J., Livingstone, S. J., Leeson, A. A., Fettweis, X., Selmes, N., ... Briggs, K. (2016). Northeast sector of the Greenland Ice Sheet to undergo the greatest inland expansion of supraglacial lakes during the 21st century.

<https://doi.org/10.1002/2016GL070338>

IPCC (2013): *Climate Change 2013: The Physical Science Basis. Contribution of Working Group I to the Fifth Assessment Report of the Intergovernmental Panel on Climate Change* [Stocker, T.F., D. Qin, G.-K. Plattner, M. Tignor, S.K. Allen, J. Boschung, A. Nauels, Y. Xia, V. Bex and P.M. Midgley (eds.)]. Cambridge University Press, Cambridge, United Kingdom and New York, NY, USA, 1535 pp, doi:10.1017/CBO9781107415324.

Jack, J. E., Eyre, R., & Zeng, X. (2017). Evaluation of Greenland near surface air temperature datasets, 115194, 1591–1605. <https://doi.org/10.5194/tc-11-1591-2017>

Jenkins, A. (n.d.). Convection-Driven Melting near the Grounding Lines of Ice Shelves and Tidewater Glaciers. <https://doi.org/10.1175/JPO-D-11-03.1>

Johansson, A. M., Jansson, P., & Brown, I. A. (2013). Spatial and temporal variations in lakes on the Greenland Ice Sheet. *Journal of Hydrology*, 476, 314–320.

<https://doi.org/10.1016/J.JHYDROL.2012.10.045>

Joughin, I., Das, S. B., King, M. A., Smith, B. E., Howat, I. M., & Moon, T. (2008). Seasonal speedup along the western flank of the Greenland Ice Sheet. *Science (New York, N.Y.)*, 320(5877), 781–3. <https://doi.org/10.1126/science.1153288>

- Kamb, B. (1987). Glacier surge mechanism based on linked cavity configuration of the basal water conduit system. *Journal of Geophysical Research*, 92(B9), 9083. <https://doi.org/10.1029/JB092iB09p09083>
- Karlstrom, L., Gajjar, P., & Manga, M. (2013). Meander formation in supraglacial streams. *Journal of Geophysical Research: Earth Surface*, 118(118), 1–11. <https://doi.org/10.1002/jgrf.20135>
- Kattel, D. B., Yao, T., Yang, K., Tian, L., Yang, G., & Joswiak, D. (2013). Temperature lapse rate in complex mountain terrain on the southern slope of the central Himalayas. *Theoretical and Applied Climatology*, 113(3–4), 671–682. <https://doi.org/10.1007/s00704-012-0816-6>
- Kingslake, J., Ng, F., & Sole, A. (2015). Modelling channelized surface drainage of supraglacial lakes. *Journal of Glaciology*, 61(225), 185–199. <https://doi.org/10.3189/2015JoG14J158>
- Koenig, L. S., Lampkin, D. J., Montgomery, L. N., Hamilton, S. L., Turrin, J. B., Joseph, C. A., ... Gogineni, P. (2015). Wintertime storage of water in buried supraglacial lakes across the Greenland Ice Sheet. *The Cryosphere*, 9(4), 1333–1342. <https://doi.org/10.5194/tc-9-1333-2015>
- Koziol, C. P., & Arnold, N. (2018). Modelling seasonal meltwater forcing of the velocity of land-terminating margins of the Greenland Ice Sheet. *The Cryosphere*, 12(3), 971–991. <https://doi.org/10.5194/tc-12-971-2018>
- Koziol, C., Arnold, N., Pope, A., & Colgan, W. (2017). Quantifying supraglacial meltwater pathways in the Paakitsoq region, West Greenland. *Journal of Glaciology*, 63(239), 464–476. <https://doi.org/10.1017/jog.2017.5>
- Krabill, E., Abdalati, P., Frederick, Manizade, Martin, Sonntag, ... Yungel. (2000). Greenland Ice Sheet: High-Elevation Balance and Peripheral Thinning. *Science (New York, N.Y.)*, 289(5478), 428–430. <https://doi.org/10.1126/science.276.5314.934>
- Lampkin, D. J., & VanderBerg, J. (2011). A preliminary investigation of the influence of basal and surface topography on supraglacial lake distribution near Jakobshavn Isbrae, western Greenland. *Hydrological Processes*, 25(21), 3347–3355. <https://doi.org/10.1002/hyp.8170>
- Langley, E. S., Leeson, A. A., Stokes, C. R., & Jamieson, S. S. R. (2016). Seasonal evolution of supraglacial lakes on an East Antarctic outlet glacier. *Geophysical Research Letters*, 43(16), 8563–8571. <https://doi.org/10.1002/2016GL069511>
- Leeson, A. A., Shepherd, A., Palmer, S., Sundal, A., & Fettweis, X. (2012). Simulating the growth of supraglacial lakes at the western margin of the Greenland ice sheet. *The Cryosphere*, 6, 1077–1086. <https://doi.org/10.5194/tc-6-1077-2012>
- Leeson, A. A., Shepherd, A., Briggs, K., Howat, I., Fettweis, X., Morlighem, M., & Rignot, E. (2015). Supraglacial lakes on the Greenland ice sheet advance inland under warming climate. *Nature Climate Change*, 5(1), 51–55. <https://doi.org/10.1038/nclimate2463>

- Liang, Y.-L., Colgan, W., Lv, Q., Steffen, K., Abdalati, W., Stroeve, J., ... Bayou, N. (2012). A decadal investigation of supraglacial lakes in West Greenland using a fully automatic detection and tracking algorithm. *Remote Sensing of Environment*, 123, 127–138. <https://doi.org/10.1016/J.RSE.2012.03.020>
- Libois, Q., Picard, G., Arnaud, L., Morin, S., & Brun, E. (2014). Modeling the impact of snow drift on the decameter-scale variability of snow properties on the Antarctic Plateau. *Journal of Geophysical Research: Atmospheres*, 119(20), 11,662–11,681. <https://doi.org/10.1002/2014JD022361>
- Liston, G. E., Elder, K., Liston, G. E., & Elder, K. (2006). A Distributed Snow-Evolution Modeling System (SnowModel). *Journal of Hydrometeorology*, 7(6), 1259–1276. <https://doi.org/10.1175/JHM548.1>
- Liston, G. E., & Hall, D. K. (1995). An energy-balance model of lake-ice evolution. *Journal of Glaciology*, 41(138), 373–382. <https://doi.org/10.3189/S0022143000016245>
- Livingstonea, D. M., & Adrianb, R. (2009). Modeling the duration of intermittent ice cover on a lake for climate-change studies. *Limnology and Oceanography*, 54(5), 1709–1722. <https://doi.org/10.4319/lo.2009.54.5.1709>
- Loucks, D., & van Beek, E. (2005). UNESCO - Water Resources Systems Planning; Management, 2005.
- Lüthje, M., Pedersen, L. T., Reeh, N., & Greuell, W. (2006). Modelling the evolution of supraglacial lakes on the West Greenland ice-sheet margin. *Journal of Glaciology*, 52(179), 608–618. <https://doi.org/10.3189/172756506781828386>
- Lydersen, E., Aanes, K.J., Andersen, S., Andersen, T., Brettum, P., Bækken, T., Lien, L., Lindstrøm, E.A., Løvik, J.E., Mjelde, M., Oredalen, T.J., Lyche, A.S., Romstad, R., Rørslett, B., Saloranta, T., 2003. THERMOS-prosjektet: Fagrapport 1998–2002. NIVA rapport 4720-2003, Norwegian Institute for Water Research, Oslo, Norway, 119 pp. (in Norwegian).
- Maclagan Cathles, L., Abbot, D. S., Bassis, J. N., & Macayeal, D. R. (n.d.). Modeling surface-roughness/solar-ablation feedback: application to small-scale surface channels and crevasses of the Greenland ice sheet. *Annals of Glaciology*, 52(59).
- Mankoff, K. D., & Tulaczyk, S. M. (2017). The past, present, and future viscous heat dissipation available for Greenland subglacial conduit formation. *The Cryosphere*, 11(1), 303–317. <https://doi.org/10.5194/tc-11-303-2017>
- Marston, R. A. (1983). Supraglacial Stream Dynamics on the Juneau Icefield. *Annals of the Association of American Geographers*, 73(4), 597–608. <https://doi.org/10.1111/j.1467-8306.1983.tb01861.x>

- Maykut, G. A., & Untersteiner, N. (1971). Some results from a time-dependent thermodynamic model of sea ice. *Journal of Geophysical Research*, 76(6), 1550–1575. <https://doi.org/10.1029/JC076i006p01550>
- McMillan, M., Nienow, P., Shepherd, A., Benham, T., & Sole, A. (2007). Seasonal evolution of supra-glacial lakes on the Greenland Ice Sheet. *Earth and Planetary Science Letters*, 262(3–4), 484–492. <https://doi.org/10.1016/J.EPSL.2007.08.002>
- Meierbachtol, T., Harper, J., & Humphrey, N. (2013). Basal drainage system response to increasing surface melt on the Greenland ice sheet. *Science (New York, N.Y.)*, 341(6147), 777–9. <https://doi.org/10.1126/science.1235905>
- Meierbachtol, T. W., Harper, J. T., Johnson, J. V., Humphrey, N. F., & Brinkerhoff, D. J. (2015). Thermal boundary conditions on western Greenland: Observational constraints and impacts on the modeled thermomechanical state. *Journal of Geophysical Research: Earth Surface*, 120(3), 623–636. <https://doi.org/10.1002/2014JF003375>
- Miles, K. E., Willis, I. C., Benedek, C. L., Williamson, A. G., & Tedesco, M. (2017). Toward Monitoring Surface and Subsurface Lakes on the Greenland Ice Sheet Using Sentinel-1 SAR and Landsat-8 OLI Imagery. *Frontiers in Earth Science*, 5, 58. <https://doi.org/10.3389/feart.2017.00058>
- Minder, J. R., Mote, P. W., & Lundquist, J. D. (2010). Surface temperature lapse rates over complex terrain: Lessons from the Cascade Mountains. *Journal of Geophysical Research*, 115(D14), D14122. <https://doi.org/10.1029/2009JD013493>
- Moon, T., Joughin, I., & Smith, B. (2015). Seasonal to multiyear variability of glacier surface velocity, terminus position, and sea ice/ice mélange in northwest Greenland. *Journal of Geophysical Research: Earth Surface*, 120(5), 818–833. <https://doi.org/10.1002/2015JF003494>
- Moon, T., Joughin, I., Smith, B., van den Broeke, M. R., van de Berg, W. J., Noël, B., & Usher, M. (2014). Distinct patterns of seasonal Greenland glacier velocity. *Geophysical Research Letters*, 41(20), 7209–7216. <https://doi.org/10.1002/2014GL061836>
- Morassutti, I., & Ledrew, E. F. (n.d.). ALBEDO AND DEPTH OF MELT PONDS ON SEA-ICE. *INTERNATIONAL JOURNAL OF CLIMATOLOGY*, 16(8), 17–838.
- Nghiem, S. V., Hall, D. K., Mote, T. L., Tedesco, M., Albert, M. R., Keegan, K., ... Neumann, G. (2012). The extreme melt across the Greenland ice sheet in 2012. *Geophysical Research Letters*, 39(20). <https://doi.org/10.1029/2012GL053611>
- Nick, F. M., Vieli, A., Andersen, M. L., Joughin, I., Payne, A., Edwards, T. L., ... van de Wal, R. S. W. (2013). Future sea-level rise from Greenland's main outlet glaciers in a warming climate. *Nature*, 497(7448), 235–238. <https://doi.org/10.1038/nature12068>

Nienow, P. W., Sole, A. J., Slater, D. A., & Cowton, T. R. (2017). Recent Advances in Our Understanding of the Role of Meltwater in the Greenland Ice Sheet System. *Current Climate Change Reports*, 3(4), 330–344. <https://doi.org/10.1007/s40641-017-0083-9>

Nienow, P., Sharp, M., & Willis, I. (1998). Seasonal changes in the morphology of the subglacial drainage system, Haut Glacier d’Arolla, Switzerland. *Earth Surface Processes and Landforms*, 23(9), 825–843.

Noël, B., Van De Berg, W. J., Melchior Van Wessem, J., Van Meijgaard, E., Van As, D., Lenaerts, J. T. M., ... Van Den Broeke, M. R. (2018). Modelling the climate and surface mass balance of polar ice sheets using RACMO2 – Part 1: Greenland (1958–2016). *The Cryosphere*, 12, 811–831. <https://doi.org/10.5194/tc-12-811-2018>

Phillips, T., Rajaram, H., Colgan, W., Steffen, K., & Abdalati, W. (2013). Evaluation of cryo-hydrologic warming as an explanation for increased ice velocities in the wet snow zone, Sermeq Avannarleq, West Greenland. *Journal of Geophysical Research: Earth Surface*, 118(3), 1241–1256. <https://doi.org/10.1002/jgrf.20079>

Phillips, T., Rajaram, H., & Steffen, K. (2010). Cryo-hydrologic warming: A potential mechanism for rapid thermal response of ice sheets. *Geophysical Research Letters*, 37(20), n/a-n/a. <https://doi.org/10.1029/2010GL044397>

Poinar, K., Joughin, I., Das, S. B., Behn, M. D., Lenaerts, J. T. M., & van den Broeke, M. R. (2015). Limits to future expansion of surface-melt-enhanced ice flow into the interior of western Greenland. *Geophysical Research Letters*, 42(6), 1800–1807. <https://doi.org/10.1002/2015GL063192>

Purves, R. S., Mackness, W. A., & Sugden, D. E. (1999). An approach to modelling the impact of snow drift on glaciation in the Cairngorm Mountains, Scotland. *Journal of Quaternary Science*, 14(4), 313–321.

Rennermalm, A. K., Moustafa, S. E., Mioduszewski, J., Chu, V. W., Forster, R. R., Hagedorn, B., ... Tedesco, M. (2013). Understanding Greenland ice sheet hydrology using an integrated multi-scale approach. *Environmental Research Letters*, 8(1), 15017. <https://doi.org/10.1088/1748-9326/8/1/015017>

Rignot, E., Velicogna, I., van den Broeke, M. R., Monaghan, A., & Lenaerts, J. T. M. (2011). Acceleration of the contribution of the Greenland and Antarctic ice sheets to sea level rise. *Geophysical Research Letters*, 38(5), n/a-n/a. <https://doi.org/10.1029/2011GL046583>

Rignot, E., Koppes, M., & Velicogna, I. (2010). Rapid submarine melting of the calving faces of West Greenland glaciers. *Nature Geoscience*, 3(3), 187–191. <https://doi.org/10.1038/ngeo765>

Saloranta, T. M., & Andersen, T. (2007). MyLake—A multi-year lake simulation model code suitable for uncertainty and sensitivity analysis simulations. *Ecological Modelling*, 207(1), 45–60. <https://doi.org/10.1016/J.ECOLMODEL.2007.03.018>

- Saloranta, T. M., Forsius, M., Järvinen, M., & Arvola, L. (2009). Impacts of projected climate change on the thermodynamics of a shallow and a deep lake in Finland: model simulations and Bayesian uncertainty analysis. *Hydrology Research*, 40(2–3), 234. <https://doi.org/10.2166/nh.2009.030>
- Saltelli, A., Tarantola, S., & Chan, .-S. (1999). A Quantitative Model-Independent Method for Global Sensitivity Analysis of Model Output. *Technometrics*, 41(1), 39–56. <https://doi.org/10.1080/00401706.1999.10485594>
- Schoof, C. (2010). Ice-sheet acceleration driven by melt supply variability. *Nature*, 468(7325), 803–806. <https://doi.org/10.1038/nature09618>
- Selmes, N., Murray, T., & James, T. D. (2013). Characterizing supraglacial lake drainage and freezing on the Greenland Ice Sheet. *The Cryosphere Discussions*, 7(1), 475–505. <https://doi.org/10.5194/tcd-7-475-2013>
- Selmes, N., Murray, T., & James, T. D. (2011). Fast draining lakes on the Greenland Ice Sheet. *Geophysical Research Letters*, 38(15), n/a-n/a. <https://doi.org/10.1029/2011GL047872>
- Sergienko, O., & Macayeal, D. R. (2005). Surface melting on Larsen Ice Shelf, Antarctica. *Annals of Glaciology*, 40, 215–218. <https://doi.org/10.3189/172756405781813474>
- Skyllingstad, E. D., Paulson, C. A., & Perovich, D. K. (2009). Simulation of melt pond evolution on level ice. *J. Geophys. Res.*, 114. <https://doi.org/10.1029/2009JC005363>
- Smith, L. C., Yang, K., Pitcher, L. H., Overstreet, B. T., Chu, V. W., Rennermalm, Å. K., ... Behar, A. E. (2017). Direct measurements of meltwater runoff on the Greenland ice sheet surface. *Proceedings of the National Academy of Sciences of the United States of America*, 114(50), E10622–E10631. <https://doi.org/10.1073/pnas.1707743114>
- Sneed, W. A., & Hamilton, G. S. (2007). Evolution of melt pond volume on the surface of the Greenland Ice Sheet. *Geophysical Research Letters*, 34(3), L03501. <https://doi.org/10.1029/2006GL028697>
- Sole, A., Nienow, P., Bartholomew, I., Mair, D., Cowton, T., Tedstone, A., & King, M. A. (2013). Winter motion mediates dynamic response of the Greenland Ice Sheet to warmer summers. *Geophysical Research Letters*, 40(15), 3940–3944. <https://doi.org/10.1002/grl.50764>
- Steger, C. R., Reijmer, C. H., & Van Den Broeke, M. R. (2017). The modelled liquid water balance of the Greenland Ice Sheet, 115194, 2507–2526. <https://doi.org/10.5194/tc-11-2507-2017>
- Sundal, A. V, Shepherd, A., Nienow, P., Hanna, E., Palmer, S., & Huybrechts, P. (2007). Evolution of supra-glacial lakes across the Greenland Ice Sheet. *Remote Sensing of Environment*, 113, 2164–2171. <https://doi.org/10.1016/j.rse.2009.05.018>

Sundal, A. V., Shepherd, A., Nienow, P., Hanna, E., Palmer, S., & Huybrechts, P. (2011). Melt-induced speed-up of Greenland ice sheet offset by efficient subglacial drainage. *Nature*, 469(7331), 521–524. <https://doi.org/10.1038/nature09740>

Surdu, C. M., Duguay, C. R., Brown, L. C., & Prieto, D. F. (2014). Response of ice cover on shallow lakes of the North Slope of Alaska to contemporary climate conditions (1950–2011): radar remote-sensing and numerical modeling data analysis. *The Cryosphere*, 8, 167–180. <https://doi.org/10.5194/tc-8-167-2014>

Surdu, C. M., Duguay, C. R., Brown, L. C., & Fernández Prieto, D. (2014). Response of ice cover on shallow lakes of the North Slope of Alaska to contemporary climate conditions (1950–2011): radar remote-sensing and numerical modeling data analysis. *The Cryosphere*, 8(1), 167–180. <https://doi.org/10.5194/tc-8-167-2014>

Taylor, P. D., & Feltham, D. L. (2004). A model of melt pond evolution on sea ice. *Journal of Geophysical Research*, 109(C12), C12007. <https://doi.org/10.1029/2004JC002361>

Tedesco, M., Fettweis, X., Mote, T., Wahr, J., Alexander, P., Box, J. E., & Wouters, B. (2013). Evidence and analysis of 2012 Greenland records from spaceborne observations, a regional climate model and reanalysis data. *The Cryosphere*, 7(2), 615–630. <https://doi.org/10.5194/tc-7-615-2013>

Tedesco, M., Lüthje, M., Steffen, K., Steiner, N., Fettweis, X., Willis, I., ... Banwell, A. (2012). Measurement and modeling of ablation of the bottom of supraglacial lakes in western Greenland. *Geophysical Research Letters*, 39(2), n/a-n/a. <https://doi.org/10.1029/2011GL049882>

Tedesco, M., Willis, I. C., Hoffman, M. J., Banwell, A. F., Alexander, P., & Arnold, N. S. (2013). Ice dynamic response to two modes of surface lake drainage on the Greenland ice sheet. *Environmental Research Letters*, 8(3), 34007. <https://doi.org/10.1088/1748-9326/8/3/034007>

Tedstone, A. J., Nienow, P. W., Gourmelen, N., Dehecq, A., Goldberg, D., & Hanna, E. (2015). Decadal slowdown of a land-terminating sector of the Greenland Ice Sheet despite warming. *Nature*, 526(7575), 692–695. <https://doi.org/10.1038/nature15722>

Tedstone, A. J., Nienow, P. W., Sole, A. J., Mair, D. W. F., Cowton, T. R., Bartholomew, I. D., & King, M. A. (n.d.). Greenland ice sheet motion insensitive to exceptional meltwater forcing. <https://doi.org/10.1073/pnas.1315843110>

Tetens, O., 1930: Über einige meteorologische Begriffe. *Zeitschrift für Geophysik*, Vol. 6:297.

Tilzer, M. M. (1983). The importance of fractional light absorption by photosynthetic pigments for phytoplankton productivity in Lake Constance. *Limnology and Oceanography*, 28(5), 833–846. <https://doi.org/10.4319/lo.1983.28.5.0833>

Troin, M., Arsenault, R., & Brissette, F. (2015). Performance and Uncertainty Evaluation of Snow Models on Snowmelt Flow Simulations over a Nordic Catchment (Mistassibi, Canada). *Hydrology*, 2(4), 289–317. <https://doi.org/10.3390/hydrology2040289>

UNESCO, 1981. International Equation of State of Seawater 1980. UNESCO Technical Papers in Marine Science No. 36.

Valéry, A., Andréassian, V., & Perrin, C. (2010). Regionalization of precipitation and air temperature over high-altitude catchments – learning from outliers. *Hydrological Sciences Journal*, 55(6), 928–940. <https://doi.org/10.1080/02626667.2010.504676>

van Angelen, J. H., van den Broeke, M. R., Wouters, B., & Lenaerts, J. T. M. (2014). Contemporary (1960–2012) Evolution of the Climate and Surface Mass Balance of the Greenland Ice Sheet. *Surveys in Geophysics*, 35(5), 1155–1174. <https://doi.org/10.1007/s10712-013-9261-z>

van As, D., Fausto, R. S., Ahlström, A. P., Andersen, S. B., Andersen, M. L., Citterio, M., ... Weidick, A. (2003). Programme for Monitoring of the Greenland Ice Sheet (PROMICE): first temperature and ablation records. *Geological Survey of Denmark and Greenland Bulletin*, 23, 73–76. Retrieved from <https://dspace.library.uu.nl/handle/1874/255179>

van de Wal, R. S. W., Boot, W., Smeets, C. J. P. P., Snellen, H., van den Broeke, M. R., & Oerlemans, J. (2012). Twenty-one years of mass balance observations along the K-transect, West Greenland. *Earth System Science Data*, 4(1), 31–35. <https://doi.org/10.5194/essd-4-31-2012>

van den Broeke, M., Bamber, J., Ettema, J., Rignot, E., Schrama, E., van de Berg, W. J., ... Wouters, B. (2009). Partitioning Recent Greenland Mass Loss. *Science*, 326(5955), 984–986. <https://doi.org/10.1126/science.1178176>

van den Broeke, M. R., Enderlin, E. M., Howat, I. M., Kuipers Munneke, P., Noël, B. P. Y., van de Berg, W. J., ... Wouters, B. (2016). On the recent contribution of the Greenland ice sheet to sea level change. *The Cryosphere*, 10(5), 1933–1946. <https://doi.org/10.5194/tc-10-1933-2016>

Van Den Broeke, M. R., Enderlin, E. M., Howat, I. M., Munneke, P. K., Noël, B. P. Y., Van De Berg, W. J., ... Wouters, B. (1933). On the recent contribution of the Greenland ice sheet to sea level change. *The Cryosphere*, 10. <https://doi.org/10.5194/tc-10-1933-2016>

van der Veen, C. J. (2007). Fracture propagation as means of rapidly transferring surface meltwater to the base of glaciers. *Geophysical Research Letters*, 34(1), L01501. <https://doi.org/10.1029/2006GL028385>

van der Veen, C. J. (1998). Fracture mechanics approach to penetration of surface crevasses on glaciers. *Cold Regions Science and Technology*, 27(1), 31–47. [https://doi.org/10.1016/S0165-232X\(97\)00022-0](https://doi.org/10.1016/S0165-232X(97)00022-0)

Vavrus, S. J., Wynne, R. H., & Foley, J. A. (1996). Measuring the sensitivity of southern Wisconsin lake ice to climate variations and lake depth using a numerical model. *Limnol. Oceanogr*, 41(5), 822–83.

Velicogna, I., & Wahr, J. (2006). Measurements of Time-Variable Gravity Show Mass Loss in Antarctica. *Science*, 311(5768), 1754–1756. <https://doi.org/10.1126/science.1123785>

Vernon, C. L., Bamber, J. L., Box, J. E., Van Den Broeke, M. R., Fettweis, X., Hanna, E., & Huybrechts, P. (2013). Surface mass balance model intercomparison for the Greenland ice sheet. *The Cryosphere*, 7, 599–614. <https://doi.org/10.5194/tc-7-599-2013>

Walter, M. T., Mccool, D. K., King, L. G., Molnau, M., & Campbell, G. S. (n.d.). Simple Snowdrift Model for Distributed Hydrological Modeling. <https://doi.org/10.1061/ASCE1084-069920049:4280>

Williamson, A. G., Arnold, N. S., Banwell, A. F., & Willis, I. C. (2017). A Fully Automated Supraglacial lake area and volume Tracking (“FAST”) algorithm: Development and application using MODIS imagery of West Greenland. *Remote Sensing of Environment*, 196, 113–133. <https://doi.org/10.1016/J.RSE.2017.04.032>

Williamson, A. G., Banwell, A. F., Willis, I. C., & Arnold, N. S. (2018). Dual-satellite (Sentinel-2 and Landsat 8) remote sensing of supraglacial lakes in Greenland. *The Cryosphere Discussions*, 1–27. <https://doi.org/10.5194/tc-2018-56>

Williamson, A. G., Willis, I. C., Arnold, N. S., & Banwell, A. F. (2018). Controls on rapid supraglacial lake drainage in West Greenland: an Exploratory Data Analysis approach. *Journal of Glaciology*, 64(244), 208–226. <https://doi.org/10.1017/jog.2018.8>

Xu, Y., Rignot, E., Fenty, I., Menemenlis, D., & Flexas, M. M. (2013). Subaqueous melting of Store Glacier, west Greenland from three-dimensional, high-resolution numerical modeling and ocean observations. *Geophysical Research Letters*, 40(17), 4648–4653. <https://doi.org/10.1002/grl.50825>

Yallop, M. L., Anesio, A. M., Perkins, R. G., Cook, J., Telling, J., Fagan, D., ... Roberts, N. W. (2012). Photophysiology and albedo-changing potential of the ice algal community on the surface of the Greenland ice sheet. *The ISME Journal*, 6(12), 2302–2313. <https://doi.org/10.1038/ismej.2012.107>

Yang, K., & Smith, L. C. (2016). Internally drained catchments dominate supraglacial hydrology of the southwest Greenland Ice Sheet. *Journal of Geophysical Research: Earth Surface*, 121(10), 1891–1910. <https://doi.org/10.1002/2016JF003927>

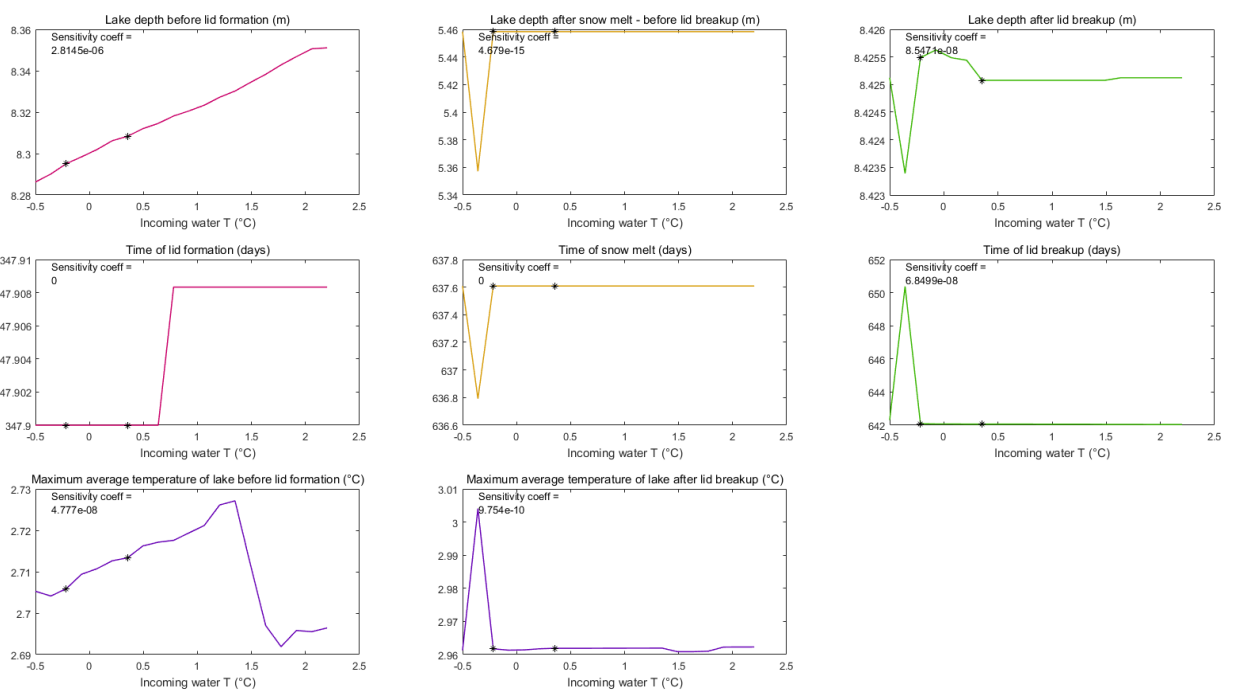
Zwally, H. J., Abdalati, W., Herring, T., Larson, K., Saba, J., & Steffen, K. (n.d.). Surface Melt-Induced Acceleration of Greenland Ice-Sheet Flow.

Polar ice sheets melting - in pictures | Environment | The Guardian. (2012). Retrieved June 7, 2018, from <https://www.theguardian.com/environment/gallery/2012/nov/29/polar-ice-sheets-losing-mass-in-pictures>

## Appendices

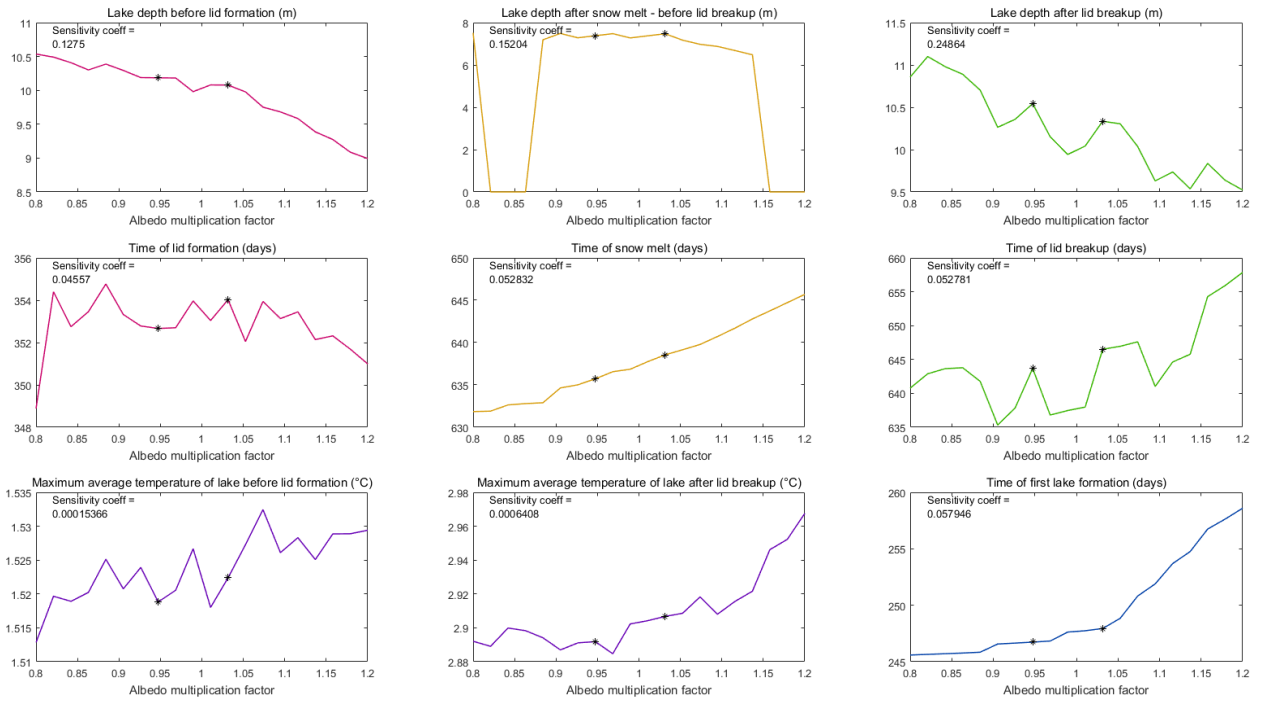
### Appendix 1: sensitivity testing results

#### Incoming water temperature



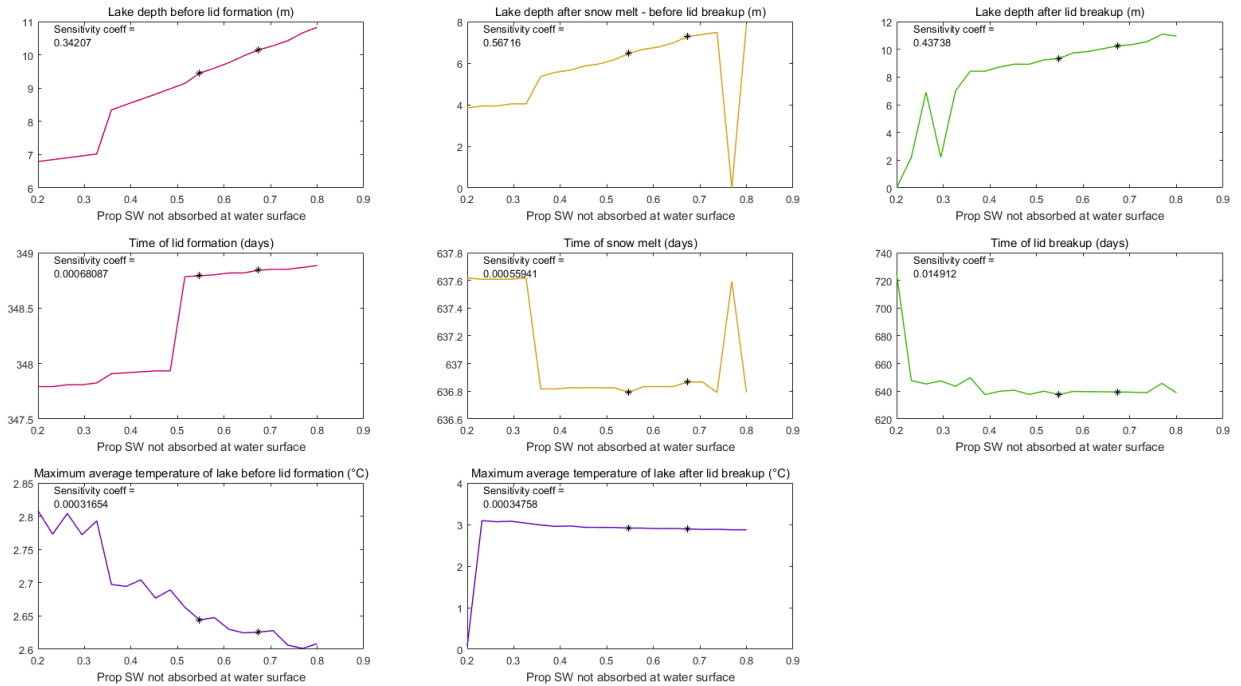
Appendix 1, figure 1: the effect of varying incoming water temperature on model output variables.

## Albedo



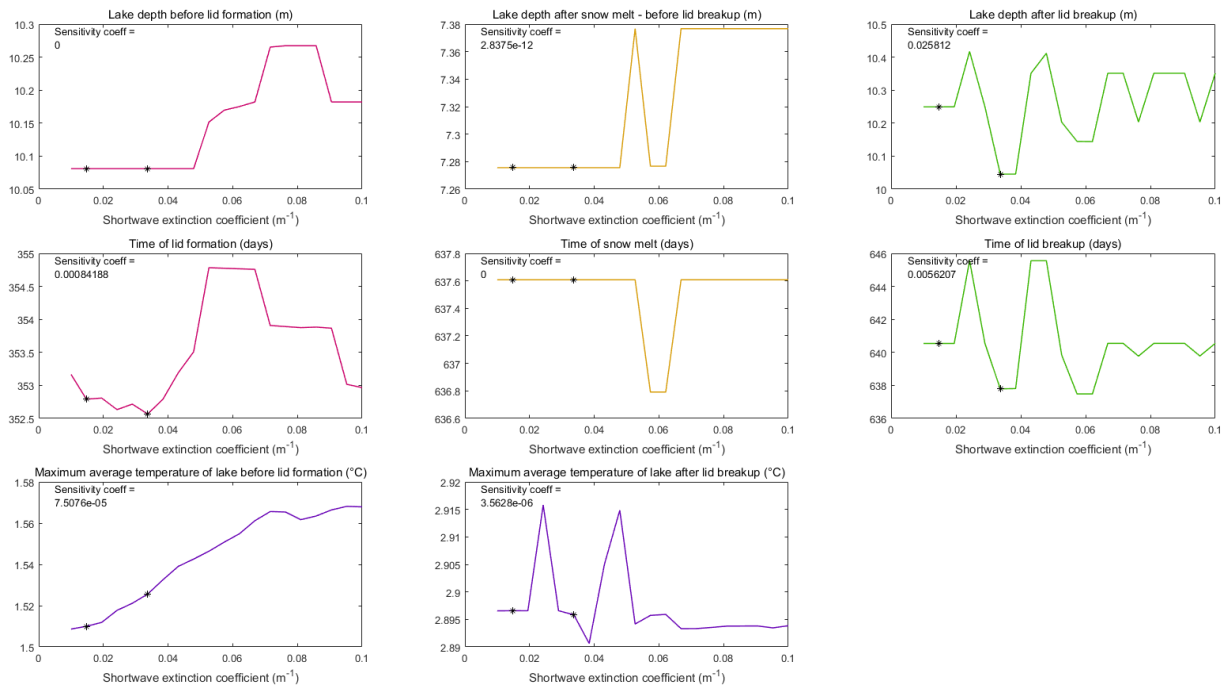
Appendix 1, figure 2: the effect of increasing or decreasing albedo used in the model. Black stars are the values used in calculating the sensitivity coefficient.

### The $I_0$ term



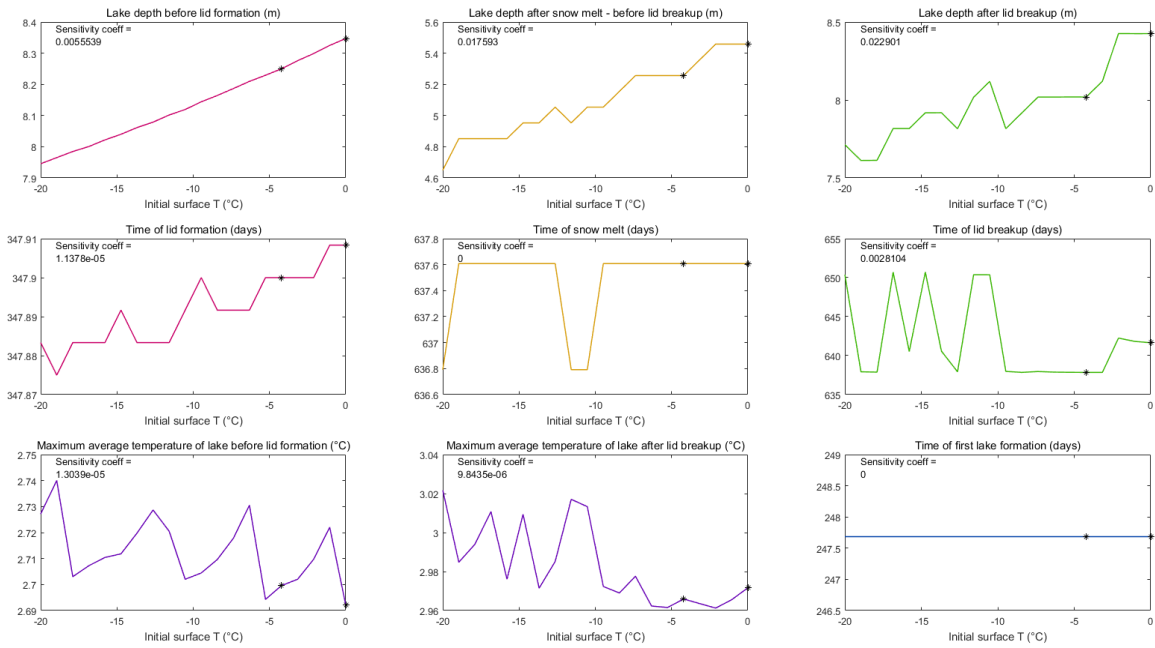
Appendix 1, figure 3: the effect of varying  $I_0$ . Black stars are the values used in calculating the sensitivity coefficient.

Shortwave extinction coefficient

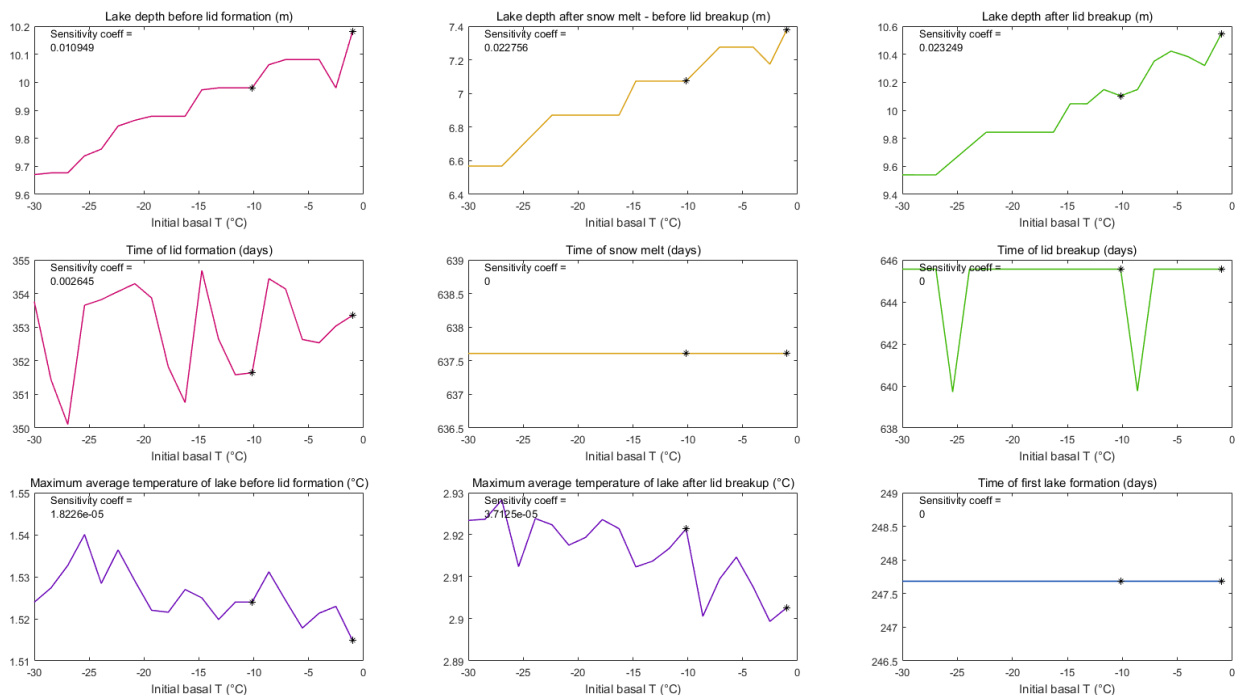


Appendix 1, figure 4: the effect of varying shortwave extinction coefficient for water. Black stars are the values used in calculating the sensitivity coefficient.

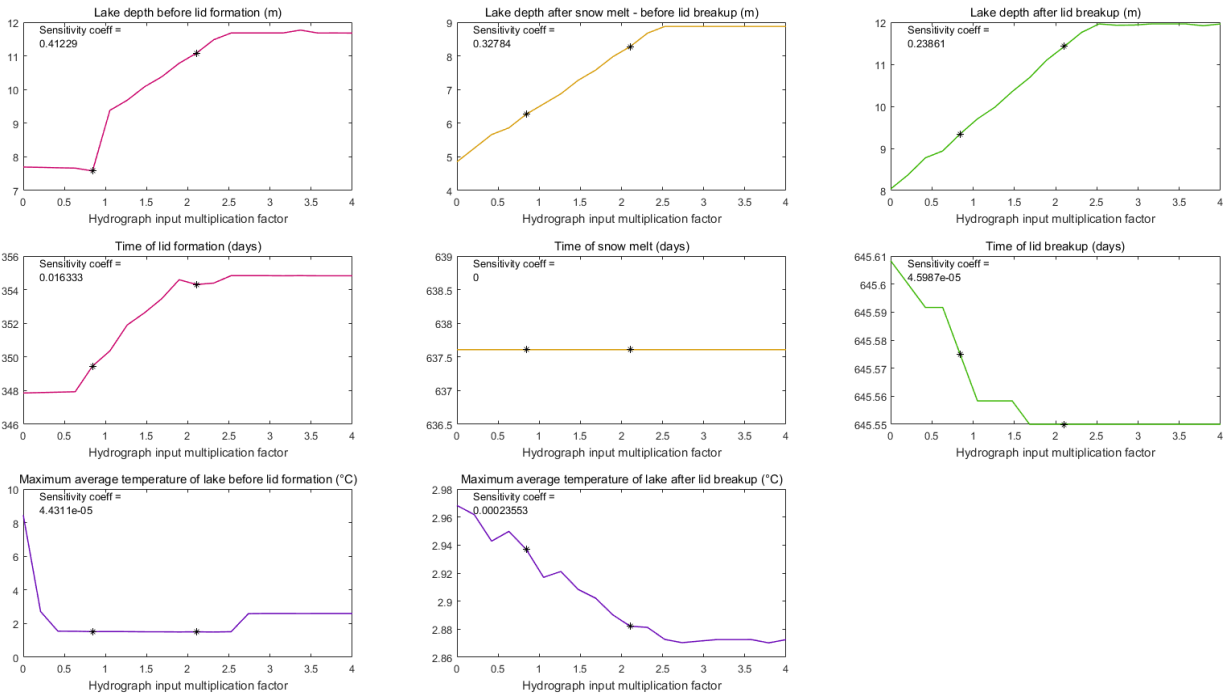
Initial surface temperature of ice



### Basal temperature of ice

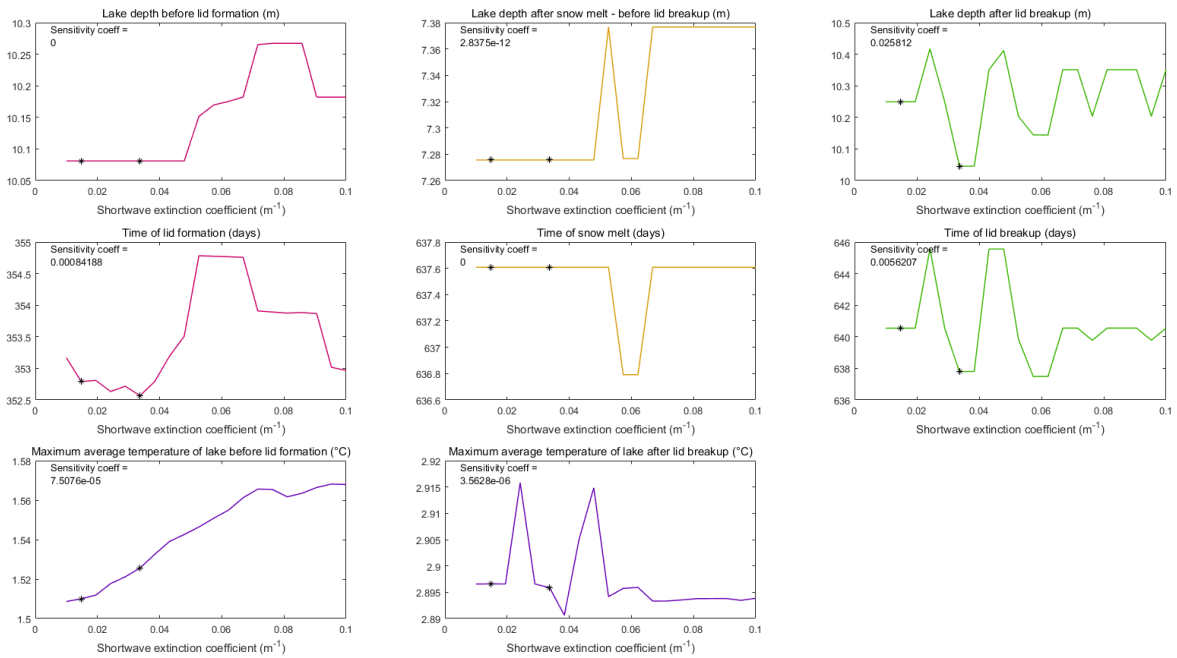


### Hydrograph input



Appendix 1, figure 7: the effect of multiplication factor for hydrograph input. Black stars are the values in calculating the sensitivity coefficient.

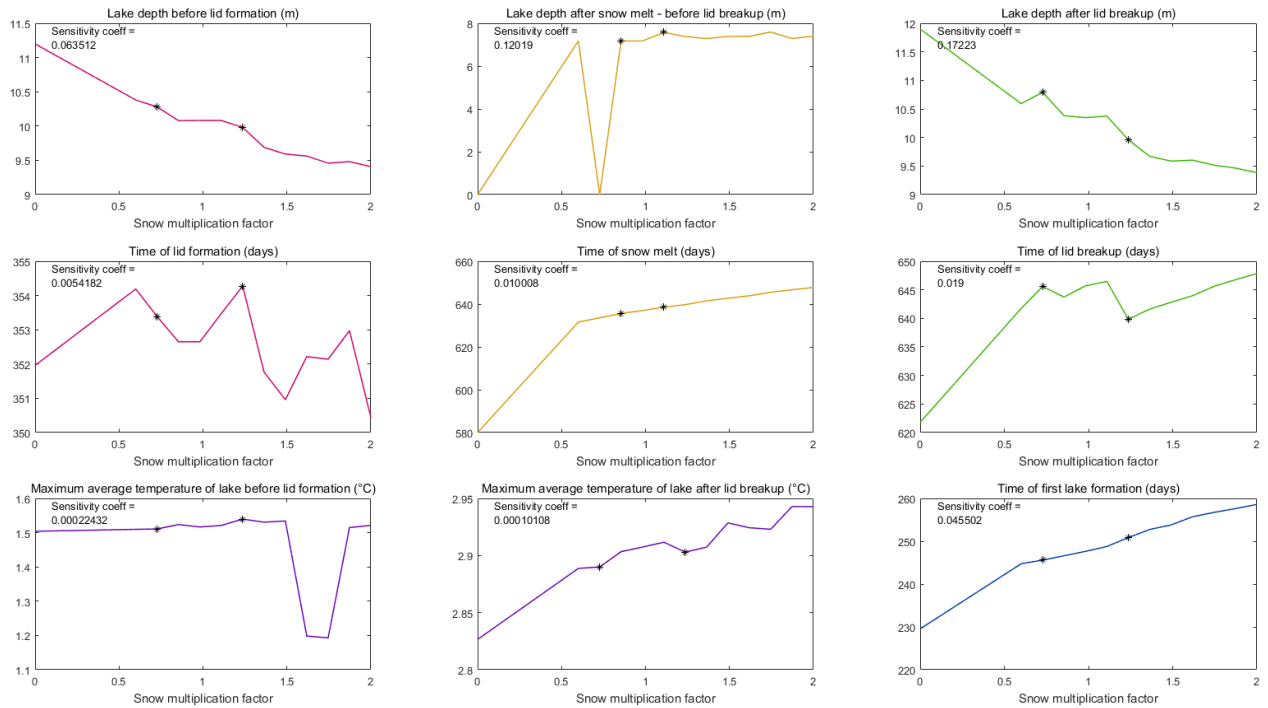
### Shortwave extinction coefficient for water



Appendix 1, figure 8: the effect of varying shortwave extinction coefficient of water. Black stars are the values used in calculating the sensitivity coefficient.

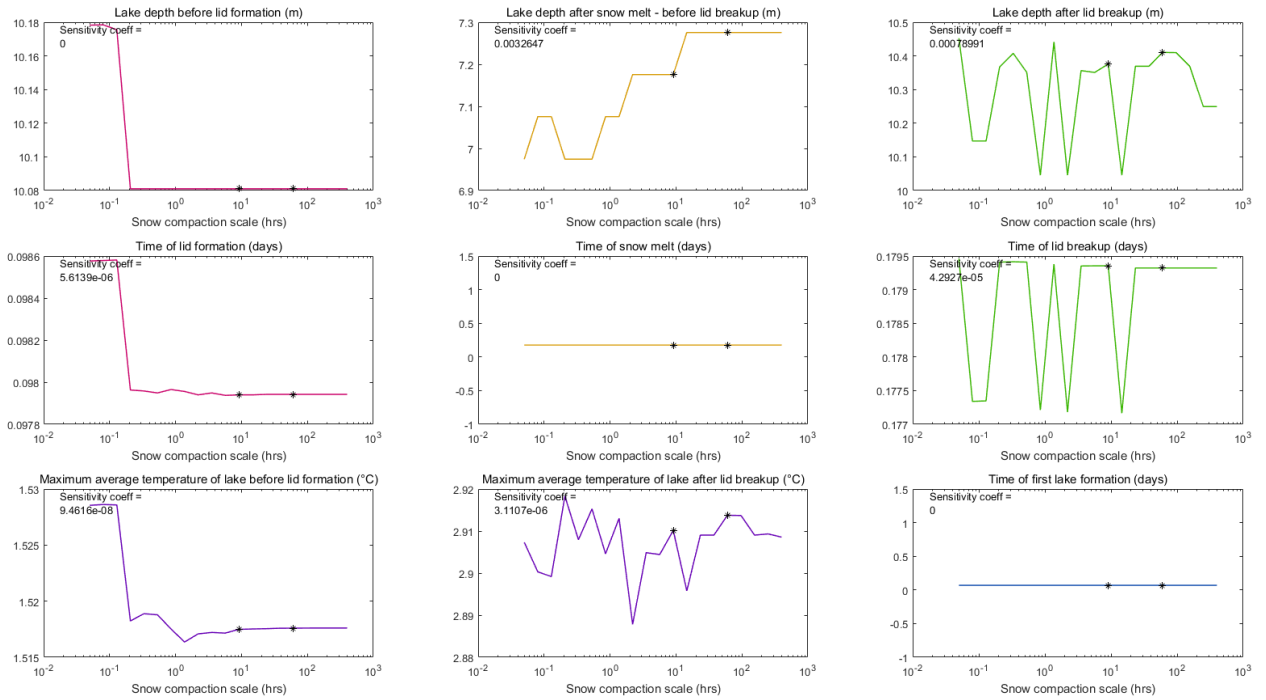
## Precipitation and its absence

A multiplication factor of  $< 0.6$  resulted in an unknown error. This was not addressed as no other instability was observed and errors did not arise for other model tests using different precipitation values.



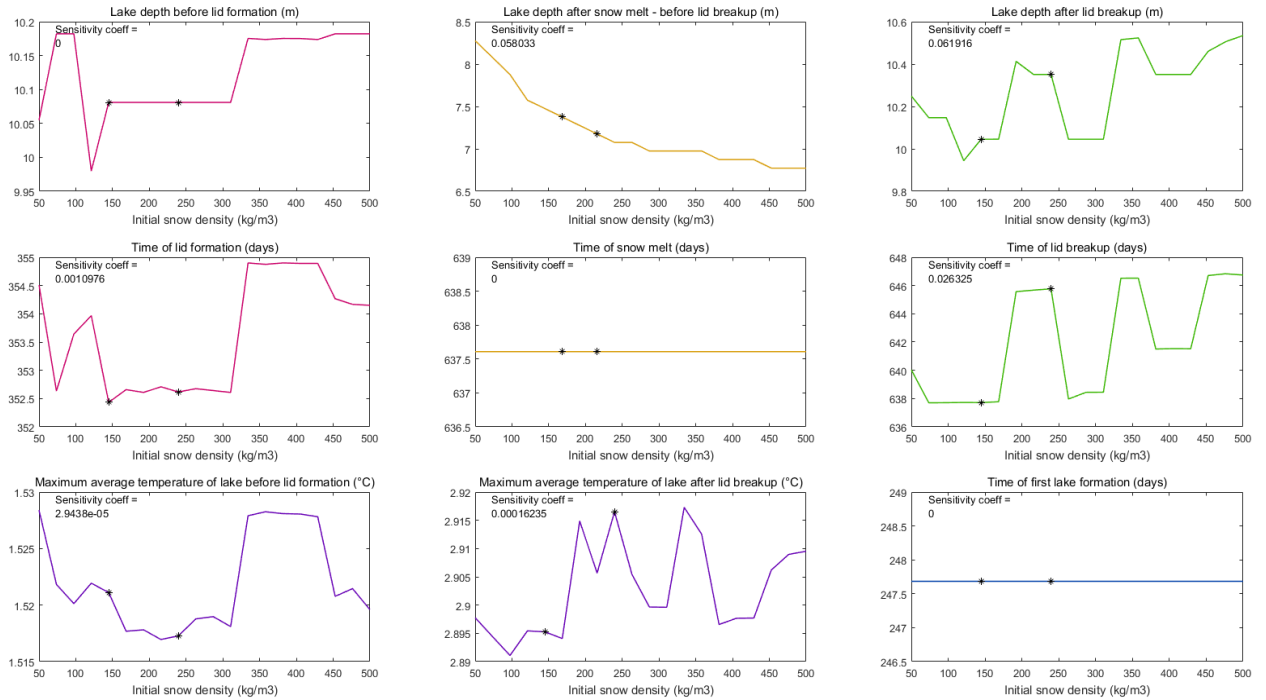
*Appendix 1, figure 9: the effect of increasing or reducing incoming snow to the model. Black stars are the values used in calculating the sensitivity coefficient.*

## Snow compaction timescale



Appendix 1, figure 10: the effect of varying snow compaction scale on model output variables. Note logarithmic scales. Black stars are the values used in calculating the sensitivity coefficient.

### Initial snow density



Appendix 1, figure 11: the effect of initial snow density on model output variables. Black stars are the values used in calculating the sensitivity coefficient.

## Appendix 2: notation

$\epsilon$	= emissivity
$F_{LWin}$	= incoming longwave radiation ( $W m^{-2}$ )
$\alpha$	= albedo
$F_{SW}$	= incoming shortwave radiation ( $W m^{-2}$ )
$\sigma$	= Stefan-Boltzmann constant ( $W m^{-2} K^{-4}$ )
$T$	= temperature (K)
$F_{sen}$	= sensible heat flux ( $W m^{-2}$ )
$F_{lat}$	= latent heat flux ( $W m^{-2}$ )
$\rho_{air}$	= density of dry air ( $kg m^{-3}$ )
$C_p^{air}$	= specific heat capacity of dry air ( $kJ kg^{-1} K^{-1}$ )
$v$	= wind speed ( $m s^{-1}$ )
$T_a$	= air temperature
$T_0$	= surface temperature
$L_v$	= latent heat of vaporisation ( $J kg^{-1}$ )
RH	= relative humidity (0-1)
$p$	= pressure (Pa)
$R_d$	= specific gas constant for dry air ( $Jkg^{-1}K^{-1}$ )
$R_v$	= specific gas constant for water vapor ( $Jkg^{-1}K^{-1}$ )
$F_i$	= flux at cell i ( $W m^{-2}$ )
$T$	= shortwave extinction coefficient ( $m^{-1}$ )
$z_i$	= depth of cell i (or i + 1)
$l_0$	= proportion of shortwave radiation absorbed at the surface
$\rho_{water}$	= density of water ( $kg m^3$ )
$T_{melt}$	= freezing point of water (K)
$L_f$	= latent heat of fusion of ice ( $J kg^{-1}$ )
$z_l$	= lake depth
$\bar{T}$	= average lake temperature (K)

$\rho_{\text{snow}}$  = density of fresh snow  
 $K_{\text{air}}$  = thermal conductivity of air  
 $\rho_s$  = current density of snow layer  
 $b$  = use specified exponent originally set as 2 (Essery, 2015)  
 $S_{\text{mwe}}$  = snow layer metres water equivalent  
 $\mu_s$  = proportion of snow layer which is snow-ice  
 $\lambda_s$  = proportion of snow layer which is water  
 $C_{\text{ice}}$  = heat capacity of ice  
 $C_{\text{water}}$  = heat capacity of water  
 $\rho_{\text{max}}$  = maximum density of melting snow if air temperature is above freezing and  
maximum density of cold snow if air temperature is below freezing ( $\text{kg m}^{-3}$ )  
 $\Delta t$  = time step (s)  
 $T_p$  = snow compaction timescale (s)  
 $T$  = temperature (K)  
 $t$  = time (s)  
 $K$  = thermal conductivity ( $\text{Wm}^{-1}\text{K}^{-1}$ )  
 $x$  = depth (m)  
 $n$  = time step  
 $i$  = cell index  
 $\Delta x$  = distance between the midpoints of two adjacent cells (m)  
 $\Delta t$  = time step (s)  
 $x_i^n$  = height of cell  
 $Q(P_0 + \Delta P)$  = output value  $Q$  when forced with a parameter value of  $P_0 + \Delta P$   
 $P_0$  = initial parameter value  
 $\Delta P$  = assumed reasonable positive or negative variation from  $P_0$   
 $\epsilon_{\text{cs}}$  = clear-sky emissivity  
 $n$  = cloudiness, assumed to be 0.6 by Lüthje et al. (2006)  
 $p$  = 4 (constant)  
 $\epsilon_{\text{oc}}$  = overcast-sky emissivity, assumed to be 0.952 by Lüthje et al. (2006)  
 $b$  = 0.484 (constant)  
 $m$  = 8 (constant)  
 $a_p$  = fraction of shortwave absorbed by the pond

$\alpha_i$  = bare ice albedo  
 $t_p$  = pond transmissivity as a function of depth  
 $l_0$  = fraction of ice shortwave to penetrate ice

### Appendix 3: default parameter values

Incoming water temperature = 0.5 °C  
Lake temperature averaging threshold = 0.09 m  
Lake temperature convection profile threshold = 0.7 m  
Minimum number of cells in a slush lid = 3 m  
How many times heavier weak section of lid needs to be than ice-lid = 1.1  
Initial ice surface temperature = -2 °C  
Initial basal ice temperature = -5 °C  
Initial snow density = 200 kg m<sup>-3</sup>  
Maximum snow density if melting = 500 kg m<sup>3</sup>  
Maximum snow density if freezing = 300 kg m<sup>3</sup>  
Snow compaction timescale = 20\*3600 seconds  
Ice albedo = 0.65  
Slush albedo = 0.55  
New snow albedo = 0.85  
IO water = 0.6  
Shortwave extinction coefficient of water = 0.025  
 $b_{exp} = 2$   
time step = 0.2  
number of ice cells = 150;  
thickness of ice cells = 0.1 m  
number of deep ice cells at coarser resolution = 10  
deep ice cell thickness = 1 m  
max snow albedo = 0.8;  
min snow albedo = 0.5  
snowfall required to refresh albedo = 10 kg/m<sup>2</sup>